

Collective dynamics and pair-distribution function of active Brownian ellipsoids

Stephan Bröker, Michael te Vrugt, and Raphael Wittkowski*
*Institute of Theoretical Physics, Center for Soft Nanoscience,
University of Münster, 48149 Münster, Germany*

While the collective dynamics of spherical active Brownian particles is relatively well understood by now, the much more complex dynamics of nonspherical active particles still raises interesting open questions. Previous work has shown that the dynamics of rod-like or ellipsoidal active particles can differ significantly from that of spherical ones. Here, we obtain the full state diagram of active Brownian ellipsoids depending on the Péclet number and packing density via computer simulations. The system is found to exhibit a rich state behavior that includes cluster formation, local polar order, polar flocks, and disordered states. Moreover, we obtain numerical results and an analytical representation for the pair-distribution function of active ellipsoids. This function provides useful quantitative insights into the collective behavior of active particles with lower symmetry and has potential applications in the development of predictive theoretical models.

I. INTRODUCTION

The physics of active matter [1, 2], which consists of self-propelled particles, is one of the central areas of soft matter physics. Of particular interest in this context is the collective dynamics of active particles. Here, a variety of phenomena have been studied, most notably *motility-induced phase separation* (MIPS) [3], which is the spontaneous formation of a high-density and a low-density phase in a system of repulsively interacting particles, and *flocking* [4–6], which refers to the coherent collective motion of active particles. Both phenomena continue to be widely investigated today [7–12].

The collective dynamics of active matter becomes considerably more complex if the particles are not – as assumed in many theoretical studies – spherical. For instance, studies of active ellipsoids [13] have found that ellipsoidal particle shapes suppress MIPS and give rise to a rich state diagram involving polar and nematic phases. Moreover, elongated particle shapes allow to study how phenomena known from classical liquid crystal physics, such as topological defects, are modified in active systems [14]. Consequently, the study of the collective dynamics of active particles with interaction potentials that have no spherical symmetry has been a growing field of research in the past years [13–24]. See Refs. [25–27] for reviews.

When obtaining the state diagram of active spheres, one usually considers the dependence on the Péclet number Pe (measuring the activity and temperature) and the packing density Φ_0 [28, 29]. These parameters are also used in state diagrams for active ellipsoids [14], although previous work has focused more on studying the effects of the particle shape [21–24, 30, 31]. Consequently, to understand the collective dynamics of active ellipsoids and to connect it to what is already known about active spheres, more detailed investigations of the state diagram of active ellipsoids as a function of Pe and Φ_0 are

required.

A particularly useful quantity for understanding the collective dynamics of simple and complex fluids is the pair-distribution function g [32], which determines how the position (and possibly orientation) of a particle depends on that of a reference particle. This function is important because it allows to calculate thermodynamic properties of a system and because it appears in microscopically derived field theories [33–39]. Field-theoretical models are now also being developed for nonspherical active particles [13, 16, 40, 41], making knowledge of the pair-distribution function for such particles desirable. In a passive fluid, the pair-distribution function can be studied using liquid integral theory [32]. Methods of this type are, however, not applicable in active systems which are far from equilibrium. Therefore, the pair-distribution function of active particles is less well understood than that of passive ones.

Previous work on the pair-distribution function of active systems has focused on the case of spherical particles. This was investigated for both single-component systems [42] and multi-component systems [43], in both two [28] and three [44] spatial dimensions. Härtel *et al.* [45] have studied both the two-dimensional pair-distribution function and the three-body distribution, and Schwarzendahl and Mazza [46] considered effects of hydrodynamic interactions. What is still missing, however, is a fully orientation-resolved pair-distribution function – as obtained for spherical particles in Refs. [28, 44] – for systems of active ellipsoids.

In this article, we significantly extend the results discussed above by systematically investigating the collective dynamics of active ellipsoids via computer simulations. This allows to obtain the state diagram as a function of Pe and Φ_0 , which complements previous works focusing more on the influence of the particle shape and allows for an easier comparison to state diagrams for active spheres (which usually focus on the influence of Pe and Φ_0). A quantitative analysis allows to classify the observed states into cluster states, local polar order, polar flocks, and global disorder. Moreover, we numerically investigate the pair-distribution function of the active el-

* Corresponding author: raphael.wittkowski@uni-muenster.de

lipsoids, discuss in detail its symmetries and dependencies on distance and orientations, and obtain an analytical representation that can be used in further theoretical work.

This article is structured as follows: In Section II, we study the state diagram. The pair-distribution function is investigated in Section III. We conclude in Section IV. In the Appendix, we provide details on the particle interactions (Appendix A), the order parameters (Appendix B), and the fit parameters (Appendix C).

II. STATE DIAGRAM

We start by numerically investigating the state diagram of active ellipsoids.

A. State of the art

The state diagram of active ellipsoids is more complex than that of standard active Brownian particles (ABPs) since the anisotropic particle shapes allow for torques. This can lead to polarization and the emergence of nematic phases [47, 48]. Typically, MIPS is suppressed in systems of active ellipsoids compared to active spheres due to the torque interactions [13, 16]. When undergoing MIPS, spherical particles collide and hinder each other's movement. If this happens to multiple particles at once, an aggregate can form that other particles then collide with. Initially, particles on the outer layer swim towards the center of the newly forming cluster and exert an inward pressure onto the surface, thereby stabilizing the cluster [3, 49]. After some time, their orientations can change due to rotational diffusion, but other particles have already formed a new outer layer that adds pressure and traps the particles in the cluster.

The torque resulting from particle-particle interaction can suppress aggregation at an existing cluster's surface for nonspherical particles such as rods and ellipsoids moving along their long axes. An active ellipsoidal particle that is oriented roughly, but not perfectly, towards the center of a cluster will experience a torque that turns the particle's orientation away from the cluster's center and thereby prevents it from swimming towards there. This effect suppresses the cluster aggregation. Even minor anisotropies, like a length-to-diameter ratio of an elliptic particle such as $\kappa = a_{\text{el}}/b_{\text{el}} = 1.0424$ (with the length a_{el} , the diameter b_{el} , and the length-to-diameter ratio κ) can cause MIPS aggregates to dissolve [13].

However, torque can also enhance cluster formation. This effect was reported by Zhang *et al.* [50], who used spherical particles with an anisotropic interaction where repulsion is stronger at the rear of the particles than at the front. This leads to a torque turning the particles towards high-density areas, which enhances MIPS. While the torque resulting from the shape interaction inhibits MIPS, it can lead to the formation of other phases. These

were studied in recent work by Großmann *et al.* [13] and Jayaram *et al.* [16]. Großmann *et al.* [13] started with spherical particles undergoing MIPS and then changed the shape of the particles. It was found that even a cluster of spherical particles that has already formed can melt if the shape becomes slightly anisotropic. Increasing the length-to-diameter ratio further can lead to the emergence of local nematic order while the system is in global disorder. For even higher ratios (such as $\kappa = 1.96$), highly polarized domains with local nematic order emerge. Finally, extremely high anisotropies allow for the formation of a polar band with local smectic order. Similar findings were reported by Peruani *et al.* [30], who studied hard rods in an overall low-packing density environment and found highly polarized swarms. Jayaram *et al.* [16], who studied self-propelled ellipsoids, found that MIPS clusters become polar domains and polar bands for increasing anisotropies in the case of infinite Péclet numbers. The force imbalance coefficient – an order parameter that characterizes the asymmetry of the interaction force of a particle, an asymmetry that is the cause of MIPS – reduces for increasing anisotropies. Due to their movement, active particles collide; therefore, particle interaction hinders their movement. If the particles are elongated, they can slide past each other more easily and do not hinder each other's movement that much, which reduces the trapping effect that causes phase separation [21]. Rather than a persistent large single cluster as in the case of active spheres, one therefore observes a continuous appearance and disappearance of small clusters. This happens even for small anisotropies such as $\kappa = 1.15$ and in the absence of diffusion (infinite Péclet number). Further increasing the anisotropy, another state transition occurs, and a single, highly polarized cluster emerges. Also, recent experimental findings support that inter-particle torque and alignment of particles hinder MIPS and break full phase separation [17].

Even though we consider a wide range of Péclet numbers in our work, the active motion is dominant in all cases here. For substantially lower Péclet numbers (not considered here), the Brownian motion dominates and the collective dynamics differs. Nematic and smectic phases can also emerge [51]. For self-propelled rods at infinite Péclet numbers (also not considered here), dynamical states such as swarming, turbulence, and jamming can be found [31].

B. Equations of motion

The general equations of motion for uniaxial ABPs in two spatial dimensions that can be influenced by interactions, external fields, and orientation-dependent propulsion read [52]

$$\dot{\mathbf{r}}_i = \frac{D_T}{k_B T} \left(F_A \hat{\mathbf{u}}_i + \mathbf{F}_{\text{int},i}(\{\mathbf{r}_j, \hat{\mathbf{u}}_j\}) + \mathbf{F}_{\text{ext}}(\mathbf{r}_i) \right) + \boldsymbol{\xi}_T, \quad (1)$$

$$\dot{\varphi}_i = \frac{D_R}{k_B T} M_{\text{int},i}(\{\mathbf{r}_j, \hat{\mathbf{u}}_j\}) + \xi_R \quad (2)$$

with the center of mass position of the i -th particle \mathbf{r}_i , its orientation φ_i , the translational diffusion matrix \underline{D}_T , the Boltzmann constant k_B , the temperature T , the magnitude of the active propulsion force F_A , the normalized orientation vector $\hat{\mathbf{u}}_i$ corresponding to φ_i , the interaction force $\mathbf{F}_{\text{int},i}$ acting on the i -th particle where $\{\mathbf{r}_i, \hat{\mathbf{u}}_i\}$ denotes the set of all particles' positions \mathbf{r}_j and orientations $\hat{\mathbf{u}}_j$, the external force $\mathbf{F}_{\text{ext}}(\mathbf{r}_i)$, the translational Brownian noise ξ_T , the rotational diffusion coefficient D_R , the torque $M_{\text{int},i}$ acting on the i -th particle resulting from interactions with other particles, and the rotational Brownian noise ξ_R . We specify the interaction forces and torques in Appendix A.

As ellipsoids are anisotropic, their translational Brownian motion is also anisotropic [53]. The translational Brownian noise ξ_T is implemented by a random force with zero mean. The variances of its components k and l are given by $\langle \xi_{T,k}(t), \xi_{T,l}(t') \rangle = 2D_{T,kl}(\varphi(t))\delta(t-t')$ where $k, l \in \{x, y\}$ and $\delta(t-t')$ is the Dirac delta function. This approach has already been utilized for passive particles in Ref. [53] and active particles in Ref. [52]. Similarly, the rotational Brownian noise is a random torque with zero mean, which variance is given by $\langle \xi_R(t), \xi_R(t') \rangle = 2D_R\delta(t-t')$.

In this work, we focus on ellipsoids of revolution that have the same volume as a sphere with diameter σ_0 . The length of their axis of revolution, which is also referred to as the polar axis, is $a_{\text{el}} = 4^{1/3}\sigma_0$. The axes perpendicular to the polar axis, which will be referred to as the equatorial axes, have a length of $b_{\text{el}} = 2^{-1/3}\sigma_0$. This means that the ellipsoids have a length-to-diameter ratio $\kappa = 2$ and the same volume as a sphere of the same diameter. An ellipsoid's orientation is defined along its polar axis, which is also the direction of the propulsion force. Note that a_{el} and b_{el} denote the length and diameter of the full ellipsoids and should not be mistaken for the length of their respective semi-axes.

Brownian particles undergo diffusive motion [53, 54]. While translational diffusion is typically isotropic for spheres, it is anisotropic for ellipsoids. The diffusive motion depends on the diffusion constant, which is a scalar for spheres and a matrix for anisotropic particles. For uniaxial particles, such as ellipsoids, there are two different translational diffusion coefficients depending on the two hydrodynamic friction coefficients $\gamma_{T,\parallel}$ and $\gamma_{T,\perp}$. The friction coefficients correspond to the friction for movement parallel and perpendicular to the particles' polar and equatorial axes, respectively [53, 54]. Using the Einstein-Smoluchowski equation [55–57], these two friction coefficients lead to two diffusion coefficients. The diffusion matrix \underline{D}_T reads

$$\underline{D}_T = D_{T,\parallel}(\hat{\mathbf{u}} \otimes \hat{\mathbf{u}}) + D_{T,\perp}(\underline{I} - \hat{\mathbf{u}} \otimes \hat{\mathbf{u}}), \quad (3)$$

where \underline{I} is the two-dimensional identity matrix, $D_{T,\parallel} = k_B T / \gamma_{T,\parallel}$ the parallel diffusion coefficient, $D_{T,\perp} =$

$k_B T / \gamma_{T,\perp}$ the perpendicular diffusion coefficient, \otimes the dyadic product, and $\hat{\mathbf{u}}$ corresponds to the polar axis. The rotational diffusion coefficients D_R can be calculated using the Einstein-Smoluchowski equation [55–57]

$$D_R = k_B T / \gamma_R \quad (4)$$

where γ_R is the rotational friction coefficient of that particle.

C. Lennard-Jones units and dimensionless variables

In the simulations, we use Lennard-Jones units. Distance and energy are measured as multiples of the distance σ_0 and the energy ϵ (appearing in the interaction potential, see Appendix A), respectively. Friction coefficients are multiples of the friction coefficient $\gamma_{T,\text{sp}}$ of a sphere with diameter σ_0 . Thus, the Lennard-Jones time is given by $\tau_{\text{LJ}} = \sigma_0^2 \gamma_{T,\text{sp}} / \epsilon = \sigma_0^2 k_B T / (\epsilon D_{T,\text{sp}})$, where $D_{T,\text{sp}}$ is the diffusion coefficient of a sphere that has the same volume as the ellipsoid. All parameters are measured in this unit system. For example, the active propulsion force F_A is given by $F_A = 24\epsilon / \sigma_0$.

As in previous work [28, 44], we use two dimensionless variables to parametrize the state of the system, namely the Péclet number for ellipsoids Pe and the global packing density Φ_0 . The Péclet number is (following Ref. [22]) defined as

$$\text{Pe} = \frac{v_0}{a_{\text{el}} D_R}, \quad (5)$$

with the propulsion speed $v_0 = F_A D_{T,\parallel} / (k_B T)$ of the ellipsoids, which defines Pe via the ratio of persistence length v_0 / D_R and particle size a_{el} . In the limit of spherical particle shapes, Eq. (5) corresponds to the standard definition of the Péclet number for active spheres, except for a factor 3. The Péclet number can be changed by tuning either the temperature T or the propulsion force F_A . We chose to change the Péclet number by changing T as we would need to cope with a different effective size of the particles due to stronger propulsion when tuning the propulsion force. Changing the temperature T affects the translational and rotational diffusion and the Péclet number.

The global packing density is defined as $\Phi_0 = N_{\text{part}} A_{\text{part}} / A_{\text{sim}}$ with the number of particles in the system N_{part} , the area of a particle $A_{\text{part}} = a_{\text{el}} b_{\text{el}} \pi$, and the area of the simulation domain A_{sim} .

D. Simulation details

Since the influence of the particle shape on the collective dynamics has been studied thoroughly in previous work [21–23], we focus on the impact of Pe and Φ_0 for a fixed length-to-diameter ratio $\kappa = 2$. The state diagram is of interest by itself, but is also required to find the parameter combinations for which the particle distribution

stays homogeneous (which will later be used for obtaining the pair-distribution function). Thus, we performed computer simulations of active ellipsoids by numerically solving Eqs. (1) and (2) for different Péclet numbers Pe and global packing densities Φ_0 . Then, we classified the observed states.

The simulations were performed with a modified version of the molecular dynamics simulation package LAMMPS [58]. We modified the software package such that overdamped dynamics could be simulated. For integrating the equations of motion, we used the Euler-Maruyama method. The simulations start with random initial positions in a quadratic simulation domain with a side length of $128\sigma_0$ and periodic boundary conditions. Then, the particles are simulated for $500\tau_{LJ}$ with a time step size of $2 \cdot 10^{-5}\tau_{LJ}$. Note that this time step is used for all simulations. Further details regarding the computer simulations are given in Ref. [59].

E. Classification of states

The particle distributions obtained in the simulations for various values of Φ_0 and Pe are shown in Fig. 1. Each box shows an entire simulation domain. The coloring of the particles indicates their orientation. A red line is used to visualize the state borders. Note that, compared to those between MIPS and a homogeneous distribution for spherical particles, the borders between these phases are not sharp. The state diagram is shown in Figs. 2(a)-(c) with various order parameters (interaction energy per particle in Fig. 2(a), averaged local polarization divided by density in Fig. 2(b), and averaged local nematic order divided by density in Fig. 2(c)). Snapshots of the four states we distinguish between are shown in Fig. 2(d) (global disorder with local polar order), Fig. 2(e) (clusters with local polar order), Fig. 2(f) (global disorder), and Fig. 2(g) (polar flocks). Finally, the dependence of the order parameters on Pe (Figs. 2(h),(i)) and Φ_0 (Figs. 2(j)-(l)) is used to determine the state borders (see Section IIF).

We now discuss the classification of the observed states in more detail. In the regime of high densities and high Péclet numbers, we find polar clusters that collide with other polar clusters and thereby form larger clusters with different polar domains. Topological defects appear at the edges of the polar domains as the polar clusters collide, and dilute areas with low densities emerge. A larger snapshot in Fig. 2(e) shows an example of these polar clusters. Typically, these defects have a half-integer topological charge, as known for active nematics [13, 60, 61] (and nematics in general). Note that these structures are, in general, not stable as they are highly polarized, and polarization is coupled to mass transport in active matter. Although the interaction potential (see Appendix A) only includes nematic effects and does not explicitly include polar effects, polar order emerges. This is caused by the interplay of aligning torques and active propulsion,

as has also been found experimentally in the case of the gliding bacterium *Myxococcus xanthus* [62, 63].

Focusing on the density distribution at high Péclet numbers and packing densities and disregarding the particle orientations, one might assume that the small clusters are MIPS clusters, which are common in systems of spherical active particles. However, the clusters found here differ from MIPS clusters in two ways. First, the polar clusters are highly mobile due to their polarity and the resulting mass transport. Their movement even becomes more persistent as the orientation of the particles inside the cluster is stabilized due to the aligning interactions inside the cluster. In contrast, MIPS clusters only move via diffusion, decreasing their diffusivity with cluster size. The second difference is that the outer layer of MIPS clusters from spherical particles consists of particles pointing inwards and exerting pressure onto the particles inside the cluster [64, 65], which can also lead to a higher interaction energy [36]. On the other hand, the outer layers of particles in polar clusters are parallel to the interface between polar and nonpolar regions and, therefore, do not exert a pressure on the inner layers [13].

In the case of very high packing densities (such as $\Phi_0 = 0.75$), these polar regions also emerge for low Péclet numbers, but the system is in global disorder. There are few dilute areas, and the polar clusters are relatively small. A snapshot of this configuration is shown in Fig. 2(d). Note that topological defects can also arise in a nematic phase [25, 66, 67] and become more pronounced in confinement [68, 69]. When comparing low and high Péclet numbers at high packing densities, low Péclet numbers correspond to high temperatures and result in a system with global disorder and local polar order. In contrast, high Péclet numbers correspond to low temperatures, resulting in a more ordered system with polar clusters. This is similar to the observations made in Ref. [13], where it was found that small anisotropy leads to global disorder. Increasing the anisotropy of the particles increases the order in the system, and therefore polar clusters emerge.

If the overall packing density is low, polar clusters also emerge, but take up a substantial amount of the surrounding particles so that barely any other polar cluster exists. This means that it is rather unlikely for such a polar cluster to collide with another polar cluster, such that the clusters can move freely. The clusters are highly polarized, and topological defects are rare. An example is given in Fig. 2(g). Such moving polar clusters are also observed in biology, for example in flocks of birds and schools of fish [1, 4]. Spherical ABPs with polar alignment also exhibit polar clusters [70]. This behavior is also known for long-range orientation ordering as in the Vicsek model [4] and the Toner-Tu model [5, 6, 71, 72].

For low packing densities Φ_0 and low Péclet numbers Pe , the system is in a state of global disorder. The temperature is sufficiently high to destabilize polar clusters, and the occurrence of local polar order is prevented, as in the case of high densities. An example is shown in

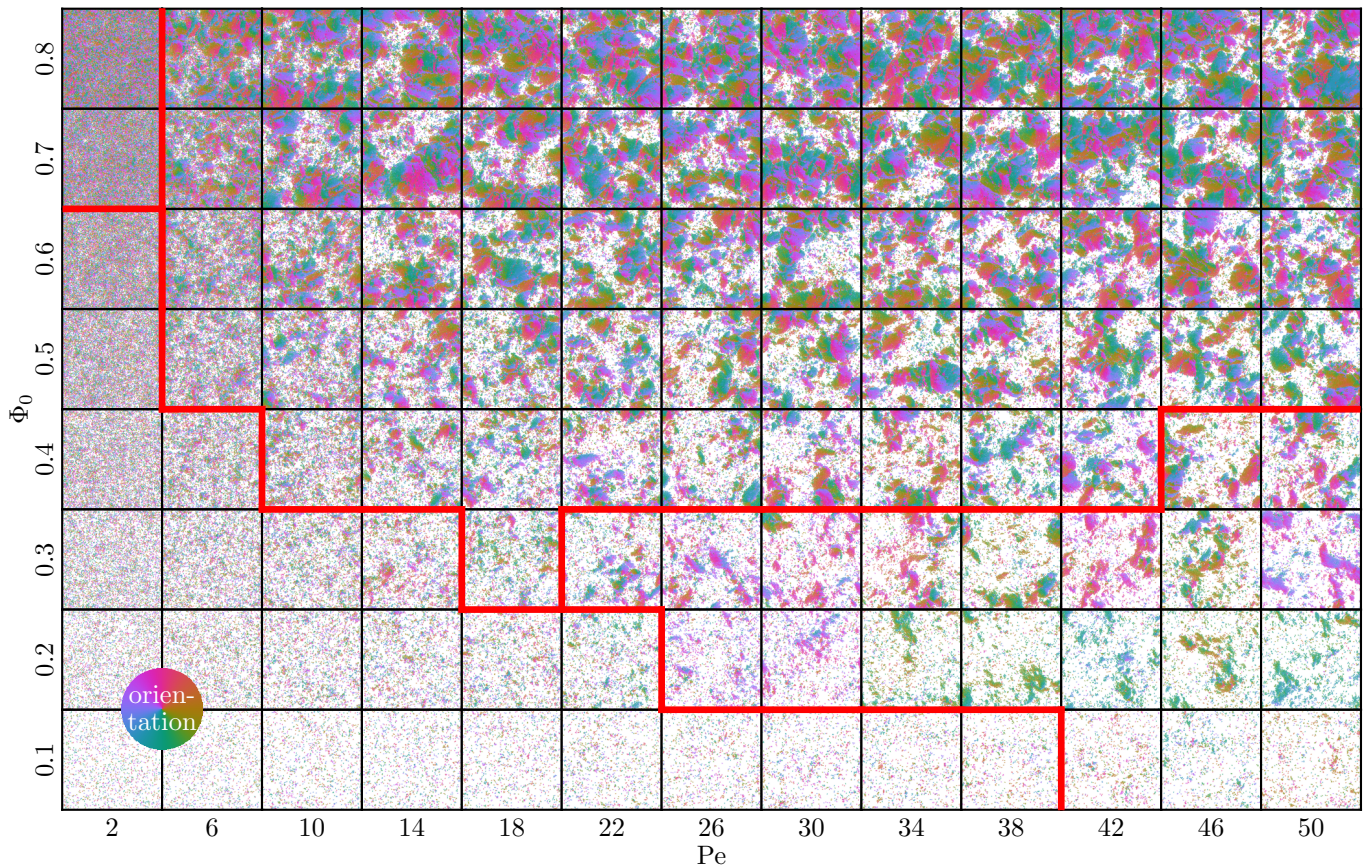


FIG. 1. Snapshots of particle distributions for different Péclet numbers Pe and packing densities Φ_0 . Each particle is colored according to its orientation. The system is in a disordered state for low Péclet numbers and low densities. Local polar order emerges for high packing densities and low Péclet numbers. For large Péclet numbers, polar flocks can be seen for low packing densities and polar domains for high packing densities. The red line corresponds to the borders between these different states obtained from order parameters shown in Fig. 2 and visual inspection.

Fig. 2(f). Small polar aggregates, which can also form in this state, are unstable.

F. Quantitative analysis of the state diagram

For a quantitative understanding, we need to analyze which parameter combinations correspond to which state. In particular, it is important to identify the parameter combinations that lead to a homogeneous distribution of the particles, as these will later be used to compute the pair-distribution function.

Visual inspection allows for this identification only to a certain degree. For an objective distinction of the states, the interaction energy per particle, the polarization, and the nematic order for different values of the overall density and Péclet number need to be calculated. As these variables scale with the number of particles, we calculate the reduced interaction energy per particle $E_{\text{int}}/(\epsilon N)$, the average local polarization divided by density $\langle \|\mathbf{P}\| \rangle / \Phi_0$, the average global polarization divided by density $\langle \langle \mathbf{P} \rangle \rangle / \Phi_0$, and the average nematic order di-

vided by density $\langle S \rangle / \Phi_0$. Here, $\|\cdot\|$ is the Euclidean norm. The interaction energy of the particles can be calculated straightforwardly from the interaction potential. Details regarding the definitions and calculations of the average local polarization, the average global polarization, and the average nematic order are given in Appendix B. Here, we briefly summarize their intuitive significance: The average local polarization increases if the particles form local polar clusters or polarized structures, i.e., if the particles locally have roughly the same orientation. Similarly, the averaged global polarization increases if the whole system is polarized, i.e., if all particles have roughly the same orientation. The emergence of nematic phases, even if only local, corresponds to an increased average nematic order, i.e., to (local) alignment or anti-alignment of the particles. We omit the terms “averaged” and “divided by density” of the order parameters from here on, i.e., we refer to the “averaged local orientation divided by density” just by “local polarization” (and similarly for other order parameters).

The interaction energy E_{int} , local polarization $\langle \|\mathbf{P}\| \rangle / \Phi_0$, and nematic order $\langle S \rangle / \Phi_0$ are shown in Figs.

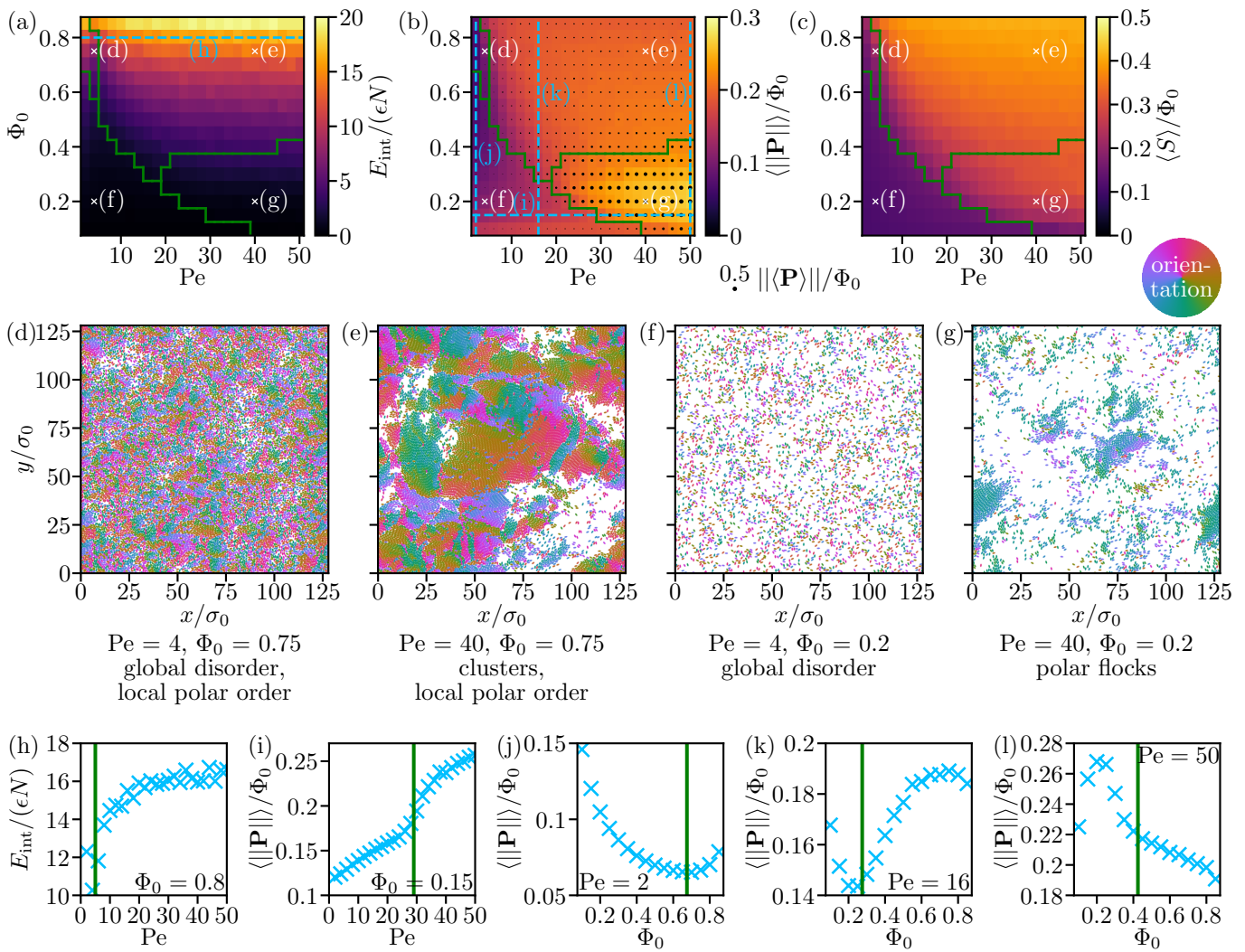


FIG. 2. **Top row:** State diagrams showing (a) interaction energy per particle $E_{\text{int}}/(\epsilon N)$, (b) local and global polarization divided by density, $\langle \|\mathbf{P}\| \rangle / \Phi_0$ and $\|\langle \mathbf{P} \rangle\| / \Phi_0$, respectively, and (c) average nematic order parameter divided by density $\langle S \rangle / \Phi_0$ as a function of Péclet number Pe and packing density Φ_0 . The green lines represent the state borders, determined by analyzing the order parameters and visual inspection. The cyan dashed lines represent exemplary cuts, for which the corresponding data is plotted in the bottom row in panels (h)-(l). **Middle row:** Exemplary snapshots of the different states of the system. The snapshots show (d) a disordered state with local polarization, (e) polarized clusters with topological defects and low-density areas, (f) a homogeneous distribution, and (g) two large polarized flocks. **Bottom row:** Example plots of the order parameters used to determine the state borders, showing (h) $E_{\text{int}}/(\epsilon N)$ as a function of Pe , (i) $\langle \|\mathbf{P}\| \rangle / \Phi_0$ as a function of Pe , and (j)-(l) $\|\langle \mathbf{P} \rangle\| / \Phi_0$ as a function of Φ_0 . The green lines represent the state borders. In the state diagrams in the top row, the cuts corresponding to these plots are marked by cyan lines.

2(a), (b), and (c), respectively. In Figs. 2(b), the global polarization $\|\langle \mathbf{P} \rangle\| / \Phi_0$ is shown as black dots. The area of the black dots scales linearly with the global polarization. We extract the values of the order parameters from the simulations. After discarding an initial $200\tau_{LJ}$ to allow for a relaxation of the system, we extracted the order parameters every τ_{LJ} for the remaining $300\tau_{LJ}$ of the simulation time. The order parameters are then used to determine borders between the different states in addition to visual inspection of the simulation results.

The state of global disorder, observed for low Péclet numbers and low packing densities, features neither high

interaction energies nor a measurable local or global polarization or a high nematic order as seen in Figs. 2(a)-(c). For low Péclet numbers, the local polarization of dilute systems ($\Phi_0 = 0.1$) is increased compared to systems with moderate densities ($\Phi_0 = 0.3$). As particle interactions become rare at low densities, the local polarization is not determined by multiple interacting particles but by single particles. Therefore, the local polarization barely depends on the Péclet number. However, for high Péclet numbers, the local and global polarization increase significantly.

The difference between the states of global disorder

with and without local polar order is the increased local polarization of the former one. Typically, for low Péclet numbers, an increase in density reduces the average local polarization. This is shown in Fig. 2(j), where the average local polarization is plotted against the density for $Pe = 2$. However, at a packing density of roughly $\Phi_0 \approx 0.65$, the polarization increases with the packing density. We consider this change of the dependence of the polarization on the density to be the border between the two states of global disorder with and without local polar order.

All order parameters represent a difference between the states of global disorder and clusters with local polar order (except for the global polarization, which is small in both phases). A significant increase in interaction energy, local polarization, and nematic order corresponds to this state border.

The interaction energy is a helpful order parameter to distinguish between clusters and global disorder with local polar order. As different polar clusters collide, the particles at the contact line are strongly pushed against each other, resulting in a high interaction energy. Note that there is a significant difference to the increased interaction energy of spherical particles in clusters [36, 73]: In MIPS clusters, the particles are pushed against each other due to boundary particles exerting pressure onto the particles inside, resulting in high pressure inside a MIPS cluster. In the case of ellipsoidal particles, however, there is no additional pressure from the outside layer because the particles at the outer layer are also aligned to the polarization of a cluster. The high interaction energy stems from the collision of polar clusters.

The border between global disorder with local polar order and clusters with local polar order is determined by the interaction energy. Both an increasing temperature (low Péclet numbers) and colliding polar clusters (high Péclet numbers) cause high interaction energies. Hence, the Péclet number for which the interaction energy starts to increase determines this border (cf. Fig. 2(h)). A transition line between global disorder and clusters can be identified by considering the local polarization as well as the nematic order. As an example, we plot in Fig. 2(k) the polarization as a function of Φ_0 . Figure 2(k) shows that, for small packing densities Φ_0 , the polarization decreases with increasing Φ_0 . For larger densities, in contrast, the polarization grows with Φ_0 . We place the border between the cluster and the global disorder phase at the point where the polarization has a local minimum as a function of Φ_0 , which is roughly at $\Phi_0 \approx 0.275$ for $Pe = 16$. This is similar to Fig. 2(j).

The state of polar flocks is characterized by a very high local polarization as well as a global polarization of the whole system. Since the global polarization only increases for polar flocks, it seems to be a convenient order parameter to characterize the system's state. However, the global polarization of a system depends on its size. The smaller the system, the easier it is to be globally polarized. Similarly, the local polarization depends on

the system size if the system size is small compared to the persistence length of the particles. In our case, the system size is sufficiently large to strongly reduce this dependence. Therefore, we choose the local polarization to determine the border between polar flocks and other states. When approaching the state of polar flocks, either from global disorder or from polarized clusters, a sharp increase in the local polarization occurs, which is shown in Figs. 2(i) and (l). Note that in Fig. 2(i) the state of polar flocks is approached when increasing Pe (from left to right in the figure), whereas in Fig. 2(l) it is approached for decreasing Φ_0 (from right to left in the figure).

The local polarization is also high for polar clusters. However, the numerous collisions and resulting topological defects decrease the local polarization, such that it is reduced compared to the case of polar flocks. Moreover, the snapshot in Fig. 2(e) shows many particles in clusters facing the opposite direction of the cluster's polarization. Thus, these particles increase the nematic order but strongly decrease local polarization. Particles facing the opposite direction of the clusters' polarization are extremely rare in the case of polar flocks.

III. PAIR-DISTRIBUTION FUNCTION

The classification of states developed in Section II reveals that the state of global disorder is the only one with translational and rotational symmetry. As our analysis of the pair-distribution function requires the state to possess these invariances, we restrict our attention to this state in the following.

Intuitively, the pair-distribution function g measures how likely it is to find a particle at a certain position in a certain state (in our case specified by the particle orientation $\hat{\mathbf{u}}$) given that another particle is at a certain position in a certain state. Thus, it is closely related (though not exactly identical) to a conditional probability. Formally, if $P(\{\mathbf{r}_i\}, \{\hat{\mathbf{u}}_i\}, t)$ is the probability for a system to be in the microscopic configuration given by the coordinates \mathbf{r}_i and $\hat{\mathbf{u}}_i$ at time t , the n -particle density can be defined as

$$\begin{aligned} \varrho^{(n)}(\mathbf{r}_1, \dots, \mathbf{r}_2, \hat{\mathbf{u}}_1, \dots, \hat{\mathbf{u}}_n, t) & \quad (6) \\ &= \frac{N!}{(N-n)!} \left(\prod_{i=n+1}^N \int_{\mathbb{R}^2} d^3 r_i \int_{\mathbb{S}_1} du_i \right) P(\{\mathbf{r}_i\}, \{\hat{\mathbf{u}}_i\}, t) \quad (7) \end{aligned}$$

with the unit sphere \mathbb{S}_1 in two spatial dimensions. We can then further define the pair-distribution function g as [32]

$$g(\mathbf{r}_1, \mathbf{r}_2, \hat{\mathbf{u}}_1, \hat{\mathbf{u}}_2, t) = \frac{\varrho^{(2)}(\mathbf{r}_1, \mathbf{r}_2, \hat{\mathbf{u}}_1, \hat{\mathbf{u}}_2, t)}{\varrho^{(1)}(\mathbf{r}_1, \hat{\mathbf{u}}_1, t) \varrho^{(1)}(\mathbf{r}_2, \hat{\mathbf{u}}_2, t)}. \quad (8)$$

Given the definitions (7) and (8), $\varrho^{(1)}(\mathbf{r}_2, \hat{\mathbf{u}}_2, t) g(\mathbf{r}_1, \mathbf{r}_2, \hat{\mathbf{u}}_1, \hat{\mathbf{u}}_2, t) / (N-1)$ is the conditional probability of finding a particle at position \mathbf{r}_2 with orientation $\hat{\mathbf{u}}_2$ at time t given that there is another particle at the position \mathbf{r}_1 with the orientation $\hat{\mathbf{u}}_1$ [74] at

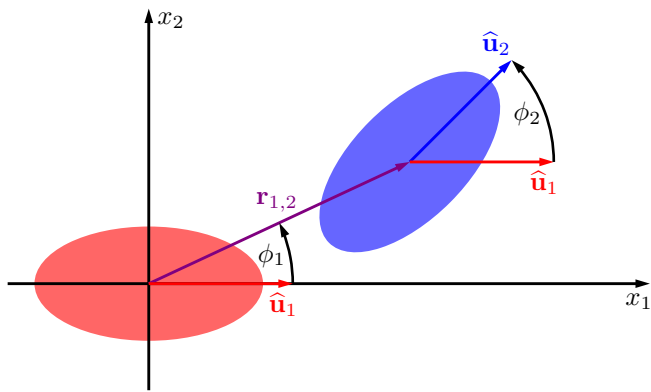


FIG. 3. Coordinate system used to parameterize the pair-distribution function $g(r, \phi_1, \phi_2)$. The vector $\mathbf{r}_{1,2} = \mathbf{r}_2 - \mathbf{r}_1$ points from the center of the first particle (red) to the center of the second particle (blue). The relative position of the second particle is determined by the length $r = \|\mathbf{r}_{1,2}\|$ of $\mathbf{r}_{1,2}$ and the angle ϕ_1 between $\mathbf{r}_{1,2}$ and the orientation unit vector $\hat{\mathbf{u}}_1$ of the first particle. The orientation of the second particle $\hat{\mathbf{u}}_2$ is given by the angle ϕ_2 between $\hat{\mathbf{u}}_2$ and $\hat{\mathbf{u}}_1$.

the same time. A more detailed explanation is given in Ref. [44]. For the sake of simplicity, we will often (with slight abuse of terminology) refer to g as a “probability” or “probability modification”.

A. Parameterization of the pair-distribution function

Next, we simplify the dependence of g on the positions and orientations of the particles. In general, the pair-distribution function g depends on two position and orientation vectors and on time t . The function g will generally take a different form for different values of Pe and Φ_0 , i.e., it depends also on these parameters. In two spatial dimensions, g thereby depends on 9 independent variables.

To simplify the pair-distribution function, we assume that it satisfies translational and rotational invariance and that it does not depend on time. These conditions are satisfied in a homogeneous state where phase separation does not occur, which is why we numerically examine the pair-distribution function of active ellipsoids under these conditions. Given translational and rotational invariance, g can only depend on the relative positions and orientations of the particles. We introduce a new coordinate system whose origin is located at the center of mass position of the first particle \mathbf{r}_1 , and align the x_1 -axis of the new coordinate system with the orientation $\hat{\mathbf{u}}_i$ of this particle. This coordinate system is visualized in Fig. 3. The relative position of the second particle $\mathbf{r}_{1,2}$ is parameterized as

$$\mathbf{r}_2 - \mathbf{r}_1 = r\hat{\mathbf{u}}(\phi_1) \quad (9)$$

with the norm

$$r = \|\mathbf{r}_{1,2}\| = \|\mathbf{r}_2 - \mathbf{r}_1\| \quad (10)$$

and the angle ϕ_1 between $\mathbf{r}_{1,2}$ and the orientation of the first particle $\hat{\mathbf{u}}_1$. With the angle $\varphi_{1,2}$ between the center-to-center vector $\mathbf{r}_{1,2}$ and the x_1 -axis, ϕ_1 is given by

$$\phi_1 = \varphi_{1,2} - \varphi_1. \quad (11)$$

The orientation of the second particle is parameterized by the angle ϕ_2 between the orientation unit vectors $\hat{\mathbf{u}}_2$ and $\hat{\mathbf{u}}_1$, resulting in

$$\phi_2 = \varphi_2 - \varphi_1. \quad (12)$$

Therefore, $g(\text{Pe}, \Phi_0; r, \phi_1, \phi_2)$ depends on the three variables r , ϕ_1 , and ϕ_2 and the two parameters Pe and Φ_0 . It has the symmetry property

$$g(\text{Pe}, \Phi_0; r, \phi_1, \phi_2) = g(\text{Pe}, \Phi_0; r, -\phi_1, -\phi_2). \quad (13)$$

B. Pair-distribution function of active Brownian ellipsoids

Now, we investigate g for fixed system parameters Pe and Φ_0 . To this end, we set the Péclet number to $\text{Pe} = 4$ and the packing density to $\Phi_0 = 0.2$, which corresponds to the setting shown in Fig. 2(f), i.e., the state of global disorder. In this section, we omit the explicit dependence on Pe and Φ_0 in our notation for brevity. To explicitly calculate g , we perform Brownian dynamics simulations in a quadratic simulation domain with side length $256\sigma_0$ and a total simulation time of $550\tau_{\text{LJ}}$. We initialize the system with random particle positions and omit the first $50\tau_{\text{LJ}}$. After that, the values of the positions and orientations of the particles are extracted every $0.1\tau_{\text{LJ}}$. To improve the statistics, we repeat this procedure 10 times. For evaluating g from the simulations, a sampling of 180 data bins for both angles ϕ_1 and ϕ_2 is used. The distance r is measured with an accuracy of $0.005\sigma_0$ for all values of $r < 3\sigma_0$ and with an accuracy of $0.05\sigma_0$ for $3\sigma_0 < r < 10\sigma_0$. See Ref. [59] for further details on the calculation of g .

The pair-distribution function g depends on three parameters. Therefore, one of these parameters has to be fixed to visualize the dependence on the other two parameters. Figure 4 shows $g(r, \phi_1, \phi_2)$ as a function of r and ϕ_1 for fixed values of ϕ_2 . High values of g typically result from two (not mutually exclusive) causes. First, if a particle constellation occurs often, independent of the stability of this constellation, the corresponding value of g is increased. Second, g has a high value for very stable constellations. Both of these causes increase the probability of a constellation being measured in the simulation, and thereby the corresponding values of g .

Figure 4(a) shows the integral of g over the second particle's orientation ($\int d\phi_2 g(r, \phi_1, \phi_2)$), which corresponds

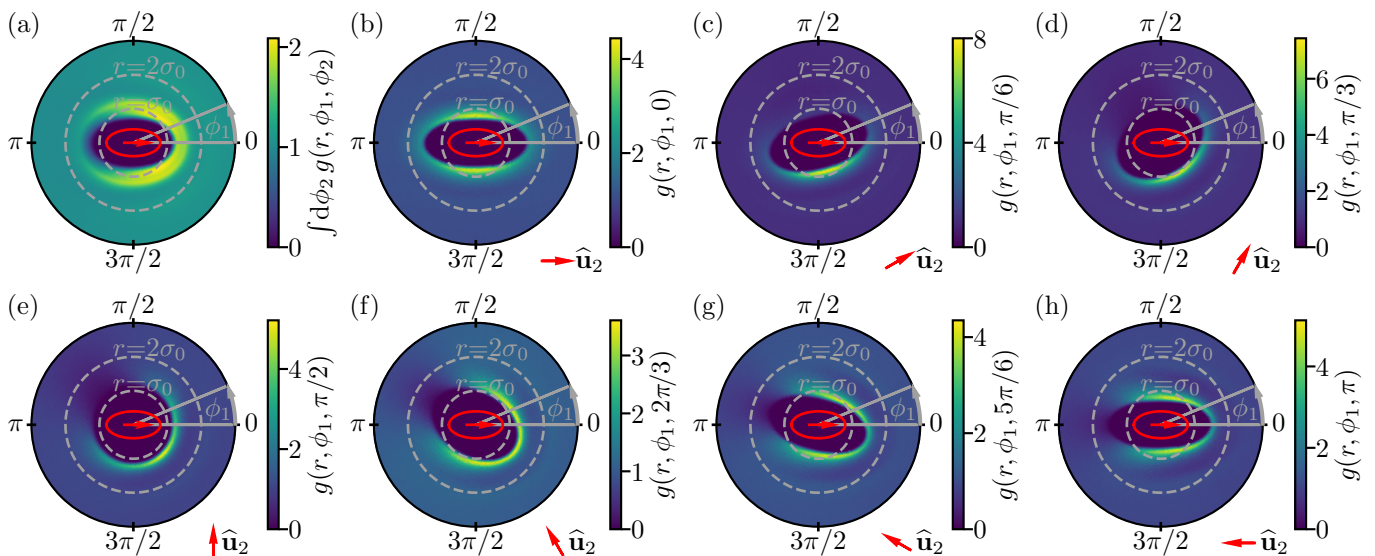


FIG. 4. Pair-distribution function of active Brownian ellipsoids for the Péclet number $Pe = 4$ and the packing density $\Phi_0 = 0.2$. (a) g integrated over the orientation of the second particle. This corresponds to the probability modification of finding a second particle independent of the second particle's orientation. (b)-(h) $g(r, \phi_1, \phi_2)$ for different fixed values of ϕ_2 . The red vectors in each bottom right corner show the orientation of the second particle. The values of $\phi_2 \in (-\pi, 0)$ are omitted due to the symmetry of g [cf. Eq. (13)].

to the modification of the probability of finding a second particle with any orientation at the relative position denoted by r and ϕ_1 . In the center of the plot, at very small values of r , an area with the shape of an ellipsoid is visible, where the values are zero. The interaction force of the particles allows for minor overlapping, but for strong overlapping, the interaction force becomes extremely strong, preventing two particles at the same location. Hence, the smallest values of r for which g is nonzero correspond to the distance r for which the particles are touching. This distance depends on ϕ_1 since the particles are anisotropic. At $\phi_1 \approx 0$ and $\phi_1 \approx \pi$, the values for r are roughly $r \approx 1.2\sigma_0$ which equals the sum of the major and minor semiaxes $(a_{el} + b_{el})/2 \approx 1.2\sigma_0$. For $\phi_1 \approx \pi/2$ and $\phi_2 \approx 3\pi/2$, the smallest value of r with a nonzero g is roughly $r \approx 0.8\sigma_0$ which equals $(b_{el} + b_{el})/2 \approx 0.8\sigma_0$. As a general rule of thumb, regarding any ϕ_1 , the smallest value of r with a probability unequal to zero is typically the sum of the size of the ellipsoid at this ϕ_1 and the minor semi axis b_{el} . The size of the reference particle is also shown in the figure.

The probability of finding another particle is roughly doubled in the proximity in front of and next to a reference particle. This is a typical feature of ABPs [28, 46, 75]. Furthermore, the area with increased probability is relatively large compared to that of spheres [75]. This area consists of two maxima with a local minimum in the center. For $\phi_1 \approx 0$, one local local maximum is at $r = (a_{el} + b_{el})/2$ and the other maximum is at $r = 2a_{el}/2$. There is a (barely visible) local minimum between these local maxima. Configurations where the particles touch have an increased probability, in particular if the particles are parallel or perpendicular to each other. The proba-

bility is increased by a small amount at $r \approx 2\sigma_0$ because particles sometimes form small local structures. The distance $r \approx 2\sigma_0$ corresponds to the next but one particle. This is again very similar to the case of spheres [76], but the effect is weaker as the maximum is less pronounced due to the anisotropy of the shape.

In Figs. 4(b)-(h), the pair-distribution function g is shown for different fixed angles of the second particle's orientation ϕ_2 . Figure 4(b) shows $g(r, \phi_1, 0)$, i.e., the case where the second particle is parallel to the reference particle. The probability is strongly increased for particles close to the reference particle, i.e., angles $\phi_1 = \pi/2$ and $\phi_1 = 3\pi/2$. Note also that the area in the center, where the values of g are zero, adapts the particle shape. As we only consider parallel particles in Fig. 4(b), the values of r at which the particles would severely overlap strongly depend on ϕ_1 . At $\phi_1 \approx 0$ and $\phi_1 \approx \pi$, the lowest value of r for which another particle is found is $r \approx 2a_{el}/2$, i.e., twice the major semi axis, and for $\phi_1 \approx \pi/2$ and $\phi_1 \approx 3\pi/2$, it is $r \approx 2b_{el}/2$, i.e., twice the minor semi axis. For Figs. 4(b)-(h), the shape of the area with $g = 0$ depends on the second particle's orientation as strong overlapping is not possible.

Suppose that we fix the reference particle in the center and move the other particle around the reference particle with a stationary orientation while maintaining contact between the particles. In that case, the resulting path of the center of the second particle determines the shape of the inner low probability zone. For parallel particles, this results in a thin ellipse (cf. Figs. 4(b) and (h)), and for perpendicular particles, the resulting area is nearly a perfect circle as shown in Fig. 4(e). Other orientations lead to a shape similar to a rotated ellipse. In cases

where the particles are roughly pointing in the same direction, like the ones shown in Fig. 4(c) ($\phi_2 = \pi/6$) and (d) ($\phi_2 = \pi/3$), the highest probability peaks are located where the particles push into each other's paths. Both particles swim against each other, resulting in a relatively stable position. In the case of perpendicular particles as in Fig. 4(e) ($\phi_2 = \pi/2$), the highest probability peaks also occur where the particles collide. If the particles point roughly in opposite directions, the maximum is instead found for a constellation resulting from a collision. For example, in Fig. 4(g) ($\phi_2 = 5\pi/6$) the maximum values of g correspond to particles passing each other at a close distance. A similar effect can be observed in Fig. 4(h) and is also known for spheres [28]. Particle constellations resulting from a previous collision have an enhanced probability of occurring. Furthermore, particles pointing in opposing directions tend to form a probability shadow (a region of locally decreased probability). This results from the fact that particle constellations that can only arise if particles have moved through each other (which is not possible for the interaction potential used here) are very unlikely. An example is shown in Fig. 4(e), where the values of g are low for $\phi_1 \approx 3\pi/4$. This probability shadow has also been observed for spherical ABPs [28, 46, 75, 77]. The depletion zone behind an ABP arises for particles with opposite orientations as in Figs. 4(g) and (h). In contrast, this depletion zone barely exists if the particles are parallel as in Fig. 4(b) and (c). Here, the probability of finding a particle directly behind another one is increased.

Another way to show the different characteristics of g is to fix the distance parameter r and then display the dependence of g on ϕ_1 and ϕ_2 , as done in Refs. [28, 44] for spherical particles. Such a plot can help to answer two questions:

- (i): For a certain center-to-center distance, what are the typical angle constellations corresponding to high and low values of g ?
- (ii): How complex is the structure of g with respect to the dependence on the angles?

The latter question is essential when looking for an analytical approximation for g , which will be considered later using the Fourier approximation model for the dependence on the angles. The pair-distribution function g for different center-to-center distances r is shown in Fig. 5. In the case of minimal distances $r = 0.8\sigma_0$ (cf. Fig. 5(a)), particles are only found if both particles are parallel or anti-parallel and the second particle is next to the reference particle. In other words, their minor semi axes create a straight line. The parallel case ($\phi_2 \approx 0$ and $\phi_2 \approx 2\pi$) has a higher probability than the anti-parallel case as it is more stable. At slightly higher distances $r = \sigma_0$, $r = 1.2\sigma_0$, and $r = 1.4\sigma_0$, as shown in Figs. 5(b), (c), and (d), similar angular constellations correspond to local maxima of g . The maxima become broader, and a local minimum emerges at their centers. At higher distances, a larger range of angles is possible without the particles overlapping too strongly. Addition-

ally, the difference between the parallel and anti-parallel cases becomes more pronounced. The maxima of g are not symmetric. Instead, higher values are found if the absolute value of ϕ_1 is scarcely smaller than $\pi/2$, which means that the second particle is minimally further ahead than the reference particle. The values of g are also increased if the second particle points towards the first particle's path ahead, corresponding to values of $\phi_2 \approx \pi/4$ for $\phi_1 = -\pi/4$. The observation that local maxima tend to widen up, and local minima emerge in between for increasing distances has also been made for spherical particles in two [28] and three [44] dimensions. At distances close to $a_{el} \approx 1.6\sigma_0$ as shown in Fig. 5(e), a local maximum is found for two particles swimming straight into each other with $\phi_1 = 0$ and $\phi_2 = \pi$ and a local minimum emerges for $\phi_1 = \pi$ and $\phi_2 = \pi$. The latter corresponds to a constellation that would require the particles to move through each other. If both particles have the same orientation ($\phi_2 = 0$), local maxima can be found for $\phi_1 = 0$ and $\phi_1 = \pi$. If the particles are parallel, the constellation where both particles swim right behind each other has an increased probability. Also, as $r = 1.6\sigma_0$ is slightly larger than $a_{el} = 4^{1/3}\sigma_0$, a very thin local minimum emerges inside the maximum. At high distances such as $r = 2\sigma_0$ and $r = 3\sigma_0$ shown in Figs. 5(g) and (h), respectively, the angular dependence of g slowly vanishes. Even for $r = 3\sigma_0$, the probability of the constellation of $\phi_1 = \pi$ and $\phi_2 = \pi$, which results from two particles passing through each other, is significantly decreased. The general asymmetry of the maxima and minima distribution is similar to the spherical case [28, 44] and a result of the co-dependence of the angles. Stable constellations correspond to high values of g , but a constellation with an offset in the position angle ϕ_1 is not particularly stable. However, if the orientation of the second particle compensates for the offset, the constellation can be stable. Therefore, the maxima are distorted. The same explanation can be used for the distortion of the minima in Fig. 5(h). The minima correspond to constellations of two particles that can arise only if they pass through each other. If the second particle's position is not exactly at $\phi_1 = \pi$, but slightly different (say, $\phi_1 = \pi + \alpha$ with a small angle α), the minimum is located at a slightly different orientation angle $\phi_2 \approx \pi + 2\alpha$. The additional factor of 2 stems from the fact that the reference particle is also moving. If the reference particle was not moving, the setting $\phi_1 = \pi + \alpha$ and $\phi_2 = \pi + \alpha$ would correspond to the second particle having moved through the reference particle. However, as the reference particle is also active, the angles must be adjusted accordingly.

C. Analytical approximation of the pair-distribution function

The pair-distribution function often appears in microscopic field-theoretical models for active matter [28, 32, 34–37, 39], and an analytical expression for this func-

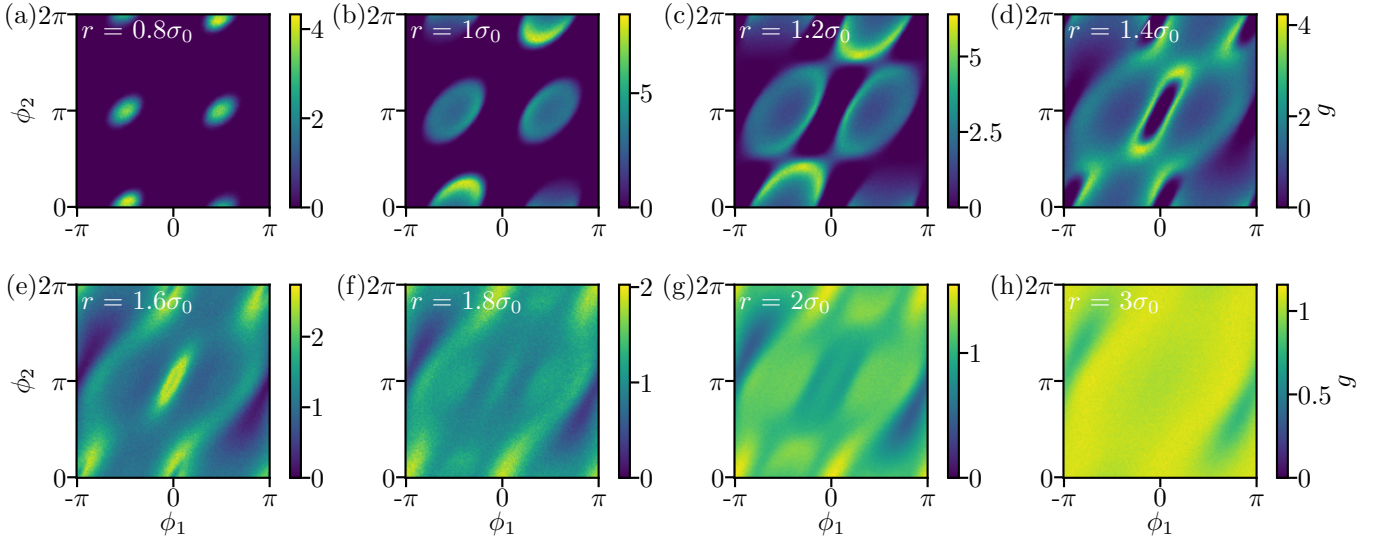


FIG. 5. Pair-distribution function of active Brownian ellipsoids for fixed Péclet number $Pe = 4$ and packing density $\Phi_0 = 0.2$ and for different values of the center-to-center distance r . This corresponds to the probability modification of finding a second particle at a certain distance r depending on the position angle ϕ_1 and the orientation angle ϕ_2 . The plots show a point symmetry with respect to $\phi_1 = 0$ and $\phi_2 = \pi$ due to the symmetry of g of [cf. Eq. (13)].

tion is needed in order to derive them in a closed form [33]. Therefore, we here determine an analytical expression for g that is valid for a wide range of Péclet numbers and packing densities. For this purpose, we first use the 2π -periodicity of $g(Pe, \Phi_0; r, \phi_1, \phi_2)$ regarding the angles ϕ_1 and ϕ_2 and perform the real Fourier expansion

$$g(Pe, \Phi_0; r, \phi_1, \phi_2) = \sum_{h,j=0}^{\infty} \sum_{k,l=1}^2 a_{h,j}^{k,l}(Pe, \Phi_0; r) w_k(h\phi_1) w_l(j\phi_2) \quad (14)$$

with the functions

$$w_1(x) = \cos(x), \quad (15)$$

$$w_2(x) = \sin(x) \quad (16)$$

and the real Fourier coefficients $a_{h,j}^{k,l}(Pe, \Phi_0; r)$ which depend on the system parameters Pe and Φ_0 and the distance r . The Fourier coefficients $a_{h,j}^{k,l}(Pe, \Phi_0; r)$ are given by

$$a_{h,j}^{k,l}(Pe, \Phi_0; r) = \frac{1}{\pi^2} \int_0^{2\pi} d\phi_1 \int_0^{2\pi} d\phi_2 g(Pe, \Phi_0; r, \phi_1, \phi_2) w_k(h\phi_1) w_l(j\phi_2) \frac{1}{2^{\delta_{h,0} + \delta_{j,0}}} \quad (17)$$

with the Kronecker delta δ_{ij} . Further details on the Fourier calculation of discrete data of a histogram are given in Ref. [59]. As the pair-distribution function g has the symmetry property

$$g(Pe, \Phi_0; r, \phi_1, \phi_2) = g(Pe, \Phi_0; r, -\phi_1, -\phi_2), \quad (18)$$

the resulting Fourier representation has the same symmetry, such that the coefficients $a_{h,j}^{1,2} = a_{h,j}^{2,1}$, which correspond to a product of a sin and a cos function in the Fourier expansion, vanish:

$$a_{h,j}^{1,2} = a_{h,j}^{2,1} = 0 \quad \forall h, j. \quad (19)$$

The coefficients that represent either two sin functions or two cos functions remain. This leaves g as

$$g(Pe, \Phi_0; r, \phi_1, \phi_2) = \sum_{h,j=0}^{\infty} \sum_{k=1}^2 a_{h,j}^{k,k}(Pe, \Phi_0; r) w_k(h\phi_1) w_k(j\phi_2). \quad (20)$$

In the cases of spheres [28, 44], the angular dependence of g can be represented reasonably accurately by a Fourier expansion truncated at second order. In the case of ellipsoids, the angular dependence is more complex, and we use the Fourier modes up to third order:

$$g(Pe, \Phi_0; r, \phi_1, \phi_2) \approx \sum_{h,j=0}^3 \sum_{k=1}^2 a_{h,j}^{k,k}(Pe, \Phi_0; r) w_k(h\phi_1) w_k(j\phi_2). \quad (21)$$

As the zero-frequency contribution of the sin functions vanishes, we find

$$a_{0,j}^{2,2} = 0 \quad \forall j, \quad (22)$$

$$a_{k,0}^{2,2} = 0 \quad \forall k. \quad (23)$$

We can therefore represent the approximation as

$$g(\text{Pe}, \Phi_0; r, \phi_1, \phi_2) \approx \sum_{h,j=0}^3 a_{h,j}^{1,1}(\text{Pe}, \Phi_0; r) \cos(h\phi_1) \cos(j\phi_2) + \sum_{h,j=1}^3 a_{h,j}^{2,2}(\text{Pe}, \Phi_0; r) \sin(h\phi_1) \sin(j\phi_2) \quad (24)$$

with a total of $16 + 9 = 25$ Fourier coefficients. To obtain a full analytical representation of g that is not only valid for specific values of r , Pe , and Φ_0 , we examine the dependence of every Fourier coefficient on r for all combinations of Pe and Φ_0 and fit it via suitable functions.

How complex the dependence of g on r is depends strongly on the parameters Pe and Φ_0 . Since we wish to choose the same functional form for all values of these parameters, choosing a functional form that is a good representation of g for parameter values where g is a complicated function may lead to overfitting in parameter regions where g is simpler. To avoid problems related to overfitting, we here choose a function that is adapted to the shape that g has in regions where it is a simple function of r . As a particle at \mathbf{r}_1 does not affect particles at a position \mathbf{r}_2 far away ($\|\mathbf{r}_2 - \mathbf{r}_1\| \gg \sigma_0$), the pair-distribution function g converges to 1 for very large distances. Thus, all Fourier coefficients must vanish for large r except for $a_{0,0}^{1,1}$, which must converge to one. All Fourier coefficients must converge to zero for small values of r since two particles cannot be at the same location.

Many Fourier coefficients can be well represented by either a product of the exponentially modified Gaussian distribution function (EMG function) and a polynomial or the product of a Gaussian function and a polynomial. The EMG function is given by

$$\text{EMG}(r; \mu, \varsigma, \lambda) = \frac{\lambda}{2} \exp\left(\frac{\lambda}{2}(\lambda\varsigma^2 - 2(r - \mu))\right) \text{erfc}\left(\frac{\lambda\varsigma^2 - (r - \mu)}{\sqrt{2}\varsigma}\right), \quad (25)$$

where μ , ς , and λ are the mean value, standard deviation, and control parameter of the skewness of the distribution, respectively, and erfc is the complementary error function

$$\text{erfc}(x) = \frac{2}{\pi} \int_x^\infty dt \exp(-t^2). \quad (26)$$

The EMG function is similar to the Gaussian function

$$f_G(r; \mu, \varsigma) = \frac{1}{\varsigma\sqrt{2\pi}} \exp\left(\frac{-(r - \mu)^2}{2\varsigma^2}\right), \quad (27)$$

where the parameter λ is used to skew the function. For the coefficient $a_{0,0}^{1,1}$, which is supposed to converge to one for very large r , a sum of the EMG function and the tangens hyperbolicus

$$\tanh(x) = \frac{\exp(x) - \exp(-x)}{\exp(x) + \exp(-x)} \quad (28)$$

Fourier coefficient	fit function
$a_{0,0}^{1,1}$	$a \text{EMG}(r; \mu, \varsigma, \lambda) + \tanh((r - \mu)l_1)/2 + 0.5$
$a_{0,1}^{1,1}$	$a_1 f_{\text{Gauss}}(r; \mu_1, \varsigma_1) + a_2 f_{\text{Gauss}}(r; \mu_2, \varsigma_2)$
$a_{0,2}^{1,1}$	$a \text{EMG}(r; \mu, \varsigma, \lambda)(r^2 + l_1 r + l_2)$
$a_{0,3}^{1,1}$	$a f_{\text{Gauss}}(r; \mu, \varsigma)$
$a_{1,0}^{1,1}$	$a \text{EMG}(r; \mu, \varsigma, \lambda)(r^2 + l_1 r + l_2)$
$a_{1,1}^{1,1}$	$a \text{EMG}(r; \mu, \varsigma, \lambda)(r^2 + l_1 r + l_2)(r - l_3)$
$a_{1,2}^{1,1}$	$a \text{EMG}(r; \mu, \varsigma, \lambda)(r^2 + l_1 r + l_2)(r - l_3)$
$a_{1,3}^{1,1}$	$a f_{\text{Gauss}}(r; \mu, \varsigma)$
$a_{2,0}^{1,1}$	$a \text{EMG}(r; \mu, \varsigma, \lambda)(r - l_1)(r - l_2)$
$a_{2,1}^{1,1}$	$a \text{EMG}(r; \mu, \varsigma, \lambda)(r - l_1)$
$a_{2,2}^{1,1}$	$a \text{EMG}(r; \mu, \varsigma, \lambda)(r - l_1)$
$a_{2,3}^{1,1}$	$a f_{\text{Gauss}}(r; \mu, \varsigma)$
$a_{3,0}^{1,1}$	$a \text{EMG}(r; \mu, \varsigma, \lambda)(r - l_1)(r - l_2)(r - l_3)$
$a_{3,1}^{1,1}$	$a f_{\text{Gauss}}(r; \mu, \varsigma)(r - l_1)(r - l_2)$
$a_{3,2}^{1,1}$	$a \text{EMG}(r; \mu, \varsigma, \lambda)(r - l_1)$
$a_{3,3}^{1,1}$	$a \text{EMG}(r; \mu, \varsigma, \lambda)(r - l_1)(r - l_2)$
$a_{2,2}^{2,2}$	$a \text{EMG}(r; \mu, \varsigma, \lambda)(r^2 + l_1 r + l_2)$
$a_{2,2}^{2,2}$	$a \text{EMG}(r; \mu, \varsigma, \lambda)(r^2 + l_1 r + l_2)$
$a_{2,2}^{2,2}$	$a \text{EMG}(r; \mu, \varsigma, \lambda)(r - l_1)(r - l_2)$
$a_{2,2}^{2,2}$	$a \text{EMG}(r; \mu, \varsigma, \lambda)(r - l_1)$
$a_{2,2}^{2,2}$	$a \text{EMG}(r; \mu, \varsigma, \lambda)(r - l_1)(r - l_2)$
$a_{2,2}^{2,2}$	$a \text{EMG}(r; \mu, \varsigma, \lambda)(r - l_1)(r - l_2)$
$a_{2,3}^{2,2}$	$a f_{\text{Gauss}}(r; \mu, \varsigma)(r - l_1)(r - l_2)$
$a_{3,1}^{2,2}$	$a f_{\text{Gauss}}(r; \mu, \varsigma)(r - l_1)$
$a_{3,2}^{2,2}$	$a \text{EMG}(r; \mu, \varsigma, \lambda)(r - l_1)(r - l_2)$
$a_{3,3}^{2,2}$	$a \text{EMG}(r; \mu, \varsigma, \lambda)(r - l_1)(r - l_2)$

TABLE I. Table of the fit functions used for the Fourier coefficients of the pair-distribution function appearing in Eq. (21).

is used. The argument of the tanh function is shifted to the center of the EMG function and multiplied by an additional fit parameter that controls its steepness. Also, the tanh is shifted and scaled to the range of $[0, 1]$. The fit functions for the other Fourier coefficients are chosen on an empirical basis by investigating their behavior for all values of Pe and Φ_0 . The most suitable functions for each Fourier coefficient are shown in Table I. We use these functions to fit every Fourier coefficient for every combination of Pe and Φ_0 that corresponds to the state of global disorder as shown in Fig. 2.

Due to its additional fitting parameter, the EMG function usually reproduces a single function better than the Gaussian distribution. Still, as the courses of the Fourier coefficients differ strongly in some cases, the fitting procedure of the EMG function is unstable for some system parameters. In these cases, the Gaussian distribution is chosen.

The Fourier coefficients extracted from simulation data and the fitting results for the Péclet number $\text{Pe} = 10$ and packing density $\Phi_0 = 0.2$ are shown in Fig. 6. Although we calculate g for the range $0 < r < 10\sigma_0$ and fitted this entire interval, in Fig. 6 we focus on $0 < r < 3\sigma_0$ as the Fourier coefficients show the most interesting behavior in this range. This fitting procedure leaves us with fit parameters for each combination of Pe and Φ_0 . Hence, we offer an analytical representation of g for a discrete set

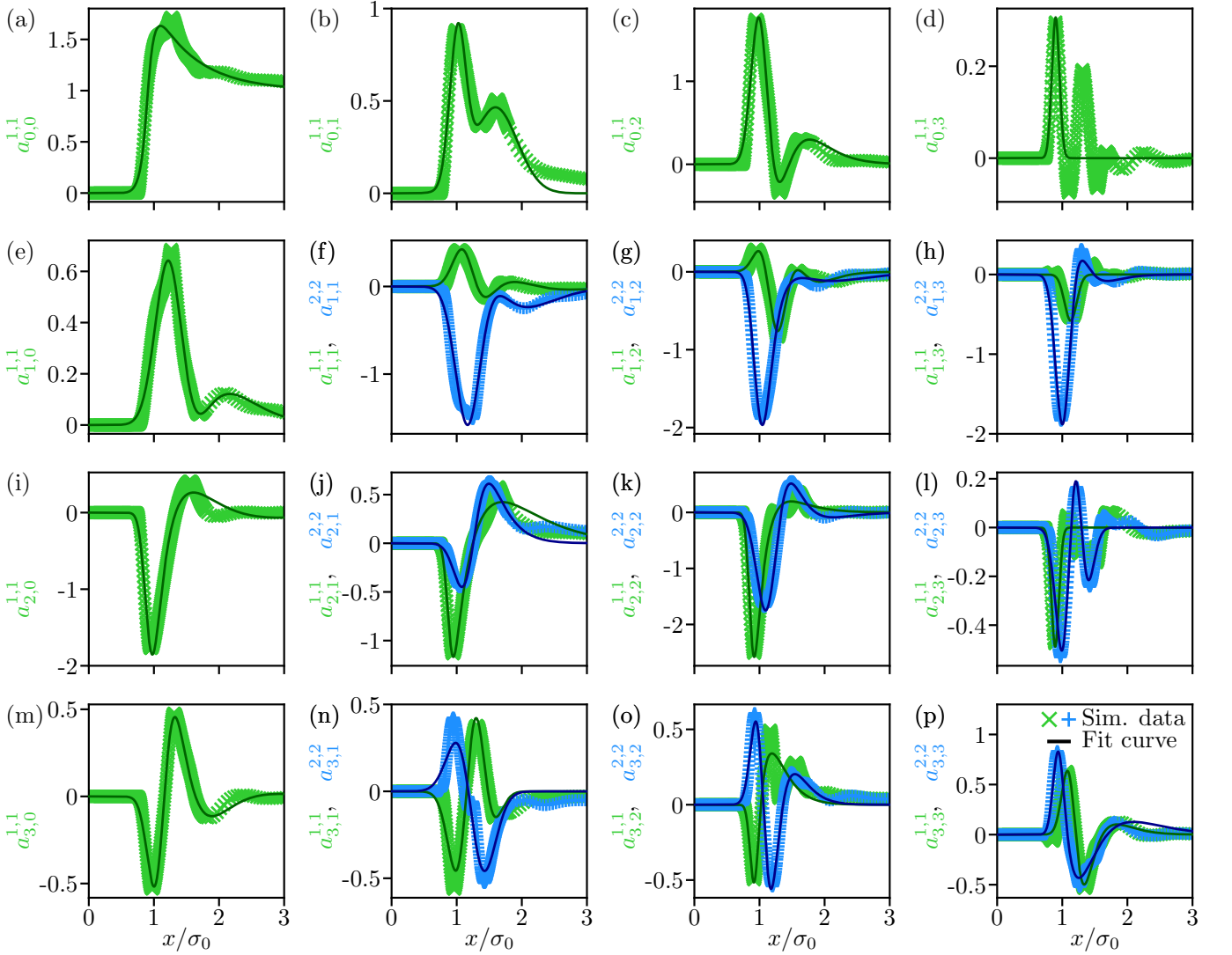


FIG. 6. Fourier coefficients $a_{h,j}^{k,k}$ of g for the simulation data (symbols) and the corresponding fitting results (solid lines) with the fit functions specified in Table I. The coefficients $a_{h,j}^{1,1}$ correspond to green crosses and the coefficients $a_{h,j}^{2,2}$ to blue plus symbols. The row and column correspond to the h and j index, respectively.

of system parameters. As a last step, each fit parameter is interpolated between the values of Pe and Φ_0 for which the fitting was performed.

Therefore, we need to ensure that the parameters of the former fitting functions are changing sufficiently smoothly regarding Pe and Φ_0 . Choosing suitable fitting functions is a crucial step for this. However, as some of the functions feature a lot of fitting parameters and are pretty complex, the fitting procedure improves when providing suitable starting parameters. This is accomplished by setting the starting parameters either to expected values or values resulting from the fitting procedure for comparable Péclet numbers or packing densities.

The interpolation is performed by using the function

$$h(Pe, \Phi_0) = \sum_{m=-2}^2 \sum_{n=0}^3 Pe^{\frac{m}{2}} \Phi_0^n u_{m,n}, \quad (29)$$

with the fit parameters $u_{m,n}$, which is employed for every fit parameter of every Fourier coefficient. This is again an empirical ansatz. Note that negative exponents of Pe correspond to positive exponents regarding the dependence on the temperature T as $Pe \propto 1/T$. Also, the course of some of the fit parameters is less complex than what Eq. (29) is capable of reproducing, but for simplicity, we choose one function for all parameters. The resulting values for $u_{m,n}$ for each fit parameter are shown in Tables II-XIV. With this interpolation, we obtain a fully analytical approximation g_{approx} of the pair-distribution function $g(Pe, \Phi_0; r, \phi_1, \phi_2)$.

To summarize: To reproduce $g_{\text{approx}}(Pe, \Phi_0; r, \phi_1, \phi_2)$ for specific values of Pe and Φ_0 , the first step is to calculate each fit parameter using the function $h(Pe, \Phi_0)$ in Eq. (29) and the parameters given in Tables II-XIV (see Appendix C). The resulting parameters are then em-

ployed in the functions in Table I to create the Fourier coefficients $a_{h,j}^{k,k}$. These Fourier coefficients can be put into Eq. (24) which gives $g_{\text{approx}}(\text{Pe}, \Phi_0; r, \phi_1, \phi_2)$. To determine the quality of the analytical approximation g_{approx} for all considered values of Pe and Φ_0 , we calculate the mean absolute error $\langle g - g_{\text{approx}} \rangle_{r < 3\sigma_0}$ via

$$\langle g - g_{\text{approx}} \rangle_{r < 3\sigma_0} = \frac{\int_0^{3\sigma_0} dr \int_0^{2\pi} d\phi_1 \int_0^{2\pi} d\phi_2 |g - g_{\text{approx}}|}{\int_0^{3\sigma_0} dr \int_0^{2\pi} d\phi_1 \int_0^{2\pi} d\phi_2 1}. \quad (30)$$

We integrate both angles ϕ_1 and ϕ_2 over the full range $[0, 2\pi[$ and integrate the distance r from 0 to $3\sigma_0$. The upper limit $3\sigma_0$ for the distance r is chosen according to the typical course of g . The angular dependence weakens for large r , which is shown in Figs. 4 and 5 as well as in the corresponding Fourier coefficients in Fig. 6. Thus, g is harder to reproduce for small values of r and easier to reproduce for large values of r . We are interested in the errors for the hard-to-reproduce range, so we chose $r < 3\sigma_0$. As the absolute error can be hard to interpret, we calculate the mean values $\langle g \rangle_{r < 3\sigma_0}$ via

$$\langle g \rangle_{r < 3\sigma_0} = \frac{\int_0^{3\sigma_0} dr \int_0^{2\pi} d\phi_1 \int_0^{2\pi} d\phi_2 g}{\int_0^{3\sigma_0} dr \int_0^{2\pi} d\phi_1 \int_0^{2\pi} d\phi_2 1}, \quad (31)$$

allowing us to calculate the relative error $\langle g - g_{\text{approx}} \rangle_{r < 3\sigma_0} / \langle g \rangle_{r < 3\sigma_0}$. The results are shown in Fig. 7. In Fig. 7(a), the mean values of g , $\langle g \rangle_{r < 3\sigma_0}$, are shown. The values slowly increase with an increase of the Péclet number and are mostly unaffected by changes in density. As g is a “probability modification”, the average values of g can be interpreted as the modification of the probability of finding a second particle in the proximity of the reference particle. If particles tend to aggregate, the average value of g increases. The absolute error $\langle g - g_{\text{approx}} \rangle_{r < 3\sigma_0}$ is shown in Fig. 7(b). Compared to the average value of g , it heavily depends on the Péclet number and grows strongly. The absolute error slightly increases with increasing packing density. Figure 7(c) shows the relative error $\langle g - g_{\text{approx}} \rangle_{r < 3\sigma_0} / \langle g \rangle_{r < 3\sigma_0}$ of the approximation. It varies between 10% and 56% and is especially high for high Péclet numbers, which correspond to low temperatures.

Generally, when reproducing the angular dependence of g with Fourier modes, sharp peaks of g are harder to reproduce. If the temperature in the system is very high, the particles’ interactions become more randomized, and sharp peaks of g are more “washed out”. This explains the improved approximation results for low Péclet numbers corresponding to high temperatures. Similar dependencies of the average value, absolute error, and relative error on the system parameters are found in the case of spherical particles [28, 44].

IV. CONCLUSION

In this article, we have studied the collective dynamics of active Brownian ellipsoids via computer simulations and obtained their state diagram. Depending on the Péclet number and the packing density, the system exhibits cluster formation, local polar order, polar flocks, and disordered phases. In addition, we have provided a detailed discussion of the pair-distribution function of active ellipsoids and obtained an analytical representation of this pair-distribution function.

Given that pair-distribution functions obtained in previous work [28, 44] have been used as an input in field-theoretical models for active spheres [34, 35], a natural continuation of the present work would be the development of a field theory for active ellipsoids based on the pair-distribution function obtained here. Moreover, one could investigate the state diagram of active ellipsoids in three spatial dimensions in order to analyze the effects of dimensionality, which are likely to be more pronounced than for spheres.

SUPPLEMENTARY MATERIAL

The Supplementary Material [78] contains a spreadsheet with the values of the fit coefficients (as shown in Appendix C) that are needed to recreate the analytical representation of the pair-distribution function, a Python script `abp_ellipsoidal2d.pairdistribution` that recreates the approximation of the pair-distribution function g using the values of the fit coefficients, and the Python scripts and raw data needed to recreate Figs. 1–8.

ACKNOWLEDGMENTS

We thank Jens Bickmann, Julian Jeggle, and Fenna Stegemerten for helpful discussions. R.W. is funded by the Deutsche Forschungsgemeinschaft (DFG, German Research Foundation) – 283183152 (WI 4170/3). The simulations for this work were performed on the computer cluster PALMA II of the University of Münster.

Appendix A: Particle interactions

We focus on hard particles and therefore use a short-ranged and purely repulsive interaction potential. More specifically, we use a modified version u_{int} of the Gay-Berne (GB) potential u_{GB} [79]. The GB potential describes the interaction of ellipsoids, which depends on the relative position $\mathbf{r}_{ij} = \mathbf{r}_j - \mathbf{r}_i$ of the interacting particles i and j as well as on their respective orientations $\hat{\mathbf{u}}_i$ and $\hat{\mathbf{u}}_j$. It is repulsive for short distances and attractive for larger ones. Thus, we disregard the attractive part, such that the potential is purely repulsive. This can be done by “cutting” off the interaction potential at

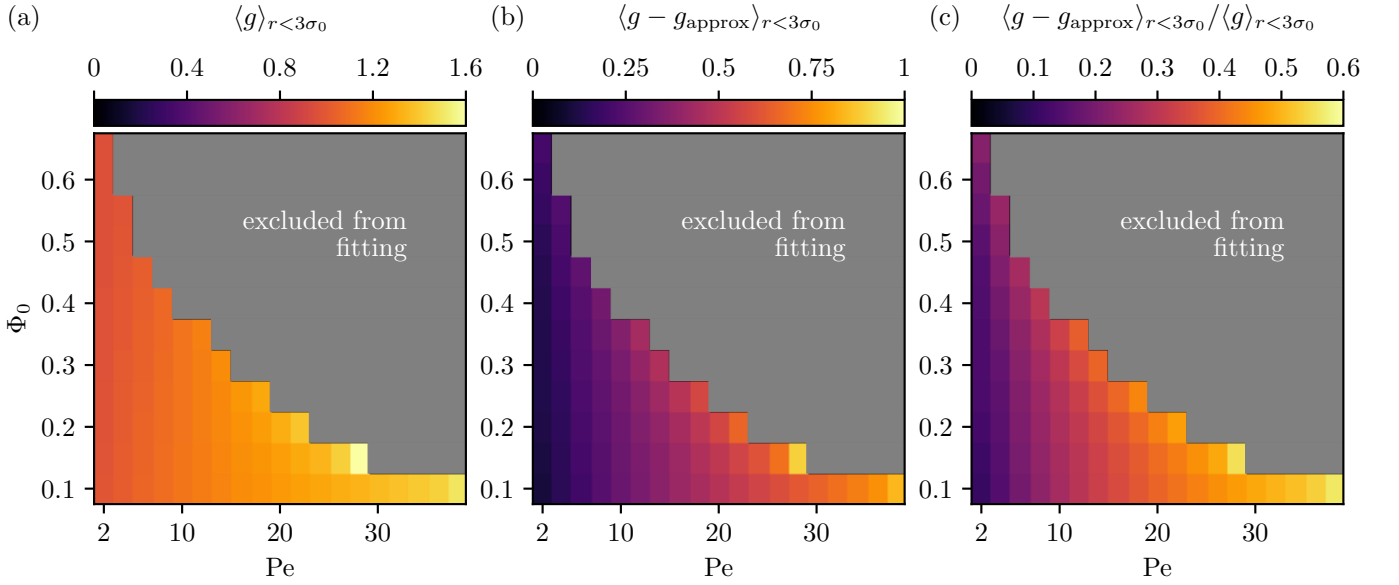


FIG. 7. (a) Mean value $\langle g \rangle_{r < 3\sigma_0}$ of g . (b) Absolute error, i.e., difference $\langle g - g_{\text{approx}} \rangle_{r < 3\sigma_0}$ between the approximation g_{approx} and g . (c) Mean relative error $\langle g - g_{\text{approx}} \rangle_{r < 3\sigma_0} / \langle g \rangle_{r < 3\sigma_0}$. All results shown here are calculated in the range $0 < r < 3\sigma_0$.

the minimum. In addition, we shift the potential to ensure that it is continuous and continuously differentiable (as done in Ref. [16]). The GB potential reads [79]

$$\begin{aligned}
 u_{\text{GB}}(\mathbf{r}_{ij}, \hat{\mathbf{u}}_i, \hat{\mathbf{u}}_j) &= 4\epsilon(\epsilon'_{\text{GB}}(\hat{\mathbf{u}}_i, \hat{\mathbf{u}}_j))^\nu (\epsilon^*_{\text{GB}}(\hat{\mathbf{r}}_{ij}, \hat{\mathbf{u}}_i, \hat{\mathbf{u}}_j))^\mu \\
 &\left[\left(\frac{1}{r_{ij}/\sigma_0 - \sigma_{\text{GB},ij} + 1} \right)^{12} - \left(\frac{1}{r_{ij}/\sigma_0 - \sigma_{\text{GB},ij} + 1} \right)^6 \right]
 \end{aligned} \quad (\text{A1})$$

with the energy ϵ and the dimensionless energy parameters ϵ'_{GB} and ϵ^*_{GB} of the potential, the exponents ν and μ , the distance between the centers of the two particles $r_{ij} = \|\mathbf{r}_{ij}\|$, the length scale σ_0 , and the distance of closest approach of the two particles $\sigma_{\text{GB},ij}$. Here, the energy parameter ϵ sets the energy of the potential. The strength parameter ϵ'_{GB} results from the derivation of the overlap of two ellipsoids known as the ‘‘Gaussian overlap potential’’ [80] and reads

$$\epsilon'_{\text{GB}}(\hat{\mathbf{u}}_i, \hat{\mathbf{u}}_j) = (1 - \chi^2(\hat{\mathbf{u}}_i \cdot \hat{\mathbf{u}}_j)^2)^{-\frac{1}{2}}, \quad (\text{A2})$$

where χ is the anisotropy parameter

$$\chi = \frac{\kappa^2 - 1}{\kappa^2 + 1}. \quad (\text{A3})$$

In the case of our ellipsoids, it is given by $\kappa = 2$. (For spheres, κ equals one.) The exponent ν modifies the potential, while the other energy parameter ϵ^*_{GB} allows to modify the interaction of the ellipsoids when two ellipsoids get close side-to-side versus end-to-end. Typically, the interaction is stronger when particles interact side-to-side, i.e., with their long sides close to each other, compared to particles interacting end-to-end, i.e., with their shortest sides close to each other.

This can be adjusted by the orientation-dependent energy parameter ϵ^*_{GB} , which was proposed by Gay and Berne [79] and reads

$$\begin{aligned}
 \epsilon^*_{\text{GB}}(\hat{\mathbf{r}}_{ij}, \hat{\mathbf{u}}_i, \hat{\mathbf{u}}_j) &= 1 - \frac{\chi'}{2} \left[\frac{(\hat{\mathbf{r}}_{ij} \cdot \hat{\mathbf{u}}_i + \hat{\mathbf{r}}_{ij} \cdot \hat{\mathbf{u}}_j)^2}{1 + \chi'(\hat{\mathbf{u}}_i \cdot \hat{\mathbf{u}}_j)} + \frac{(\hat{\mathbf{r}}_{ij} \cdot \hat{\mathbf{u}}_i - \hat{\mathbf{r}}_{ij} \cdot \hat{\mathbf{u}}_j)^2}{1 - \chi'(\hat{\mathbf{u}}_i \cdot \hat{\mathbf{u}}_j)} \right]
 \end{aligned} \quad (\text{A4})$$

with $\hat{\mathbf{r}}_{ij} = \mathbf{r}_{ij}/\|\mathbf{r}_{ij}\|$. From the desired interaction strength for the side-to-side interaction ϵ_{side} and the desired interaction strength for the end-to-end interaction ϵ_{end} , we obtain for the new parameter χ' the expression

$$\chi' = \frac{\frac{1}{\epsilon_{\text{side}}^\mu} - \frac{1}{\epsilon_{\text{end}}^\mu}}{\frac{1}{\epsilon_{\text{side}}^\mu} + \frac{1}{\epsilon_{\text{end}}^\mu}} \quad (\text{A5})$$

that depends only on the relative strength $\epsilon_{\text{side}}/\epsilon_{\text{end}}$. The exponents ν and μ as well as the energy ratio $\epsilon_{\text{side}}/\epsilon_{\text{end}}$ can be chosen depending on the situation. Simulations of different particle shapes require different parameter combinations [79, 81, 82]. In this work, we set $\epsilon_{\text{side}}/\epsilon_{\text{end}} = 1$, $\nu = 1$, and $\mu = 0$, so that our interaction potential is a Gaussian overlap potential.

The distance of closest approach $\sigma_{\text{GB},ij}$ can be calculated via

$$\begin{aligned}
 \sigma_{\text{GB},ij}(\hat{\mathbf{r}}_{ij}, \hat{\mathbf{u}}_i, \hat{\mathbf{u}}_j) &= \left(1 - \frac{\chi}{2} \left[\frac{(\hat{\mathbf{r}}_{ij} \cdot \hat{\mathbf{u}}_i + \hat{\mathbf{r}}_{ij} \cdot \hat{\mathbf{u}}_j)^2}{1 + \chi(\hat{\mathbf{u}}_i \cdot \hat{\mathbf{u}}_j)} \right. \right. \\
 &\quad \left. \left. + \frac{(\hat{\mathbf{r}}_{ij} \cdot \hat{\mathbf{u}}_i - \hat{\mathbf{r}}_{ij} \cdot \hat{\mathbf{u}}_j)^2}{1 - \chi(\hat{\mathbf{u}}_i \cdot \hat{\mathbf{u}}_j)} \right] \right)^{-\frac{1}{2}}.
 \end{aligned} \quad (\text{A6})$$

Note that $\sigma_{\text{GB},ij}$ is not the exact distance of two ellipsoids, but a very common approximation. The exact way

to calculate the distance between ellipsoids in two dimensions has only been discovered rather recently [83], but it is computationally too expensive to be applicable in a large-scale computer simulation. As stated at the beginning of this section, our potential is a purely repulsive and short-ranged modification of the GB potential. This is achieved by cutting off the interaction at the minimum of the potential and shifting the potential. Following Refs. [16, 51], this yields

$$u_{\text{int}}(\mathbf{r}_{ij}, \hat{\mathbf{u}}_i, \hat{\mathbf{u}}_j) = \begin{cases} u_{\text{GB}}(\mathbf{r}_{ij}, \hat{\mathbf{u}}_i, \hat{\mathbf{u}}_j) + \epsilon_{\text{min}}, & \text{if } r_{ij} \leq r_c, \\ 0, & \text{else} \end{cases} \quad (\text{A7})$$

with $\epsilon_{\text{min}} = \epsilon \epsilon'_{\text{GB}}{}^\nu \epsilon_{\text{GB}}^{\star\mu}$ and $r_c = \sigma_0(2^{1/6} - 1) + \sigma_{\text{GB},ij}$. The translational force resulting from the interaction is given by

$$\mathbf{F}_{\text{int},i}(\{\mathbf{r}_j, \hat{\mathbf{u}}_j\}) = -\nabla_{\mathbf{r}_i} \sum_{j \neq i} u_{\text{int}}(\mathbf{r}_{ij}, \hat{\mathbf{u}}_i, \hat{\mathbf{u}}_j) \quad (\text{A8})$$

and the torque is

$$M_{\text{int},i}(\{\mathbf{r}_j, \hat{\mathbf{u}}_j\}) = -\frac{\partial}{\partial \varphi_i} \sum_{j \neq i} u_{\text{int}}(\mathbf{r}_{ij}, \hat{\mathbf{u}}_i, \hat{\mathbf{u}}_j). \quad (\text{A9})$$

Appendix B: Calculation of polarization and nematic order

We use the local polarization in the system as an order parameter. The polarization at an arbitrary position \mathbf{r} is calculated with the orientations of all nearby particles. Each particle's orientation vector contributes to the polarization vector of that reference point, multiplied by a factor that depends on the distance between the particle and the reference point. Therefore, the resulting polarization $\mathbf{P}(\mathbf{r})$ at a position \mathbf{r} reads

$$\mathbf{P}(\mathbf{r}) = \sum_{i=0}^N \hat{\mathbf{u}}_i f_d(\mathbf{r}, \mathbf{r}_i, \hat{\mathbf{u}}_i), \quad (\text{B1})$$

where N is the number of particles in the system, \mathbf{r}_i is the position of the i -th particle, $\hat{\mathbf{u}}_i$ is the orientation of the i -th particle, and f_d is the distance-dependent scaling factor. This factor ensures that only particles in the vicinity of \mathbf{r} contribute to the polarization measured at this point. This is because the particles' influence on the polarization decreases with a higher distance between the particle and the point of interest.

Since the scaling factor f_d depends on the distance of a particle to the reference point, we need a way to measure this distance. For spheres, we can use the distance from the reference point to the particle's center. However, in the case of ellipsoids the simple distance to the center of the ellipsoid should not be used as the particles are not spherical. Instead, considering the elliptic shape of the particles, prolate ellipsoidal coordinates are an excellent

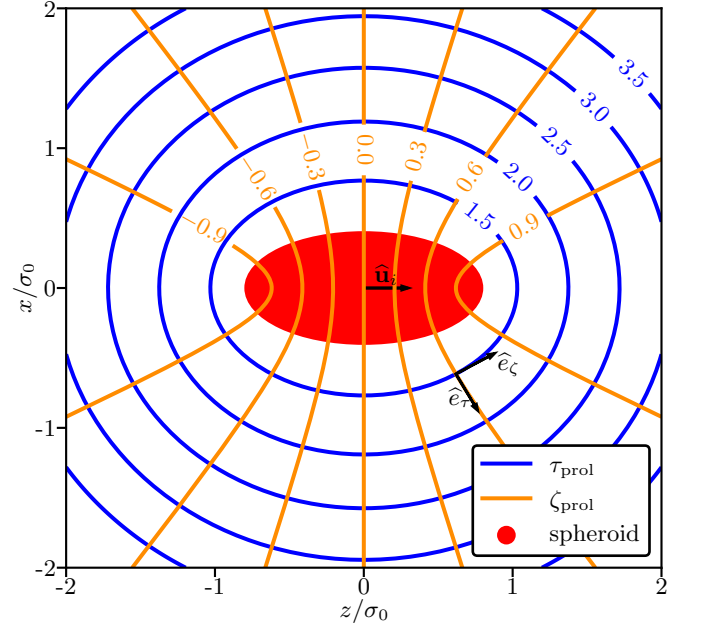


FIG. 8. Scheme showing the curves representing prolate spheroidal coordinates for constant values of τ_{prol} (blue) and ζ_{prol} (orange) in the $z-x$ -plane. The azimuthal angular parameter φ_{prol} induces rotation around the z -axis.

way to factor in their form. The prolate spheroidal coordinate system is set up as follows: The center of the particle is the center of a new prolate spheroidal coordinate system, and the particle's orientation defines its z -axis. Three values define the new prolate spheroidal coordinate system: the distance parameter $\tau_{\text{prol}} \geq 1$, the polar angular parameter $\zeta_{\text{prol}} \in [-1, 1]$, and the azimuthal angular parameter $\varphi_{\text{prol}} \in [0, 2\pi[$. The azimuthal angular parameter can be dismissed as the ellipsoids only move in the two-dimensional plane here.

The values of the parameters can be calculated via

$$\tau_{\text{prol}} = \frac{1}{2d_{\text{foc}}} \left(\sqrt{x'^2 + y'^2 + (z' + d_{\text{foc}})^2} + \sqrt{x'^2 + y'^2 + (z' - d_{\text{foc}})^2} \right), \quad (\text{B2})$$

$$\zeta_{\text{prol}} = \frac{1}{2d_{\text{foc}}} \left(\sqrt{x'^2 + y'^2 + (z' + d_{\text{foc}})^2} - \sqrt{x'^2 + y'^2 + (z' - d_{\text{foc}})^2} \right), \quad (\text{B3})$$

$$\varphi_{\text{prol}} = \arctan\left(\frac{y'}{x'}\right), \quad (\text{B4})$$

where x' , y' , and z' are the Cartesian coordinates of the reference point in the new reference frame and $2d_{\text{foc}} = \sqrt{(a_{\text{el}}/2)^2 - (b_{\text{el}}/2)^2}$ is the distance between the center of the ellipsoid and its focal point. A scheme of the prolate coordinate system is shown in Fig. 8. Varying the polar angular parameter ζ_{prol} while keeping the distance parameter τ_{prol} constant allows to draw prolate ellipsoids. The distance parameter τ_{prol} is a good measurement for

the distance from the ellipsoid. We can now transfer the reference point into the new coordinate system, and the resulting value of τ_{prol} is the distance. Note that the value of τ_{prol} is greater or equal to one. Thus, we employ $\tau_{\text{prol}} - 1$ as the value for the distance from the center of the ellipsoid. The scaling function is then defined as

$$f_d(\tau_{\text{prol}}) = \begin{cases} \bar{f}_d \exp\left(\frac{-1}{1 - ((\tau_{\text{prol}} - 1)/r_c)^2}\right), & \text{if } \tau_{\text{prol}} < r_c, \\ 0, & \text{else,} \end{cases} \quad (\text{B5})$$

where r_c is the cut-off distance up to which a particle influences the polarization and \bar{f}_d is a normalization parameter. We found a good agreement between the visual inspection of the states and the polarization for $r_c = 5\sigma_0 + a_{\text{el}}/(2d_{\text{foc}})$ for ellipsoids. The normalization parameter \bar{f}_d fixes the volume. Additionally, this parameter can be used to smear out the particles to determine a locally blurred density. If the density were to be calculated, we would choose \bar{f}_d in such a way that we get the correct overall density, which means

$$\int_{A_{\text{part}}} dA H_{\text{part}} = \int_{A_{\text{part}}} dA f_d(\tau_{\text{prol}}) \quad (\text{B6})$$

where A_{part} is the area of the particle and H_{part} is a function that is one inside the particle and zero elsewhere. Equation (B6) defines \bar{f}_d . The function f_d is similar to a Gaussian distribution, but falls off to zero at a finite distance $\tau_{\text{prol}} = r_c$ while staying continuously differentiable. Thus, the closer a particle is to the reference point, the stronger the orientation of the particle influences the polarization at the reference point. By spreading a fine grid over the entire simulation domain and calculating the polarization for every grid point, we can calculate the average local polarization divided by density

$$\frac{\langle\langle \mathbf{P} \rangle\rangle}{\Phi_0} = \frac{1}{N_{\text{grid}}\Phi_0} \sum_{\mathbf{r}_i \in R_{\text{grid}}} \|\mathbf{P}(\mathbf{r}_i)\|, \quad (\text{B7})$$

where R_{grid} denotes the set of all grid points and N_{grid} denotes the number of all grid points. We chose a distance of $0.1\sigma_0$ between two grid points. For each grid point, the length of the polarization vector is calculated. Then, we average over the resulting values. Applying

this method, we measure the average local polarization $\langle\langle \mathbf{P} \rangle\rangle/\Phi_0$ for a single time and the whole simulation domain. Additionally, we can average over 300 time steps to get a reliable measurement of the typical polarization for a given parameter set. Thereby, the values of the polarization obtained for different system parameters (Péclet number and packing density) can be compared. Thus, the average local polarization we use to characterize a system is averaged over the simulation domain and over time. We can calculate the average global polarization

$$\frac{\|\langle \mathbf{P} \rangle\|}{\Phi_0} = \frac{1}{N_{\text{grid}}\Phi_0} \left\| \sum_{\mathbf{r}_i \in R_{\text{grid}}} \mathbf{P}(\mathbf{r}_i) \right\| \quad (\text{B8})$$

of a system by averaging over the local polarization vector grid (a square lattice), calculating the norm of the resulting vector, and dividing by Φ_0 . By averaging over the local polarization vectors instead of their norm, we can measure whether the whole system is polarized.

In addition to the polarization, the average nematic order divided by density $\langle S \rangle/\Phi_0$ can be used as an order parameter. It is calculated via the nematic tensor \underline{Q} , which is given by [48]

$$\underline{Q}(\mathbf{r}) = \sum_{i=0}^N (\hat{\mathbf{u}}_i f_d(\mathbf{r}, \mathbf{r}_i, \hat{\mathbf{u}}_i) \otimes \hat{\mathbf{u}}_i f_d(\mathbf{r}, \mathbf{r}_i, \hat{\mathbf{u}}_i)) - \frac{1}{2}. \quad (\text{B9})$$

From the nematic tensor \underline{Q} , we can calculate the nematic order S using

$$S^2(\mathbf{r}) = 2\text{Tr}(\underline{Q}^2(\mathbf{r})) \quad (\text{B10})$$

with the trace Tr . This is done for every point of a fine grid over the entire simulation domain. Then, we average over these points and time. As a last step, the result is divided by density. This gives the average nematic order divided by density, which is defined as

$$\frac{\langle S \rangle}{\Phi_0} = \frac{1}{N_{\text{grid}}\Phi_0} \sum_{\mathbf{r}_i \in R_{\text{grid}}} \sqrt{S^2(\mathbf{r}_i)}. \quad (\text{B11})$$

Appendix C: Tables of fit parameters

These tables contain the fit parameters required for the function $h(\text{Pe}, \Phi_0)$ defined in Eq. (29).

[1] M. C. Marchetti, J.-F. Joanny, S. Ramaswamy, T. B. Liverpool, J. Prost, M. Rao, and R. A. Simha, Hydrodynamics of soft active matter, *Reviews of Modern Physics* **85**, 1143 (2013).
 [2] C. Bechinger, R. Di Leonardo, H. Löwen, C. Reichardt, G. Volpe, and G. Volpe, Active particles in complex and crowded environments, *Reviews of Modern Physics* **88**, 045006 (2016).

[3] M. E. Cates and J. Tailleur, Motility-induced phase separation, *Annual Review of Condensed Matter Physics* **6**, 219 (2015).
 [4] T. Vicsek, A. Czirók, E. Ben-Jacob, I. Cohen, and O. Shochet, Novel type of phase transition in a system of self-driven particles, *Physical Review Letters* **75**, 1226 (1995).
 [5] J. Toner and Y. Tu, Long-range order in a two-dimensional dynamical XY model: how birds fly to-

	$u_{-2,0}$ $u_{-1,3}$ $u_{1,2}$	$u_{-2,1}$ $u_{0,0}$ $u_{1,3}$	$u_{-2,2}$ $u_{0,1}$ $u_{2,0}$	$u_{-2,3}$ $u_{0,2}$ $u_{2,1}$	$u_{-1,0}$ $u_{0,3}$ $u_{2,2}$	$u_{-1,1}$ $u_{1,0}$ $u_{2,3}$	$u_{-1,2}$ $u_{1,1}$	
$a_{0,0}^{1,1}$	a	$-2.737 \cdot 10^1$	$4.643 \cdot 10^1$	$-2.684 \cdot 10^1$	$6.357 \cdot 10^0$	$-4.461 \cdot 10^{-1}$	$3.556 \cdot 10^2$	$-5.713 \cdot 10^2$
		$3.050 \cdot 10^2$	$-6.047 \cdot 10^1$	$3.073 \cdot 10^0$	$-5.688 \cdot 10^2$	$6.566 \cdot 10^2$	$-9.030 \cdot 10^1$	$-9.534 \cdot 10^1$
		$2.378 \cdot 10^1$	$-1.762 \cdot 10^2$	$7.852 \cdot 10^2$	$-9.153 \cdot 10^2$	$3.911 \cdot 10^2$	$-5.398 \cdot 10^1$	
	μ	$5.836 \cdot 10^0$	$-8.995 \cdot 10^0$	$6.051 \cdot 10^0$	$-1.168 \cdot 10^0$	$8.930 \cdot 10^{-2}$	$-1.227 \cdot 10^2$	$1.814 \cdot 10^2$
		$-9.056 \cdot 10^1$	$1.813 \cdot 10^1$	$-1.245 \cdot 10^0$	$3.358 \cdot 10^2$	$-4.523 \cdot 10^2$	$1.962 \cdot 10^2$	$-3.184 \cdot 10^1$
		$1.484 \cdot 10^0$	$-2.291 \cdot 10^2$	$2.716 \cdot 10^2$	$-9.364 \cdot 10^1$	$8.809 \cdot 10^0$	$1.664 \cdot 10^{-1}$	
	ς	$-3.981 \cdot 10^0$	$4.485 \cdot 10^0$	$-6.754 \cdot 10^{-1}$	$-3.059 \cdot 10^{-1}$	$5.984 \cdot 10^{-2}$	$-1.816 \cdot 10^1$	$5.593 \cdot 10^1$
		$-5.315 \cdot 10^1$	$1.909 \cdot 10^1$	$-2.068 \cdot 10^0$	$5.904 \cdot 10^2$	$-1.098 \cdot 10^3$	$7.276 \cdot 10^2$	$-1.996 \cdot 10^2$
		$1.801 \cdot 10^1$	$-1.124 \cdot 10^3$	$1.942 \cdot 10^3$	$-1.165 \cdot 10^3$	$2.787 \cdot 10^2$	$-2.018 \cdot 10^1$	
	λ	$3.091 \cdot 10^2$	$-4.979 \cdot 10^2$	$2.802 \cdot 10^2$	$-6.325 \cdot 10^1$	$4.972 \cdot 10^0$	$-5.778 \cdot 10^3$	$8.925 \cdot 10^3$
		$-4.687 \cdot 10^3$	$1.002 \cdot 10^3$	$-7.428 \cdot 10^1$	$1.947 \cdot 10^4$	$-2.878 \cdot 10^4$	$1.433 \cdot 10^4$	$-2.851 \cdot 10^3$
		$1.889 \cdot 10^2$	$-1.729 \cdot 10^4$	$2.438 \cdot 10^4$	$-1.131 \cdot 10^4$	$1.988 \cdot 10^3$	$-1.012 \cdot 10^2$	
	l_1	$5.689 \cdot 10^2$	$-1.033 \cdot 10^3$	$6.665 \cdot 10^2$	$-1.773 \cdot 10^2$	$1.636 \cdot 10^1$	$-7.842 \cdot 10^3$	$1.463 \cdot 10^4$
		$-9.605 \cdot 10^3$	$2.587 \cdot 10^3$	$-2.267 \cdot 10^2$	$5.388 \cdot 10^4$	$-9.512 \cdot 10^4$	$5.845 \cdot 10^4$	$-1.450 \cdot 10^4$
		$1.137 \cdot 10^3$	$-6.368 \cdot 10^4$	$1.029 \cdot 10^5$	$-5.451 \cdot 10^4$	$1.005 \cdot 10^4$	$-2.359 \cdot 10^2$	
$a_{0,1}^{1,1}$	a_1	$-6.027 \cdot 10^0$	$1.062 \cdot 10^1$	$-7.124 \cdot 10^0$	$2.003 \cdot 10^0$	$-1.654 \cdot 10^{-1}$	$7.910 \cdot 10^1$	$-1.370 \cdot 10^2$
		$8.474 \cdot 10^1$	$-2.192 \cdot 10^1$	$1.925 \cdot 10^0$	$-2.116 \cdot 10^2$	$3.624 \cdot 10^2$	$-2.191 \cdot 10^2$	$5.505 \cdot 10^1$
		$-4.596 \cdot 10^0$	$2.014 \cdot 10^2$	$-3.535 \cdot 10^2$	$2.214 \cdot 10^2$	$-5.865 \cdot 10^1$	$5.438 \cdot 10^0$	
	μ_1	$-1.175 \cdot 10^1$	$1.348 \cdot 10^1$	$-4.238 \cdot 10^0$	$8.306 \cdot 10^{-1}$	$-4.455 \cdot 10^{-2}$	$1.277 \cdot 10^2$	$-1.410 \cdot 10^2$
		$5.143 \cdot 10^1$	$-6.925 \cdot 10^0$	$2.459 \cdot 10^{-1}$	$-2.190 \cdot 10^2$	$1.650 \cdot 10^2$	$-8.199 \cdot 10^0$	$-1.416 \cdot 10^1$
		$2.119 \cdot 10^0$	$5.645 \cdot 10^1$	$5.708 \cdot 10^1$	$-9.675 \cdot 10^1$	$3.289 \cdot 10^1$	$-2.946 \cdot 10^0$	
	ς_1	$-5.054 \cdot 10^0$	$7.380 \cdot 10^0$	$-3.645 \cdot 10^0$	$7.931 \cdot 10^{-1}$	$-5.812 \cdot 10^{-2}$	$1.070 \cdot 10^2$	$-1.472 \cdot 10^2$
		$7.000 \cdot 10^1$	$-1.343 \cdot 10^1$	$8.615 \cdot 10^{-1}$	$-2.645 \cdot 10^2$	$3.200 \cdot 10^2$	$-1.198 \cdot 10^2$	$1.338 \cdot 10^1$
		$1.421 \cdot 10^{-1}$	$1.402 \cdot 10^2$	$-1.150 \cdot 10^2$	$-1.404 \cdot 10^{-1}$	$1.534 \cdot 10^1$	$-2.416 \cdot 10^0$	
	a_2	$-9.846 \cdot 10^0$	$2.092 \cdot 10^1$	$-1.572 \cdot 10^1$	$4.858 \cdot 10^0$	$-4.887 \cdot 10^{-1}$	$1.972 \cdot 10^2$	$-3.769 \cdot 10^2$
		$2.592 \cdot 10^2$	$-7.562 \cdot 10^1$	$7.836 \cdot 10^0$	$-8.291 \cdot 10^2$	$1.535 \cdot 10^3$	$-1.016 \cdot 10^3$	$2.833 \cdot 10^2$
		$-2.758 \cdot 10^1$	$1.028 \cdot 10^3$	$-1.885 \cdot 10^3$	$1.234 \cdot 10^3$	$-3.404 \cdot 10^2$	$3.321 \cdot 10^1$	
	μ_2	$-2.309 \cdot 10^0$	$4.503 \cdot 10^0$	$-1.230 \cdot 10^0$	$8.442 \cdot 10^{-1}$	$-1.001 \cdot 10^{-1}$	$5.819 \cdot 10^1$	$-1.111 \cdot 10^2$
		$7.443 \cdot 10^1$	$-2.103 \cdot 10^1$	$2.157 \cdot 10^0$	$-2.646 \cdot 10^2$	$4.851 \cdot 10^2$	$-3.120 \cdot 10^2$	$8.332 \cdot 10^1$
		$-8.092 \cdot 10^0$	$3.121 \cdot 10^2$	$-5.598 \cdot 10^2$	$3.522 \cdot 10^2$	$-9.265 \cdot 10^1$	$9.029 \cdot 10^0$	
ς_2	$9.550 \cdot 10^0$	$-1.158 \cdot 10^1$	$3.779 \cdot 10^0$	$-5.367 \cdot 10^{-5}$	$-6.380 \cdot 10^{-2}$	$6.245 \cdot 10^1$	$-1.306 \cdot 10^2$	
	$9.565 \cdot 10^1$	$-2.868 \cdot 10^1$	$2.889 \cdot 10^0$	$-4.235 \cdot 10^2$	$7.703 \cdot 10^2$	$-4.967 \cdot 10^2$	$1.330 \cdot 10^2$	
	$-1.206 \cdot 10^1$	$5.205 \cdot 10^2$	$-9.081 \cdot 10^2$	$5.543 \cdot 10^2$	$-1.373 \cdot 10^2$	$1.096 \cdot 10^1$		

TABLE II. Fit coefficients of the function $h(\text{Pe}, \Phi_0)$ used to fit the variables of the Fourier coefficients $a_{0,0}^{1,1}$ and $a_{0,1}^{1,1}$ of the function g_{approx} .

- gether, Physical Review Letters **75**, 4326 (1995).
- [6] J. Toner, Y. Tu, and S. Ramaswamy, Hydrodynamics and phases of flocks, Annals of Physics **318**, 170 (2005).
- [7] M. Paoluzzi, D. Levis, and I. Pagonabarraga, From motility-induced phase-separation to glassiness in dense active matter, Communications Physics **5**, 111 (2022).
- [8] A. K. Omar, H. Row, S. A. Mallory, and J. F. Brady, Mechanical theory of nonequilibrium coexistence and motility-induced phase separation, Proceedings of the National Academy of Sciences U.S.A. **120**, e2219900120 (2023).
- [9] C. Anderson and A. Fernandez-Nieves, Social interactions lead to motility-induced phase separation in fire ants, Nature Communications **13**, 6710 (2022).
- [10] K. L. Kreienkamp and S. H. L. Klapp, Clustering and flocking of repulsive chiral active particles with non-reciprocal couplings, New Journal of Physics **24**, 123009 (2022).
- [11] Q. Yu and Y. Tu, Energy cost for flocking of active spins: the cusped dissipation maximum at the flocking transition, Physical Review Letters **129**, 278001 (2022).
- [12] L. Caprini and H. Löwen, Flocking without alignment interactions in attractive active Brownian particles, Physical Review Letters **130**, 148202 (2023).
- [13] R. Großmann, I. S. Aranson, and F. Peruani, A particle-field approach bridges phase separation and collective motion in active matter, Nature Communications **11**, 5365 (2020).
- [14] P. Arora, A. K. Sood, and R. Ganapathy, Motile topological defects hinder dynamical arrest in dense liquids of active ellipsoids, Physical Review Letters **128**, 178002 (2022).
- [15] T. C. Rebocho, M. Tasinkevych, and C. S. Dias, Effect of anisotropy on the formation of active particle films, Physical Review E **106**, 024609 (2022).

	$u_{-2,0}$ $u_{-1,3}$ $u_{1,2}$	$u_{-2,1}$ $u_{0,0}$ $u_{1,3}$	$u_{-2,2}$ $u_{0,1}$ $u_{2,0}$	$u_{-2,3}$ $u_{0,2}$ $u_{2,1}$	$u_{-1,0}$ $u_{0,3}$ $u_{2,2}$	$u_{-1,1}$ $u_{1,0}$ $u_{2,3}$	$u_{-1,2}$ $u_{1,1}$	
$a_{0,2}^{1,1}$	α	$-1.136 \cdot 10^2$	$2.185 \cdot 10^2$	$-1.581 \cdot 10^2$	$5.366 \cdot 10^1$	$-5.567 \cdot 10^0$	$4.596 \cdot 10^3$	$-8.094 \cdot 10^3$
		$5.043 \cdot 10^3$	$-1.305 \cdot 10^3$	$1.153 \cdot 10^2$	$-1.891 \cdot 10^4$	$3.241 \cdot 10^4$	$-1.934 \cdot 10^4$	$4.679 \cdot 10^3$
		$-3.687 \cdot 10^2$	$1.839 \cdot 10^4$	$-3.013 \cdot 10^4$	$1.671 \cdot 10^4$	$-3.521 \cdot 10^3$	$2.000 \cdot 10^2$	
	μ	$-3.564 \cdot 10^0$	$4.365 \cdot 10^0$	$-2.577 \cdot 10^{-1}$	$4.620 \cdot 10^{-2}$	$1.163 \cdot 10^{-2}$	$2.935 \cdot 10^1$	$-3.633 \cdot 10^1$
		$1.144 \cdot 10^1$	$-8.634 \cdot 10^{-2}$	$-2.509 \cdot 10^{-1}$	$-8.349 \cdot 10^{-1}$	$-4.781 \cdot 10^1$	$6.640 \cdot 10^1$	$-2.784 \cdot 10^1$
		$3.581 \cdot 10^0$	$-1.229 \cdot 10^2$	$2.733 \cdot 10^2$	$-2.144 \cdot 10^2$	$6.966 \cdot 10^1$	$-7.870 \cdot 10^0$	
	ς	$-1.463 \cdot 10^0$	$2.233 \cdot 10^0$	$-9.562 \cdot 10^{-1}$	$2.161 \cdot 10^{-1}$	$-1.666 \cdot 10^{-2}$	$2.642 \cdot 10^1$	$-4.220 \cdot 10^1$
		$2.283 \cdot 10^1$	$-4.843 \cdot 10^0$	$3.211 \cdot 10^{-1}$	$-7.454 \cdot 10^1$	$1.115 \cdot 10^2$	$-5.306 \cdot 10^1$	$8.192 \cdot 10^0$
		$-7.048 \cdot 10^{-2}$	$3.147 \cdot 10^1$	$-2.511 \cdot 10^1$	$-1.027 \cdot 10^1$	$1.196 \cdot 10^1$	$-2.259 \cdot 10^0$	
	λ	$-7.847 \cdot 10^1$	$9.657 \cdot 10^1$	$-1.620 \cdot 10^1$	$-1.938 \cdot 10^0$	$5.428 \cdot 10^{-1}$	$-3.844 \cdot 10^1$	$3.320 \cdot 10^2$
		$-4.043 \cdot 10^2$	$1.428 \cdot 10^2$	$-1.535 \cdot 10^1$	$2.657 \cdot 10^3$	$-5.224 \cdot 10^3$	$3.598 \cdot 10^3$	$-9.952 \cdot 10^2$
		$9.411 \cdot 10^1$	$-4.301 \cdot 10^3$	$7.847 \cdot 10^3$	$-5.007 \cdot 10^3$	$1.304 \cdot 10^3$	$-1.171 \cdot 10^2$	
	l_1	$-8.763 \cdot 10^0$	$1.555 \cdot 10^1$	$-1.272 \cdot 10^1$	$2.705 \cdot 10^0$	$-2.543 \cdot 10^{-1}$	$1.462 \cdot 10^2$	$-2.588 \cdot 10^2$
		$1.625 \cdot 10^2$	$-4.294 \cdot 10^1$	$4.001 \cdot 10^0$	$-5.705 \cdot 10^2$	$1.001 \cdot 10^3$	$-6.205 \cdot 10^2$	$1.607 \cdot 10^2$
		$-1.445 \cdot 10^1$	$6.776 \cdot 10^2$	$-1.190 \cdot 10^3$	$7.389 \cdot 10^2$	$-1.918 \cdot 10^2$	$1.746 \cdot 10^1$	
	l_2	$7.763 \cdot 10^0$	$-1.404 \cdot 10^1$	$1.115 \cdot 10^1$	$-2.622 \cdot 10^0$	$2.581 \cdot 10^{-1}$	$-1.436 \cdot 10^2$	$2.570 \cdot 10^2$
		$-1.636 \cdot 10^2$	$4.409 \cdot 10^1$	$-4.216 \cdot 10^0$	$5.825 \cdot 10^2$	$-1.032 \cdot 10^3$	$6.480 \cdot 10^2$	$-1.709 \cdot 10^2$
		$1.575 \cdot 10^1$	$-7.153 \cdot 10^2$	$1.269 \cdot 10^3$	$-7.993 \cdot 10^2$	$2.117 \cdot 10^2$	$-1.980 \cdot 10^1$	
$a_{0,3}^{1,1}$	α	$1.125 \cdot 10^1$	$-2.058 \cdot 10^1$	$1.362 \cdot 10^1$	$-3.904 \cdot 10^0$	$4.121 \cdot 10^{-1}$	$-1.963 \cdot 10^2$	$3.465 \cdot 10^2$
		$-2.180 \cdot 10^2$	$5.839 \cdot 10^1$	$-5.663 \cdot 10^0$	$7.842 \cdot 10^2$	$-1.372 \cdot 10^3$	$8.530 \cdot 10^2$	$-2.253 \cdot 10^2$
		$2.156 \cdot 10^1$	$-8.485 \cdot 10^2$	$1.470 \cdot 10^3$	$-9.008 \cdot 10^2$	$2.330 \cdot 10^2$	$-2.156 \cdot 10^1$	
	μ	$2.967 \cdot 10^1$	$-3.890 \cdot 10^1$	$1.891 \cdot 10^1$	$-3.694 \cdot 10^0$	$3.002 \cdot 10^{-1}$	$-5.948 \cdot 10^2$	$8.071 \cdot 10^2$
		$-3.648 \cdot 10^2$	$6.976 \cdot 10^1$	$-5.111 \cdot 10^0$	$1.509 \cdot 10^3$	$-1.834 \cdot 10^3$	$6.865 \cdot 10^2$	$-1.059 \cdot 10^2$
		$7.400 \cdot 10^0$	$-9.701 \cdot 10^2$	$1.046 \cdot 10^3$	$-3.407 \cdot 10^2$	$6.794 \cdot 10^1$	$-1.028 \cdot 10^1$	
	ς	$-6.793 \cdot 10^0$	$8.681 \cdot 10^0$	$-3.137 \cdot 10^0$	$2.205 \cdot 10^{-1}$	$4.000 \cdot 10^{-2}$	$7.345 \cdot 10^1$	$-9.078 \cdot 10^1$
		$3.053 \cdot 10^1$	$-6.077 \cdot 10^{-1}$	$-6.928 \cdot 10^{-1}$	$-1.613 \cdot 10^2$	$1.466 \cdot 10^2$	$4.671 \cdot 10^0$	$-2.992 \cdot 10^1$
		$5.858 \cdot 10^0$	$2.300 \cdot 10^1$	$1.167 \cdot 10^2$	$-1.875 \cdot 10^2$	$8.505 \cdot 10^1$	$-1.190 \cdot 10^1$	

TABLE III. Fit coefficients of the function $h(\text{Pe}, \Phi_0)$ used to fit the variables of the Fourier coefficients $a_{0,2}^{1,1}$ and $a_{0,3}^{1,1}$ of the function g_{approx} .

- [16] A. Jayaram, A. Fischer, and T. Speck, From scalar to polar active matter: Connecting simulations with mean-field theory, *Physical Review E* **101**, 022602 (2020).
- [17] M. N. Van Der Linden, L. C. Alexander, D. G. A. L. Aarts, and O. Dauchot, Interrupted motility induced phase separation in aligning active colloids, *Physical Review Letters* **123**, 098001 (2019).
- [18] A. Suma, G. Gonnella, D. Marenduzzo, and E. Orlandini, Motility-induced phase separation in an active dumbbell fluid, *EPL* **108**, 56004 (2014).
- [19] G.-J. Liao, C. K. Hall, and S. H. L. Klapp, Dynamical self-assembly of dipolar active Brownian particles in two dimensions, *Soft Matter* **16**, 2208 (2020).
- [20] E. Sesé-Sansa, G.-J. Liao, D. Levis, I. Pagonabarraga, and S. H. L. Klapp, Impact of dipole-dipole interactions on motility-induced phase separation, *Soft Matter* **18**, 5388 (2022).
- [21] R. Van Damme, J. Rodenburg, R. van Roij, and M. Dijkstra, Interparticle torques suppress motility-induced phase separation for rodlike particles, *Journal of Chemical Physics* **150**, 164501 (2019).
- [22] M. Theers, E. Westphal, K. Qi, R. G. Winkler, and G. Gompper, Clustering of microswimmers: interplay of shape and hydrodynamics, *Soft Matter* **14**, 8590 (2018).
- [23] X.-q. Shi and H. Chaté, Self-propelled rods: Linking alignment-dominated and repulsion-dominated active matter, arXiv:1807.00294 (2018).
- [24] W.-T. L. Fan, O. S. Pak, and M. Sandoval, Ellipsoidal Brownian self-driven particles in a magnetic field, *Physical Review E* **95**, 032605 (2017).
- [25] M. Bär, R. Großmann, S. Heidenreich, and F. Peruani, Self-propelled rods: Insights and perspectives for active matter, *Annual Review of Condensed Matter Physics* **11**, 441 (2020).
- [26] H. H. Wensink, H. Löwen, M. Marechal, A. Härtel, R. Wittkowski, U. Zimmermann, A. Kaiser, and A. M. Menzel, Differently shaped hard body colloids in confinement: from passive to active particles, *European Physical Journal Special Topics* **222**, 3023 (2013).
- [27] H. Chaté, Dry aligning dilute active matter, *Annual Review of Condensed Matter Physics* **11**, 189 (2020).
- [28] J. Jeggle, J. Stenhammar, and R. Wittkowski, Pair-distribution function of active Brownian spheres in two spatial dimensions: Simulation results and analytic representation, *Journal of Chemical Physics* **152**, 194903 (2020).
- [29] S. C. Takatori and J. F. Brady, Towards a thermodynamics of active matter, *Physical Review E* **91**, 032117

	$u_{-2,0}$ $u_{-1,3}$ $u_{1,2}$	$u_{-2,1}$ $u_{0,0}$ $u_{1,3}$	$u_{-2,2}$ $u_{0,1}$ $u_{2,0}$	$u_{-2,3}$ $u_{0,2}$ $u_{2,1}$	$u_{-1,0}$ $u_{0,3}$ $u_{2,2}$	$u_{-1,1}$ $u_{1,0}$ $u_{2,3}$	$u_{-1,2}$ $u_{1,1}$		
$a_{1,0}^{1,1}$	α	$2.232 \cdot 10^2$	$-3.872 \cdot 10^2$	$2.330 \cdot 10^2$	$-5.646 \cdot 10^1$	$4.744 \cdot 10^0$	$-2.904 \cdot 10^3$	$5.056 \cdot 10^3$	
		$-3.089 \cdot 10^3$	$7.807 \cdot 10^2$	$-6.724 \cdot 10^1$	$1.050 \cdot 10^4$	$-1.820 \cdot 10^4$	$1.105 \cdot 10^4$	$-2.758 \cdot 10^3$	
		$2.318 \cdot 10^2$	$-1.173 \cdot 10^4$	$2.031 \cdot 10^4$	$-1.231 \cdot 10^4$	$3.068 \cdot 10^3$	$-2.586 \cdot 10^2$		
	μ	$2.344 \cdot 10^1$	$-4.131 \cdot 10^1$	$2.676 \cdot 10^1$	$-6.477 \cdot 10^0$	$5.661 \cdot 10^{-1}$	$-3.546 \cdot 10^2$	$6.204 \cdot 10^2$	
		$-3.815 \cdot 10^2$	$9.728 \cdot 10^1$	$-8.596 \cdot 10^0$	$1.379 \cdot 10^3$	$-2.398 \cdot 10^3$	$1.462 \cdot 10^3$	$-3.684 \cdot 10^2$	
		$3.195 \cdot 10^1$	$-1.605 \cdot 10^3$	$2.784 \cdot 10^3$	$-1.693 \cdot 10^3$	$4.256 \cdot 10^2$	$-3.702 \cdot 10^1$		
	ς	$6.353 \cdot 10^0$	$-1.101 \cdot 10^1$	$6.871 \cdot 10^0$	$-1.690 \cdot 10^0$	$1.493 \cdot 10^{-1}$	$-9.639 \cdot 10^1$	$1.686 \cdot 10^2$	
		$-1.039 \cdot 10^2$	$2.669 \cdot 10^1$	$-2.383 \cdot 10^0$	$3.795 \cdot 10^2$	$-6.615 \cdot 10^2$	$4.056 \cdot 10^2$	$-1.030 \cdot 10^2$	
		$9.040 \cdot 10^0$	$-4.481 \cdot 10^2$	$7.800 \cdot 10^2$	$-4.774 \cdot 10^2$	$1.210 \cdot 10^2$	$-1.064 \cdot 10^1$		
	λ	$2.392 \cdot 10^2$	$-4.237 \cdot 10^2$	$2.606 \cdot 10^2$	$-6.228 \cdot 10^1$	$5.159 \cdot 10^0$	$-3.269 \cdot 10^3$	$5.683 \cdot 10^3$	
		$-3.435 \cdot 10^3$	$8.445 \cdot 10^2$	$-7.118 \cdot 10^1$	$1.221 \cdot 10^4$	$-2.098 \cdot 10^4$	$1.249 \cdot 10^4$	$-3.012 \cdot 10^3$	
		$2.446 \cdot 10^2$	$-1.330 \cdot 10^4$	$2.256 \cdot 10^4$	$-1.318 \cdot 10^4$	$3.094 \cdot 10^3$	$-2.409 \cdot 10^2$		
	l_1	$-1.508 \cdot 10^0$	$8.168 \cdot 10^{-1}$	$-4.322 \cdot 10^0$	$4.916 \cdot 10^{-1}$	$-7.876 \cdot 10^{-2}$	$-2.276 \cdot 10^0$	$5.966 \cdot 10^0$	
		$1.605 \cdot 10^{-1}$	$-2.271 \cdot 10^0$	$5.665 \cdot 10^{-1}$	$4.345 \cdot 10^1$	$-6.299 \cdot 10^1$	$1.853 \cdot 10^1$	$3.997 \cdot 10^0$	
		$-1.544 \cdot 10^0$	$-7.013 \cdot 10^1$	$1.055 \cdot 10^2$	$-4.321 \cdot 10^1$	$3.023 \cdot 10^0$	$7.260 \cdot 10^{-1}$		
	l_2	$4.823 \cdot 10^0$	$-3.028 \cdot 10^0$	$4.852 \cdot 10^0$	$-8.761 \cdot 10^{-1}$	$1.399 \cdot 10^{-1}$	$2.107 \cdot 10^1$	$-4.874 \cdot 10^1$	
		$2.484 \cdot 10^1$	$-2.358 \cdot 10^0$	$-4.747 \cdot 10^{-1}$	$-1.598 \cdot 10^2$	$2.585 \cdot 10^2$	$-1.174 \cdot 10^2$	$1.154 \cdot 10^1$	
		$1.509 \cdot 10^0$	$2.100 \cdot 10^2$	$-3.276 \cdot 10^2$	$1.521 \cdot 10^2$	$-2.069 \cdot 10^1$	$-3.834 \cdot 10^{-1}$		
	$a_{1,1}^{1,1}$	α	$1.537 \cdot 10^2$	$-2.357 \cdot 10^2$	$1.223 \cdot 10^2$	$-2.682 \cdot 10^1$	$2.006 \cdot 10^0$	$-2.083 \cdot 10^3$	$3.428 \cdot 10^3$
			$-1.918 \cdot 10^3$	$4.196 \cdot 10^2$	$-2.969 \cdot 10^1$	$6.254 \cdot 10^3$	$-1.004 \cdot 10^4$	$5.349 \cdot 10^3$	$-1.049 \cdot 10^3$
			$5.200 \cdot 10^1$	$-4.127 \cdot 10^3$	$5.726 \cdot 10^3$	$-2.119 \cdot 10^3$	$-1.799 \cdot 10^1$	$8.388 \cdot 10^1$	
μ		$-1.565 \cdot 10^1$	$2.427 \cdot 10^1$	$-1.116 \cdot 10^1$	$2.518 \cdot 10^0$	$-1.850 \cdot 10^{-1}$	$1.821 \cdot 10^2$	$-2.929 \cdot 10^2$	
		$1.598 \cdot 10^2$	$-3.451 \cdot 10^1$	$2.481 \cdot 10^0$	$-5.636 \cdot 10^2$	$8.869 \cdot 10^2$	$-4.642 \cdot 10^2$	$9.180 \cdot 10^1$	
		$-5.321 \cdot 10^0$	$4.219 \cdot 10^2$	$-5.962 \cdot 10^2$	$2.466 \cdot 10^2$	$-2.140 \cdot 10^1$	$-2.936 \cdot 10^0$		
ς		$-4.864 \cdot 10^0$	$7.780 \cdot 10^0$	$-4.109 \cdot 10^0$	$9.791 \cdot 10^{-1}$	$-8.334 \cdot 10^{-2}$	$7.077 \cdot 10^1$	$-1.182 \cdot 10^2$	
		$6.850 \cdot 10^1$	$-1.622 \cdot 10^1$	$1.330 \cdot 10^0$	$-2.572 \cdot 10^2$	$4.269 \cdot 10^2$	$-2.440 \cdot 10^2$	$5.611 \cdot 10^1$	
		$-4.303 \cdot 10^0$	$2.426 \cdot 10^2$	$-3.874 \cdot 10^2$	$2.069 \cdot 10^2$	$-4.169 \cdot 10^1$	$2.344 \cdot 10^0$		
λ		$-1.902 \cdot 10^2$	$2.719 \cdot 10^2$	$-1.214 \cdot 10^2$	$2.254 \cdot 10^1$	$-1.416 \cdot 10^0$	$1.434 \cdot 10^3$	$-2.147 \cdot 10^3$	
		$1.043 \cdot 10^3$	$-1.878 \cdot 10^2$	$1.017 \cdot 10^1$	$-2.721 \cdot 10^3$	$3.603 \cdot 10^3$	$-1.277 \cdot 10^3$	$3.066 \cdot 10^1$	
		$2.335 \cdot 10^1$	$8.382 \cdot 10^2$	$-1.403 \cdot 10^2$	$-9.994 \cdot 10^2$	$6.076 \cdot 10^2$	$-8.329 \cdot 10^1$		
l_1		$-3.393 \cdot 10^1$	$6.168 \cdot 10^1$	$-4.434 \cdot 10^1$	$1.145 \cdot 10^1$	$-1.199 \cdot 10^0$	$6.663 \cdot 10^2$	$-1.230 \cdot 10^3$	
		$8.103 \cdot 10^2$	$-2.256 \cdot 10^2$	$2.245 \cdot 10^1$	$-3.136 \cdot 10^3$	$5.772 \cdot 10^3$	$-3.788 \cdot 10^3$	$1.048 \cdot 10^3$	
		$-1.024 \cdot 10^2$	$4.024 \cdot 10^3$	$-7.328 \cdot 10^3$	$4.737 \cdot 10^3$	$-1.278 \cdot 10^3$	$1.190 \cdot 10^2$		
l_2		$9.589 \cdot 10^1$	$-1.752 \cdot 10^2$	$1.195 \cdot 10^2$	$-3.298 \cdot 10^1$	$3.445 \cdot 10^0$	$-1.806 \cdot 10^3$	$3.335 \cdot 10^3$	
		$-2.205 \cdot 10^3$	$6.186 \cdot 10^2$	$-6.224 \cdot 10^1$	$8.398 \cdot 10^3$	$-1.549 \cdot 10^4$	$1.021 \cdot 10^4$	$-2.852 \cdot 10^3$	
		$2.838 \cdot 10^2$	$-1.120 \cdot 10^4$	$2.056 \cdot 10^4$	$-1.348 \cdot 10^4$	$3.729 \cdot 10^3$	$-3.640 \cdot 10^2$		
l_3		$-6.395 \cdot 10^0$	$9.908 \cdot 10^0$	$-4.681 \cdot 10^0$	$1.588 \cdot 10^0$	$-1.489 \cdot 10^{-1}$	$1.013 \cdot 10^2$	$-1.792 \cdot 10^2$	
		$1.147 \cdot 10^2$	$-3.122 \cdot 10^1$	$3.026 \cdot 10^0$	$-4.036 \cdot 10^2$	$7.263 \cdot 10^2$	$-4.694 \cdot 10^2$	$1.286 \cdot 10^2$	
		$-1.257 \cdot 10^1$	$4.981 \cdot 10^2$	$-9.053 \cdot 10^2$	$5.912 \cdot 10^2$	$-1.641 \cdot 10^2$	$1.639 \cdot 10^1$		

TABLE IV. Fit coefficients of the function $h(\text{Pe}, \Phi_0)$ used to fit the variables of the Fourier coefficients $a_{1,0}^{1,1}$ and $a_{1,1}^{1,1}$ of the function g_{approx} .

- (2015).
- [30] F. Peruani, A. Deutsch, and M. Bär, Nonequilibrium clustering of self-propelled rods, *Physical Review E* **74**, 030904 (2006).
- [31] H. H. Wensink and H. Löwen, Emergent states in dense systems of active rods: from swarming to turbulence, *Journal of Physics: Condensed Matter* **24**, 464130 (2012).
- [32] J.-P. Hansen and I. R. McDonald, *Theory of Simple Liquids: with Applications to Soft Matter*, 4th ed. (Elsevier Academic Press, Oxford, 2009) p. 636.
- [33] M. te Vrugt, J. Bickmann, and R. Wittkowski, How to derive a predictive field theory for active Brownian particles: a step-by-step tutorial, *Journal of Physics: Condensed Matter* **35**, 313001 (2023).
- [34] J. Bickmann and R. Wittkowski, Predictive local field theory for interacting active Brownian spheres in two spatial dimensions, *Journal of Physics: Condensed Matter* **32**, 214001 (2020).
- [35] J. Bickmann and R. Wittkowski, Collective dynamics of active Brownian particles in three spatial dimensions: A predictive field theory, *Physical Review Research* **2**,

	$u_{-2,0}$ $u_{-1,3}$ $u_{1,2}$	$u_{-2,1}$ $u_{0,0}$ $u_{1,3}$	$u_{-2,2}$ $u_{0,1}$ $u_{2,0}$	$u_{-2,3}$ $u_{0,2}$ $u_{2,1}$	$u_{-1,0}$ $u_{0,3}$ $u_{2,2}$	$u_{-1,1}$ $u_{1,0}$ $u_{2,3}$	$u_{-1,2}$ $u_{1,1}$	
$a_{1,2}^{1,1}$	α	$-4.550 \cdot 10^2$	$7.431 \cdot 10^2$	$-4.054 \cdot 10^2$	$7.990 \cdot 10^1$	$-6.723 \cdot 10^0$	$4.553 \cdot 10^3$	$-7.690 \cdot 10^3$
		$4.558 \cdot 10^3$	$-1.128 \cdot 10^3$	$1.058 \cdot 10^2$	$-1.601 \cdot 10^4$	$2.752 \cdot 10^4$	$-1.673 \cdot 10^4$	$4.280 \cdot 10^3$
		$-4.039 \cdot 10^2$	$1.815 \cdot 10^4$	$-3.165 \cdot 10^4$	$1.961 \cdot 10^4$	$-5.160 \cdot 10^3$	$5.038 \cdot 10^2$	
	μ	$4.525 \cdot 10^0$	$-7.379 \cdot 10^0$	$5.319 \cdot 10^0$	$-8.855 \cdot 10^{-1}$	$6.670 \cdot 10^{-2}$	$-4.754 \cdot 10^1$	$7.743 \cdot 10^1$
		$-4.361 \cdot 10^1$	$9.949 \cdot 10^0$	$-8.305 \cdot 10^{-1}$	$1.565 \cdot 10^2$	$-2.571 \cdot 10^2$	$1.462 \cdot 10^2$	$-3.403 \cdot 10^1$
		$2.872 \cdot 10^0$	$-1.567 \cdot 10^2$	$2.567 \cdot 10^2$	$-1.452 \cdot 10^2$	$3.352 \cdot 10^1$	$-2.802 \cdot 10^0$	
	ς	$7.414 \cdot 10^{-1}$	$-1.060 \cdot 10^0$	$6.290 \cdot 10^{-1}$	$-7.840 \cdot 10^{-2}$	$4.185 \cdot 10^{-3}$	$-5.154 \cdot 10^0$	$7.505 \cdot 10^0$
		$-3.576 \cdot 10^0$	$6.477 \cdot 10^{-1}$	$-4.529 \cdot 10^{-2}$	$1.318 \cdot 10^1$	$-1.951 \cdot 10^1$	$9.591 \cdot 10^0$	$-1.841 \cdot 10^0$
		$1.524 \cdot 10^{-1}$	$-1.108 \cdot 10^1$	$1.626 \cdot 10^1$	$-7.796 \cdot 10^0$	$1.445 \cdot 10^0$	$-1.176 \cdot 10^{-1}$	
	λ	$3.156 \cdot 10^2$	$-4.860 \cdot 10^2$	$2.539 \cdot 10^2$	$-4.563 \cdot 10^1$	$2.880 \cdot 10^0$	$-2.374 \cdot 10^3$	$3.573 \cdot 10^3$
		$-1.747 \cdot 10^3$	$3.083 \cdot 10^2$	$-2.002 \cdot 10^1$	$5.970 \cdot 10^3$	$-8.813 \cdot 10^3$	$4.169 \cdot 10^3$	$-7.135 \cdot 10^2$
		$4.982 \cdot 10^1$	$-4.722 \cdot 10^3$	$6.761 \cdot 10^3$	$-3.034 \cdot 10^3$	$4.878 \cdot 10^2$	$-3.951 \cdot 10^1$	
	l_1	$4.419 \cdot 10^0$	$-6.663 \cdot 10^0$	$2.485 \cdot 10^{-1}$	$-7.042 \cdot 10^{-1}$	$5.594 \cdot 10^{-2}$	$-4.428 \cdot 10^1$	$6.892 \cdot 10^1$
		$-3.870 \cdot 10^1$	$9.024 \cdot 10^0$	$-8.073 \cdot 10^{-1}$	$1.518 \cdot 10^2$	$-2.462 \cdot 10^2$	$1.419 \cdot 10^2$	$-3.436 \cdot 10^1$
		$3.115 \cdot 10^0$	$-1.555 \cdot 10^2$	$2.564 \cdot 10^2$	$-1.472 \cdot 10^2$	$3.533 \cdot 10^1$	$-3.070 \cdot 10^0$	
	l_2	$-6.622 \cdot 10^0$	$9.922 \cdot 10^0$	$-2.471 \cdot 10^0$	$9.942 \cdot 10^{-1}$	$-7.683 \cdot 10^{-2}$	$6.155 \cdot 10^1$	$-9.431 \cdot 10^1$
		$5.225 \cdot 10^1$	$-1.200 \cdot 10^1$	$1.074 \cdot 10^0$	$-2.086 \cdot 10^2$	$3.347 \cdot 10^2$	$-1.921 \cdot 10^2$	$4.644 \cdot 10^1$
		$-4.267 \cdot 10^0$	$2.132 \cdot 10^2$	$-3.490 \cdot 10^2$	$1.998 \cdot 10^2$	$-4.804 \cdot 10^1$	$4.225 \cdot 10^0$	
	l_3	$2.626 \cdot 10^{-1}$	$-3.881 \cdot 10^{-1}$	$1.263 \cdot 10^0$	$-1.875 \cdot 10^{-2}$	$1.390 \cdot 10^{-3}$	$-3.737 \cdot 10^0$	$5.609 \cdot 10^0$
		$-2.919 \cdot 10^0$	$5.834 \cdot 10^{-1}$	$-4.529 \cdot 10^{-2}$	$1.324 \cdot 10^1$	$-2.000 \cdot 10^1$	$1.033 \cdot 10^1$	$-2.090 \cdot 10^0$
		$1.289 \cdot 10^{-1}$	$-9.921 \cdot 10^0$	$1.299 \cdot 10^1$	$-5.122 \cdot 10^0$	$2.938 \cdot 10^{-1}$	$1.002 \cdot 10^{-1}$	
$a_{1,3}^{1,1}$	α	$-2.847 \cdot 10^0$	$4.687 \cdot 10^0$	$-2.562 \cdot 10^0$	$4.839 \cdot 10^{-1}$	$-3.158 \cdot 10^{-2}$	$2.115 \cdot 10^1$	$-3.421 \cdot 10^1$
		$1.867 \cdot 10^1$	$-3.941 \cdot 10^0$	$2.518 \cdot 10^{-1}$	$-4.896 \cdot 10^1$	$7.543 \cdot 10^1$	$-3.791 \cdot 10^1$	$6.745 \cdot 10^0$
		$-2.149 \cdot 10^{-1}$	$3.808 \cdot 10^1$	$-5.677 \cdot 10^1$	$2.704 \cdot 10^1$	$-4.293 \cdot 10^0$	$7.958 \cdot 10^{-2}$	
	μ	$-4.493 \cdot 10^{-1}$	$4.666 \cdot 10^{-1}$	$9.993 \cdot 10^{-1}$	$1.056 \cdot 10^{-2}$	$3.005 \cdot 10^{-4}$	$1.770 \cdot 10^0$	$-2.011 \cdot 10^0$
		$5.611 \cdot 10^{-1}$	$-5.189 \cdot 10^{-2}$	$1.590 \cdot 10^{-3}$	$-2.539 \cdot 10^0$	$2.588 \cdot 10^0$	$-6.978 \cdot 10^{-1}$	$7.128 \cdot 10^{-2}$
		$-1.013 \cdot 10^{-2}$	$4.949 \cdot 10^{-2}$	$1.264 \cdot 10^0$	$-1.658 \cdot 10^0$	$6.269 \cdot 10^{-1}$	$-8.216 \cdot 10^{-2}$	
	ς	$1.866 \cdot 10^{-1}$	$-3.058 \cdot 10^{-1}$	$2.697 \cdot 10^{-1}$	$-3.713 \cdot 10^{-2}$	$1.912 \cdot 10^{-3}$	$-1.356 \cdot 10^0$	$2.187 \cdot 10^0$
		$-1.175 \cdot 10^0$	$2.251 \cdot 10^{-1}$	$-8.874 \cdot 10^{-3}$	$3.135 \cdot 10^0$	$-4.656 \cdot 10^0$	$2.156 \cdot 10^0$	$-2.851 \cdot 10^{-1}$
		$-1.181 \cdot 10^{-2}$	$-2.656 \cdot 10^0$	$3.786 \cdot 10^0$	$-1.669 \cdot 10^0$	$1.837 \cdot 10^{-1}$	$1.798 \cdot 10^{-2}$	

TABLE V. Fit coefficients of the function $h(\text{Pe}, \Phi_0)$ used to fit the variables of the Fourier coefficients $a_{1,2}^{1,1}$ and $a_{1,3}^{1,1}$ of the function g_{approx} .

- 033241 (2020).
- [36] J. Bickmann, S. Bröker, J. Jeggle, and R. Wittkowski, Analytical approach to chiral active systems: Suppressed phase separation of interacting Brownian circle swimmers, *Journal of Chemical Physics* **156**, 194904 (2022).
- [37] S. Bröker, J. Bickmann, M. te Vrugt, M. E. Cates, and R. Wittkowski, Orientation-dependent propulsion of active Brownian spheres: from self-advection to programmable cluster shapes, arXiv:2210.13357 (2022).
- [38] M. te Vrugt, T. Frohoff-Hülsmann, E. Heifetz, U. Thiele, and R. Wittkowski, From a microscopic inertial active matter model to the Schrödinger equation, *Nature Communications* **14**, 1302 (2023).
- [39] J. Bickmann, S. Bröker, M. te Vrugt, and R. Wittkowski, Active Brownian particles in external force fields: field-theoretical models, generalized barometric law, and programmable density patterns, arXiv:2202.04423 (2022).
- [40] J. Bickmann, *Collective Dynamics of Active Brownian Particle Systems*, Ph.D. thesis, Westfälische Wilhelms-Universität Münster (2022).
- [41] M. te Vrugt, M. P. Holl, A. Koch, R. Wittkowski, and U. Thiele, Derivation and analysis of a phase field crystal model for a mixture of active and passive particles, *Modelling and Simulation in Materials Science and Engineering* **30**, 084001 (2022).
- [42] J. Bialké, H. Löwen, and T. Speck, Microscopic theory for the phase separation of self-propelled repulsive disks, *EPL* **103**, 30008 (2013).
- [43] R. Wittkowski, J. Stenhammar, and M. E. Cates, Nonequilibrium dynamics of mixtures of active and passive colloidal particles, *New Journal of Physics* **19**, 105003 (2017).
- [44] S. Bröker, M. te Vrugt, J. Jeggle, J. Stenhammar, and R. Wittkowski, Pair-distribution function of active Brownian spheres in three spatial dimensions: simulation results and analytical representation, arXiv:2307.14558 (2023).
- [45] A. Härtel, D. Richard, and T. Speck, Three-body correlations and conditional forces in suspensions of active hard disks, *Physical Review E* **97**, 012606 (2018).

	$u_{-2,0}$ $u_{-1,3}$ $u_{1,2}$	$u_{-2,1}$ $u_{0,0}$ $u_{1,3}$	$u_{-2,2}$ $u_{0,1}$ $u_{2,0}$	$u_{-2,3}$ $u_{0,2}$ $u_{2,1}$	$u_{-1,0}$ $u_{0,3}$ $u_{2,2}$	$u_{-1,1}$ $u_{1,0}$ $u_{2,3}$	$u_{-1,2}$ $u_{1,1}$	
$a_{2,0}^{1,1}$	α	$9.704 \cdot 10^1$	$-1.703 \cdot 10^2$	$1.041 \cdot 10^2$	$-2.672 \cdot 10^1$	$2.230 \cdot 10^0$	$-1.414 \cdot 10^3$	$2.458 \cdot 10^3$
		$-1.493 \cdot 10^3$	$3.692 \cdot 10^2$	$-3.114 \cdot 10^1$	$5.216 \cdot 10^3$	$-8.870 \cdot 10^3$	$5.215 \cdot 10^3$	$-1.234 \cdot 10^3$
		$9.600 \cdot 10^1$	$-5.388 \cdot 10^3$	$8.930 \cdot 10^3$	$-5.059 \cdot 10^3$	$1.126 \cdot 10^3$	$-7.794 \cdot 10^1$	
	μ	$7.785 \cdot 10^{-1}$	$-1.539 \cdot 10^0$	$2.198 \cdot 10^0$	$-3.646 \cdot 10^{-1}$	$3.189 \cdot 10^{-2}$	$-3.099 \cdot 10^1$	$5.089 \cdot 10^1$
		$-2.896 \cdot 10^1$	$6.597 \cdot 10^0$	$-5.123 \cdot 10^{-1}$	$1.110 \cdot 10^2$	$-1.746 \cdot 10^2$	$9.369 \cdot 10^1$	$-1.989 \cdot 10^1$
		$1.360 \cdot 10^0$	$-1.012 \cdot 10^2$	$1.516 \cdot 10^2$	$-7.489 \cdot 10^1$	$1.336 \cdot 10^1$	$-5.810 \cdot 10^{-1}$	
	ς	$-1.871 \cdot 10^0$	$2.992 \cdot 10^0$	$-1.401 \cdot 10^0$	$3.079 \cdot 10^{-1}$	$-2.427 \cdot 10^{-2}$	$1.977 \cdot 10^1$	$-3.245 \cdot 10^1$
		$1.830 \cdot 10^1$	$-4.199 \cdot 10^0$	$3.294 \cdot 10^{-1}$	$-6.655 \cdot 10^1$	$1.078 \cdot 10^2$	$-5.898 \cdot 10^1$	$1.266 \cdot 10^1$
		$-8.753 \cdot 10^{-1}$	$6.347 \cdot 10^1$	$-9.971 \cdot 10^1$	$5.173 \cdot 10^1$	$-1.018 \cdot 10^1$	$5.979 \cdot 10^{-1}$	
	λ	$-2.180 \cdot 10^1$	$3.583 \cdot 10^1$	$-1.625 \cdot 10^1$	$3.838 \cdot 10^0$	$-2.768 \cdot 10^{-1}$	$1.859 \cdot 10^2$	$-3.135 \cdot 10^2$
		$1.770 \cdot 10^2$	$-4.032 \cdot 10^1$	$3.072 \cdot 10^0$	$-6.292 \cdot 10^2$	$1.056 \cdot 10^3$	$-5.876 \cdot 10^2$	$1.268 \cdot 10^2$
		$-8.322 \cdot 10^0$	$5.802 \cdot 10^2$	$-9.244 \cdot 10^2$	$4.688 \cdot 10^2$	$-8.266 \cdot 10^1$	$2.576 \cdot 10^0$	
	l_1	$4.891 \cdot 10^0$	$-8.265 \cdot 10^0$	$6.803 \cdot 10^0$	$-1.384 \cdot 10^0$	$1.189 \cdot 10^{-1}$	$-8.500 \cdot 10^1$	$1.437 \cdot 10^2$
		$-8.671 \cdot 10^1$	$2.100 \cdot 10^1$	$-1.769 \cdot 10^0$	$3.273 \cdot 10^2$	$-5.468 \cdot 10^2$	$3.185 \cdot 10^2$	$-7.444 \cdot 10^1$
		$5.874 \cdot 10^0$	$-3.402 \cdot 10^2$	$5.556 \cdot 10^2$	$-3.109 \cdot 10^2$	$6.808 \cdot 10^1$	$-4.781 \cdot 10^0$	
l_2	$1.115 \cdot 10^1$	$-2.025 \cdot 10^1$	$1.384 \cdot 10^1$	$-2.469 \cdot 10^0$	$1.739 \cdot 10^{-1}$	$-9.773 \cdot 10^1$	$1.754 \cdot 10^2$	
	$-1.021 \cdot 10^2$	$2.235 \cdot 10^1$	$-1.465 \cdot 10^0$	$3.094 \cdot 10^2$	$-5.252 \cdot 10^2$	$2.864 \cdot 10^2$	$-5.508 \cdot 10^1$	
	$2.029 \cdot 10^0$	$-2.584 \cdot 10^2$	$3.937 \cdot 10^2$	$-1.745 \cdot 10^2$	$1.523 \cdot 10^1$	$3.077 \cdot 10^0$		
$a_{2,1}^{1,1}$	α	$-1.094 \cdot 10^2$	$1.951 \cdot 10^2$	$-1.235 \cdot 10^2$	$3.254 \cdot 10^1$	$-2.766 \cdot 10^0$	$1.841 \cdot 10^3$	$-3.156 \cdot 10^3$
		$1.901 \cdot 10^3$	$-4.754 \cdot 10^2$	$4.136 \cdot 10^1$	$-6.471 \cdot 10^3$	$1.082 \cdot 10^4$	$-6.298 \cdot 10^3$	$1.501 \cdot 10^3$
		$-1.204 \cdot 10^2$	$6.228 \cdot 10^3$	$-1.015 \cdot 10^4$	$5.676 \cdot 10^3$	$-1.266 \cdot 10^3$	$9.024 \cdot 10^1$	
	μ	$-8.192 \cdot 10^{-1}$	$-6.898 \cdot 10^{-1}$	$1.965 \cdot 10^0$	$-3.146 \cdot 10^{-1}$	$2.609 \cdot 10^{-2}$	$1.073 \cdot 10^2$	$-6.616 \cdot 10^1$
		$8.105 \cdot 10^0$	$1.020 \cdot 10^0$	$-1.507 \cdot 10^{-1}$	$-1.206 \cdot 10^2$	$-5.044 \cdot 10^1$	$6.991 \cdot 10^1$	$-1.478 \cdot 10^1$
		$5.779 \cdot 10^{-1}$	$5.422 \cdot 10^1$	$1.342 \cdot 10^1$	$1.708 \cdot 10^1$	$-1.914 \cdot 10^1$	$3.222 \cdot 10^0$	
	ς	$3.199 \cdot 10^1$	$-3.146 \cdot 10^1$	$1.059 \cdot 10^1$	$-1.381 \cdot 10^0$	$5.732 \cdot 10^{-2}$	$-2.171 \cdot 10^2$	$1.909 \cdot 10^2$
		$-4.618 \cdot 10^1$	$1.508 \cdot 10^0$	$2.979 \cdot 10^{-1}$	$2.355 \cdot 10^2$	$8.319 \cdot 10^0$	$-1.493 \cdot 10^2$	$5.249 \cdot 10^1$
		$-4.398 \cdot 10^0$	$4.511 \cdot 10^0$	$-2.435 \cdot 10^2$	$1.897 \cdot 10^2$	$-3.457 \cdot 10^1$	$-1.988 \cdot 10^{-1}$	
	λ	$-2.032 \cdot 10^1$	$1.617 \cdot 10^0$	$6.113 \cdot 10^0$	$-6.918 \cdot 10^{-1}$	$2.301 \cdot 10^{-2}$	$4.404 \cdot 10^1$	$3.828 \cdot 10^2$
		$-2.828 \cdot 10^2$	$5.678 \cdot 10^1$	$-2.899 \cdot 10^0$	$3.118 \cdot 10^3$	$-4.918 \cdot 10^3$	$2.232 \cdot 10^3$	$-3.281 \cdot 10^2$
		$7.820 \cdot 10^0$	$-2.315 \cdot 10^3$	$1.913 \cdot 10^3$	$4.369 \cdot 10^2$	$-5.534 \cdot 10^2$	$9.085 \cdot 10^1$	
	l_1	$1.143 \cdot 10^1$	$-1.936 \cdot 10^1$	$1.154 \cdot 10^1$	$-2.091 \cdot 10^0$	$1.454 \cdot 10^{-1}$	$-2.465 \cdot 10^2$	$3.323 \cdot 10^2$
		$-1.507 \cdot 10^2$	$2.714 \cdot 10^1$	$-1.687 \cdot 10^0$	$5.414 \cdot 10^2$	$-6.030 \cdot 10^2$	$1.954 \cdot 10^2$	$-1.561 \cdot 10^1$
		$-5.910 \cdot 10^{-1}$	$-2.827 \cdot 10^2$	$2.245 \cdot 10^2$	$-1.666 \cdot 10^1$	$-1.239 \cdot 10^1$	$8.833 \cdot 10^{-1}$	

TABLE VI. Fit coefficients of the function $h(\text{Pe}, \Phi_0)$ used to fit the variables of the Fourier coefficients $a_{2,0}^{1,1}$ and $a_{2,1}^{1,1}$ of the function g_{approx} .

- [46] F. J. Schwarzendahl and M. G. Mazza, Hydrodynamic interactions dominate the structure of active swimmers' pair distribution functions, *Journal of Chemical Physics* **150**, 184902 (2019).
- [47] T. C. Adhyapak, S. Ramaswamy, and J. Toner, Live soap: stability, order, and fluctuations in apolar active smectics, *Physical Review Letters* **110**, 118102 (2013).
- [48] S. Shankar, A. Souslov, M. J. Bowick, M. C. Marchetti, and V. Vitelli, Topological active matter, *Nature Reviews Physics* **4**, 380 (2022).
- [49] J. Tailleur and M. E. Cates, Statistical mechanics of interacting run-and-tumble bacteria, *Physical Review Letters* **100**, 218103 (2008).
- [50] J. Zhang, R. Alert, J. Yan, N. S. Wingreen, and S. Granick, Active phase separation by turning towards regions of higher density, *Nature Physics* **17**, 961 (2021).
- [51] M. C. Bott, F. Winterhalter, M. Marechal, A. Sharma, J. M. Brader, and R. Wittmann, Isotropic-nematic transition of self-propelled rods in three dimensions, *Physical Review E* **98**, 012601 (2018).
- [52] B. ten Hagen, S. van Teeffelen, and H. Löwen, Brownian motion of a self-propelled particle, *Journal of Physics: Condensed Matter* **23**, 194119 (2011).
- [53] Y. Han, A. M. Alsayed, M. Nobili, J. Zhang, T. C. Lubensky, and A. G. Yodh, Brownian motion of an ellipsoid, *Science* **314**, 626 (2006).
- [54] J. K. G. Dhont, *An Introduction to Dynamics of Colloids*, Studies in Interface Science (Elsevier Science, Amsterdam, 1996).
- [55] M. von Smoluchowski, Über Brownsche Molekularbewegung unter Einwirkung äußerer Kräfte und deren Zusammenhang mit der verallgemeinerten Diffusionsgleichung, *Annalen der Physik* **353**, 1103 (1916).
- [56] M. von Smoluchowski, Zur kinetischen Theorie der Brownschen Molekularbewegung und der Suspensionen, *Annalen der Physik* **326**, 756 (1906).

	$u_{-2,0}$ $u_{-1,3}$ $u_{1,2}$	$u_{-2,1}$ $u_{0,0}$ $u_{1,3}$	$u_{-2,2}$ $u_{0,1}$ $u_{2,0}$	$u_{-2,3}$ $u_{0,2}$ $u_{2,1}$	$u_{-1,0}$ $u_{0,3}$ $u_{2,2}$	$u_{-1,1}$ $u_{1,0}$ $u_{2,3}$	$u_{-1,2}$ $u_{1,1}$	
$a_{2,2}^{1,1}$	α	$-1.405 \cdot 10^2$	$2.460 \cdot 10^2$	$-1.517 \cdot 10^2$	$3.902 \cdot 10^1$	$-3.367 \cdot 10^0$	$2.090 \cdot 10^3$	$-3.634 \cdot 10^3$
		$2.228 \cdot 10^3$	$-5.681 \cdot 10^2$	$5.122 \cdot 10^1$	$-7.946 \cdot 10^3$	$1.373 \cdot 10^4$	$-8.334 \cdot 10^3$	$2.097 \cdot 10^3$
		$-1.831 \cdot 10^2$	$8.741 \cdot 10^3$	$-1.498 \cdot 10^4$	$8.977 \cdot 10^3$	$-2.209 \cdot 10^3$	$1.855 \cdot 10^2$	
	μ	$1.620 \cdot 10^0$	$-2.803 \cdot 10^0$	$2.482 \cdot 10^0$	$-3.702 \cdot 10^{-1}$	$3.029 \cdot 10^{-2}$	$-2.211 \cdot 10^1$	$3.686 \cdot 10^1$
		$-2.137 \cdot 10^1$	$5.031 \cdot 10^0$	$-4.117 \cdot 10^{-1}$	$7.938 \cdot 10^1$	$-1.306 \cdot 10^2$	$7.396 \cdot 10^1$	$-1.677 \cdot 10^1$
		$1.256 \cdot 10^0$	$-7.736 \cdot 10^1$	$1.234 \cdot 10^2$	$-6.635 \cdot 10^1$	$1.368 \cdot 10^1$	$-8.603 \cdot 10^{-1}$	
	ς	$-7.195 \cdot 10^{-1}$	$1.288 \cdot 10^0$	$-6.951 \cdot 10^{-1}$	$1.821 \cdot 10^{-1}$	$-1.583 \cdot 10^{-2}$	$1.258 \cdot 10^1$	$-2.125 \cdot 10^1$
		$1.239 \cdot 10^1$	$-2.935 \cdot 10^0$	$2.353 \cdot 10^{-1}$	$-4.385 \cdot 10^1$	$7.156 \cdot 10^1$	$-3.975 \cdot 10^1$	$8.716 \cdot 10^0$
		$-6.106 \cdot 10^{-1}$	$4.209 \cdot 10^1$	$-6.663 \cdot 10^1$	$3.528 \cdot 10^1$	$-7.138 \cdot 10^0$	$4.277 \cdot 10^{-1}$	
	λ	$4.691 \cdot 10^1$	$-7.341 \cdot 10^1$	$3.965 \cdot 10^1$	$-7.497 \cdot 10^0$	$6.431 \cdot 10^{-1}$	$-3.617 \cdot 10^2$	$5.994 \cdot 10^2$
		$-3.540 \cdot 10^2$	$9.309 \cdot 10^1$	$-9.143 \cdot 10^0$	$1.390 \cdot 10^3$	$-2.421 \cdot 10^3$	$1.503 \cdot 10^3$	$-3.970 \cdot 10^2$
		$3.808 \cdot 10^1$	$-1.629 \cdot 10^3$	$2.862 \cdot 10^3$	$-1.775 \cdot 10^3$	$4.650 \cdot 10^2$	$-4.425 \cdot 10^1$	
	l_1	$2.578 \cdot 10^0$	$-4.606 \cdot 10^0$	$5.239 \cdot 10^0$	$-1.072 \cdot 10^0$	$9.280 \cdot 10^{-2}$	$-7.443 \cdot 10^1$	$1.275 \cdot 10^2$
		$-7.805 \cdot 10^1$	$1.806 \cdot 10^1$	$-1.448 \cdot 10^0$	$2.807 \cdot 10^2$	$-4.642 \cdot 10^2$	$2.633 \cdot 10^2$	$-5.721 \cdot 10^1$
		$4.234 \cdot 10^0$	$-2.754 \cdot 10^2$	$4.379 \cdot 10^2$	$-2.329 \cdot 10^2$	$4.611 \cdot 10^1$	$-2.975 \cdot 10^0$	
$a_{2,3}^{1,1}$	α	$1.134 \cdot 10^1$	$-1.939 \cdot 10^1$	$1.167 \cdot 10^1$	$-2.898 \cdot 10^0$	$2.343 \cdot 10^{-1}$	$-1.372 \cdot 10^2$	$2.440 \cdot 10^2$
		$-1.533 \cdot 10^2$	$3.964 \cdot 10^1$	$-3.436 \cdot 10^0$	$5.531 \cdot 10^2$	$-9.779 \cdot 10^2$	$6.043 \cdot 10^2$	$-1.506 \cdot 10^2$
		$1.213 \cdot 10^1$	$-6.216 \cdot 10^2$	$1.069 \cdot 10^3$	$-6.315 \cdot 10^2$	$1.454 \cdot 10^2$	$-1.001 \cdot 10^1$	
	μ	$2.376 \cdot 10^1$	$-3.090 \cdot 10^1$	$1.484 \cdot 10^1$	$-2.424 \cdot 10^0$	$1.419 \cdot 10^{-1}$	$-4.862 \cdot 10^2$	$6.347 \cdot 10^2$
		$-2.575 \cdot 10^2$	$3.793 \cdot 10^1$	$-1.727 \cdot 10^0$	$8.198 \cdot 10^2$	$-6.607 \cdot 10^2$	$-4.447 \cdot 10^1$	$9.180 \cdot 10^1$
		$-1.117 \cdot 10^1$	$-1.413 \cdot 10^2$	$-3.357 \cdot 10^2$	$4.714 \cdot 10^2$	$-1.283 \cdot 10^2$	$4.885 \cdot 10^0$	
	ς	$-1.651 \cdot 10^{-1}$	$6.003 \cdot 10^{-1}$	$-3.562 \cdot 10^{-1}$	$1.373 \cdot 10^{-1}$	$-1.388 \cdot 10^{-2}$	$-2.796 \cdot 10^1$	$3.273 \cdot 10^1$
		$-9.689 \cdot 10^0$	$1.712 \cdot 10^{-1}$	$1.040 \cdot 10^{-1}$	$1.833 \cdot 10^1$	$3.209 \cdot 10^1$	$-5.791 \cdot 10^1$	$2.129 \cdot 10^1$
		$-1.965 \cdot 10^0$	$4.589 \cdot 10^1$	$-1.253 \cdot 10^2$	$9.524 \cdot 10^1$	$-2.239 \cdot 10^1$	$8.989 \cdot 10^{-1}$	

TABLE VII. Fit coefficients of the function $h(\text{Pe}, \Phi_0)$ used to fit the variables of the Fourier coefficients $a_{2,2}^{1,1}$ and $a_{2,3}^{1,1}$ of the function g_{approx} .

- [57] A. Einstein, Über die von der molekularkinetischen Theorie der Wärme geforderte Bewegung von in ruhenden Flüssigkeiten suspendierten Teilchen, *Annalen der Physik* **322**, 549 (1905).
- [58] S. Plimpton, Fast parallel algorithms for short-range molecular dynamics, *Journal of Computational Physics* **117**, 1 (1995).
- [59] S. Bröker, *Computer simulations of active Brownian particles and active colloidal liquid crystals*, Ph.D. thesis, Westfälische Wilhelms-Universität Münster (2023).
- [60] A. Doostmohammadi, J. Ignés-Mullol, J. M. Yeomans, and F. Sagués, Active nematics, *Nature Communications* **9**, 3246 (2018).
- [61] B. Palmer, S. Chen, P. Govan, W. Yan, and T. Gao, Understanding topological defects in fluidized dry active nematics, *Soft Matter* **18**, 1013 (2022).
- [62] F. Peruani, J. Starruß, V. Jakovljevic, L. Søgaard-Andersen, A. Deutsch, and M. Bär, Collective motion and nonequilibrium cluster formation in colonies of gliding bacteria, *Physical Review Letters* **108**, 098102 (2012).
- [63] C. W. Harvey, M. Alber, L. S. Tsimring, and I. S. Aranson, Continuum modeling of myxobacteria clustering, *New Journal of Physics* **15**, 035029 (2013).
- [64] A. P. Solon, J. Stenhammar, M. E. Cates, Y. Kafri, and J. Tailleur, Generalized thermodynamics of motility-induced phase separation: phase equilibria, Laplace pressure, and change of ensembles, *New Journal of Physics* **20**, 075001 (2018).
- [65] L. Caprini, U. M. B. Marconi, and A. Puglisi, Spontaneous velocity alignment in motility-induced phase separation, *Physical Review Letters* **124**, 078001 (2020).
- [66] F. C. Keber, E. Loiseau, T. Sanchez, S. J. DeCamp, L. Giomi, M. J. Bowick, M. C. Marchetti, Z. Dogic, and A. R. Bausch, Topology and dynamics of active nematic vesicles, *Science* **345**, 1135 (2014).
- [67] J. Hardoïin, R. Hughes, A. Doostmohammadi, J. Laurent, T. Lopez-Leon, J. M. Yeomans, J. Ignés-Mullol, and F. Sagués, Reconfigurable flows and defect landscape of confined active nematics, *Communications Physics* **2**, 121 (2019).
- [68] R. Wittmann, L. B. G. Cortes, H. Löwen, and D. G. A. L. Aarts, Particle-resolved topological defects of smectic colloidal liquid crystals in extreme confinement, *Nature Communications* **12**, 623 (2021).
- [69] P. A. Monderkamp, R. Wittmann, M. te Vrugt, A. Voigt, R. Wittkowski, and H. Löwen, Topological fine structure of smectic grain boundaries and tetratic disclination lines within three-dimensional smectic liquid crystals, *Physical Chemistry Chemical Physics* **24**, 15691 (2022).
- [70] A. Martín-Gómez, D. Levis, A. Díaz-Guilera, and I. Pagonabarraga, Collective motion of active Brownian particles with polar alignment, *Soft Matter* **14**, 2610 (2018).
- [71] J. Toner and Y. Tu, Flocks, herds, and schools: A quantitative theory of flocking, *Physical Review E* **58**, 4828 (1998).

	$u_{-2,0}$ $u_{-1,3}$ $u_{1,2}$	$u_{-2,1}$ $u_{0,0}$ $u_{1,3}$	$u_{-2,2}$ $u_{0,1}$ $u_{2,0}$	$u_{-2,3}$ $u_{0,2}$ $u_{2,1}$	$u_{-1,0}$ $u_{0,3}$ $u_{2,2}$	$u_{-1,1}$ $u_{1,0}$ $u_{2,3}$	$u_{-1,2}$ $u_{1,1}$	
$a_{3,0}^{1,1}$	α	$-9.187 \cdot 10^1$	$1.695 \cdot 10^2$	$-1.125 \cdot 10^2$	$3.173 \cdot 10^1$	$-2.945 \cdot 10^0$	$1.385 \cdot 10^3$	$-2.444 \cdot 10^3$
		$1.520 \cdot 10^3$	$-3.939 \cdot 10^2$	$3.706 \cdot 10^1$	$-5.606 \cdot 10^3$	$9.858 \cdot 10^3$	$-6.108 \cdot 10^3$	$1.574 \cdot 10^3$
		$-1.438 \cdot 10^2$	$6.281 \cdot 10^3$	$-1.091 \cdot 10^4$	$6.641 \cdot 10^3$	$-1.657 \cdot 10^3$	$1.421 \cdot 10^2$	
	μ	$1.023 \cdot 10^0$	$-1.850 \cdot 10^0$	$2.113 \cdot 10^0$	$-1.719 \cdot 10^{-1}$	$1.616 \cdot 10^{-3}$	$-2.750 \cdot 10^0$	$3.422 \cdot 10^0$
		$-5.686 \cdot 10^{-1}$	$-4.594 \cdot 10^{-1}$	$1.155 \cdot 10^{-1}$	$-1.076 \cdot 10^{-1}$	$4.370 \cdot 10^0$	$-6.972 \cdot 10^0$	$3.144 \cdot 10^0$
		$-4.404 \cdot 10^{-1}$	$4.671 \cdot 10^0$	$-1.117 \cdot 10^1$	$1.041 \cdot 10^1$	$-3.801 \cdot 10^0$	$5.062 \cdot 10^{-1}$	
	ς	$-2.744 \cdot 10^{-1}$	$6.240 \cdot 10^{-1}$	$-3.768 \cdot 10^{-1}$	$1.744 \cdot 10^{-1}$	$-2.176 \cdot 10^{-2}$	$7.874 \cdot 10^0$	$-1.476 \cdot 10^1$
		$1.005 \cdot 10^1$	$-2.894 \cdot 10^0$	$3.003 \cdot 10^{-1}$	$-3.430 \cdot 10^1$	$6.221 \cdot 10^1$	$-4.059 \cdot 10^1$	$1.114 \cdot 10^1$
		$-1.082 \cdot 10^0$	$4.065 \cdot 10^1$	$-7.258 \cdot 10^1$	$4.654 \cdot 10^1$	$-1.255 \cdot 10^1$	$1.210 \cdot 10^0$	
	λ	$3.115 \cdot 10^1$	$-5.425 \cdot 10^1$	$3.174 \cdot 10^1$	$-4.642 \cdot 10^0$	$1.550 \cdot 10^{-1}$	$7.791 \cdot 10^1$	$-1.435 \cdot 10^2$
		$1.092 \cdot 10^2$	$-3.885 \cdot 10^1$	$4.495 \cdot 10^0$	$-6.371 \cdot 10^2$	$1.091 \cdot 10^3$	$-6.830 \cdot 10^2$	$1.858 \cdot 10^2$
		$-1.716 \cdot 10^1$	$7.705 \cdot 10^2$	$-1.290 \cdot 10^3$	$7.779 \cdot 10^2$	$-1.994 \cdot 10^2$	$1.780 \cdot 10^1$	
	l_1	$1.010 \cdot 10^0$	$-1.568 \cdot 10^0$	$2.216 \cdot 10^0$	$-2.636 \cdot 10^{-1}$	$1.991 \cdot 10^{-2}$	$-1.481 \cdot 10^1$	$2.481 \cdot 10^1$
		$-1.474 \cdot 10^1$	$3.528 \cdot 10^0$	$-2.859 \cdot 10^{-1}$	$5.360 \cdot 10^1$	$-8.951 \cdot 10^1$	$5.175 \cdot 10^1$	$-1.216 \cdot 10^1$
		$9.350 \cdot 10^{-1}$	$-5.565 \cdot 10^1$	$9.180 \cdot 10^1$	$-5.246 \cdot 10^1$	$1.204 \cdot 10^1$	$-9.006 \cdot 10^{-1}$	
	l_2	$2.794 \cdot 10^0$	$-3.433 \cdot 10^0$	$4.250 \cdot 10^0$	$-7.995 \cdot 10^{-1}$	$8.203 \cdot 10^{-2}$	$-5.852 \cdot 10^1$	$9.979 \cdot 10^1$
		$-6.251 \cdot 10^1$	$1.606 \cdot 10^1$	$-1.448 \cdot 10^0$	$2.237 \cdot 10^2$	$-3.851 \cdot 10^2$	$2.327 \cdot 10^2$	$-5.745 \cdot 10^1$
		$4.846 \cdot 10^0$	$-2.392 \cdot 10^2$	$4.053 \cdot 10^2$	$-2.382 \cdot 10^2$	$5.631 \cdot 10^1$	$-4.432 \cdot 10^0$	
	l_3	$1.564 \cdot 10^1$	$-2.873 \cdot 10^1$	$2.071 \cdot 10^1$	$-4.364 \cdot 10^0$	$3.842 \cdot 10^{-1}$	$-1.974 \cdot 10^2$	$3.585 \cdot 10^2$
		$-2.205 \cdot 10^2$	$5.339 \cdot 10^1$	$-4.705 \cdot 10^0$	$7.281 \cdot 10^2$	$-1.285 \cdot 10^3$	$7.758 \cdot 10^2$	$-1.881 \cdot 10^2$
		$1.637 \cdot 10^1$	$-8.054 \cdot 10^2$	$1.388 \cdot 10^3$	$-8.240 \cdot 10^2$	$1.977 \cdot 10^2$	$-1.698 \cdot 10^1$	
$a_{3,1}^{1,1}$	α	$1.735 \cdot 10^2$	$-3.408 \cdot 10^2$	$2.453 \cdot 10^2$	$-7.632 \cdot 10^1$	$7.783 \cdot 10^0$	$-2.895 \cdot 10^3$	$5.460 \cdot 10^3$
		$-3.709 \cdot 10^3$	$1.073 \cdot 10^3$	$-1.111 \cdot 10^2$	$1.271 \cdot 10^4$	$-2.371 \cdot 10^4$	$1.590 \cdot 10^4$	$-4.549 \cdot 10^3$
		$4.683 \cdot 10^2$	$-1.637 \cdot 10^4$	$3.042 \cdot 10^4$	$-2.031 \cdot 10^4$	$5.786 \cdot 10^3$	$-5.915 \cdot 10^2$	
	μ	$-2.965 \cdot 10^0$	$5.581 \cdot 10^0$	$-2.373 \cdot 10^0$	$1.075 \cdot 10^0$	$-1.222 \cdot 10^{-1}$	$4.635 \cdot 10^1$	$-8.795 \cdot 10^1$
		$5.999 \cdot 10^1$	$-1.771 \cdot 10^1$	$1.908 \cdot 10^0$	$-2.149 \cdot 10^2$	$4.042 \cdot 10^2$	$-2.734 \cdot 10^2$	$7.918 \cdot 10^1$
		$-8.309 \cdot 10^0$	$2.907 \cdot 10^2$	$-5.437 \cdot 10^2$	$3.650 \cdot 10^2$	$-1.047 \cdot 10^2$	$1.085 \cdot 10^1$	
	ς	$-1.932 \cdot 10^0$	$3.621 \cdot 10^0$	$-2.242 \cdot 10^0$	$7.041 \cdot 10^{-1}$	$-7.556 \cdot 10^{-2}$	$3.221 \cdot 10^1$	$-5.975 \cdot 10^1$
		$3.984 \cdot 10^1$	$-1.138 \cdot 10^1$	$1.179 \cdot 10^0$	$-1.444 \cdot 10^2$	$2.660 \cdot 10^2$	$-1.761 \cdot 10^2$	$4.969 \cdot 10^1$
		$-5.048 \cdot 10^0$	$1.905 \cdot 10^2$	$-3.503 \cdot 10^2$	$2.311 \cdot 10^2$	$-6.497 \cdot 10^1$	$6.572 \cdot 10^0$	
	l_1	$9.450 \cdot 10^{-1}$	$-3.362 \cdot 10^0$	$3.900 \cdot 10^0$	$-7.771 \cdot 10^{-1}$	$7.043 \cdot 10^{-2}$	$-3.741 \cdot 10^1$	$6.990 \cdot 10^1$
		$-4.450 \cdot 10^1$	$1.154 \cdot 10^1$	$-1.039 \cdot 10^0$	$1.593 \cdot 10^2$	$-2.839 \cdot 10^2$	$1.773 \cdot 10^2$	$-4.609 \cdot 10^1$
		$4.177 \cdot 10^0$	$-1.975 \cdot 10^2$	$3.509 \cdot 10^2$	$-2.208 \cdot 10^2$	$5.824 \cdot 10^1$	$-5.411 \cdot 10^0$	
	l_2	$3.221 \cdot 10^0$	$-5.575 \cdot 10^0$	$4.823 \cdot 10^0$	$-8.681 \cdot 10^{-1}$	$8.625 \cdot 10^{-2}$	$-3.277 \cdot 10^1$	$6.018 \cdot 10^1$
		$-4.004 \cdot 10^1$	$1.143 \cdot 10^1$	$-1.195 \cdot 10^0$	$1.401 \cdot 10^2$	$-2.607 \cdot 10^2$	$1.748 \cdot 10^2$	$-5.049 \cdot 10^1$
		$5.320 \cdot 10^0$	$-1.984 \cdot 10^2$	$3.724 \cdot 10^2$	$-2.528 \cdot 10^2$	$7.422 \cdot 10^1$	$-7.948 \cdot 10^0$	

TABLE VIII. Fit coefficients of the function $h(\text{Pe}, \Phi_0)$ used to fit the variables of the Fourier coefficients $a_{3,0}^{1,1}$ and $a_{3,1}^{1,1}$ of the function g_{approx} .

- [72] B. Mahault, F. Ginelli, and H. Chaté, Quantitative assessment of the Toner and Tu theory of polar flocks, *Physical Review Letters* **123**, 218001 (2019).
- [73] J. Stenhammar, D. Marenduzzo, R. J. Allen, and M. E. Cates, Phase behaviour of active Brownian particles: the role of dimensionality, *Soft Matter* **10**, 1489 (2014).
- [74] T. Weber and A. Simonov, The three-dimensional pair distribution function analysis of disordered single crystals: basic concepts, *Zeitschrift für Kristallographie* **227**, 238 (2012).
- [75] J. Bialké, H. Löwen, and T. Speck, Microscopic theory for the phase separation of self-propelled repulsive disks, *EPL* **103**, 30008 (2013).
- [76] J. Bialké, T. Speck, and H. Löwen, Active colloidal suspensions: Clustering and phase behavior, *Journal of Non-Crystalline Solids* **407**, 367 (2015).
- [77] J. K. G. Dhont, G. W. Park, and W. J. Briels, Motility-induced inter-particle correlations and dynamics: a microscopic approach for active Brownian particles, *Soft Matter* **17**, 5613 (2021).
- [78] Supplementary Material for this article is available at <https://doi.org/10.5281/zenodo.8186700>.
- [79] J. G. Gay and B. J. Berne, Modification of the overlap potential to mimic a linear site-site potential, *Journal of Chemical Physics* **74**, 3316 (1981).
- [80] B. J. Berne and P. Pechukas, Gaussian model potentials for molecular interactions, *Journal of Chemical Physics*

	$u_{-2,0}$ $u_{-1,3}$ $u_{1,2}$	$u_{-2,1}$ $u_{0,0}$ $u_{1,3}$	$u_{-2,2}$ $u_{0,1}$ $u_{2,0}$	$u_{-2,3}$ $u_{0,2}$ $u_{2,1}$	$u_{-1,0}$ $u_{0,3}$ $u_{2,2}$	$u_{-1,1}$ $u_{1,0}$ $u_{2,3}$	$u_{-1,2}$ $u_{1,1}$	
$a_{3,2}^{1,1}$	α	$-4.758 \cdot 10^1$	$8.182 \cdot 10^1$	$-4.906 \cdot 10^1$	$1.216 \cdot 10^1$	$-9.177 \cdot 10^{-1}$	$4.377 \cdot 10^2$	$-7.528 \cdot 10^2$
		$4.561 \cdot 10^2$	$-1.164 \cdot 10^2$	$1.085 \cdot 10^1$	$-1.768 \cdot 10^3$	$3.137 \cdot 10^3$	$-1.988 \cdot 10^3$	$5.375 \cdot 10^2$
		$-5.239 \cdot 10^1$	$2.143 \cdot 10^3$	$-3.813 \cdot 10^3$	$2.414 \cdot 10^3$	$-6.426 \cdot 10^2$	$5.942 \cdot 10^1$	
	μ	$1.154 \cdot 10^0$	$-1.292 \cdot 10^0$	$1.221 \cdot 10^0$	$9.169 \cdot 10^{-4}$	$-3.697 \cdot 10^{-3}$	$1.100 \cdot 10^0$	$-5.014 \cdot 10^0$
		$4.437 \cdot 10^0$	$-1.308 \cdot 10^0$	$1.142 \cdot 10^{-1}$	$-2.874 \cdot 10^1$	$5.428 \cdot 10^1$	$-3.485 \cdot 10^1$	$8.754 \cdot 10^0$
		$-6.652 \cdot 10^{-1}$	$3.055 \cdot 10^1$	$-4.955 \cdot 10^1$	$2.562 \cdot 10^1$	$-3.826 \cdot 10^0$	$-1.610 \cdot 10^{-1}$	
	ς	$-9.259 \cdot 10^{-1}$	$2.057 \cdot 10^0$	$-1.393 \cdot 10^0$	$3.862 \cdot 10^{-1}$	$-3.444 \cdot 10^{-2}$	$2.492 \cdot 10^1$	$-4.376 \cdot 10^1$
		$2.640 \cdot 10^1$	$-6.422 \cdot 10^0$	$5.297 \cdot 10^{-1}$	$-1.045 \cdot 10^2$	$1.766 \cdot 10^2$	$-1.025 \cdot 10^2$	$2.384 \cdot 10^1$
		$-1.803 \cdot 10^0$	$1.053 \cdot 10^2$	$-1.700 \cdot 10^2$	$9.204 \cdot 10^1$	$-1.871 \cdot 10^1$	$1.019 \cdot 10^0$	
	λ	$-5.877 \cdot 10^1$	$1.221 \cdot 10^2$	$-8.755 \cdot 10^1$	$2.550 \cdot 10^1$	$-2.246 \cdot 10^0$	$1.295 \cdot 10^3$	$-2.292 \cdot 10^3$
		$1.422 \cdot 10^3$	$-3.551 \cdot 10^2$	$3.063 \cdot 10^1$	$-6.408 \cdot 10^3$	$1.112 \cdot 10^4$	$-6.776 \cdot 10^3$	$1.674 \cdot 10^3$
		$-1.381 \cdot 10^2$	$6.756 \cdot 10^3$	$-1.116 \cdot 10^4$	$6.309 \cdot 10^3$	$-1.350 \cdot 10^3$	$8.155 \cdot 10^1$	
	l_1	$1.133 \cdot 10^0$	$-1.681 \cdot 10^0$	$2.273 \cdot 10^0$	$-3.282 \cdot 10^{-1}$	$2.848 \cdot 10^{-2}$	$-2.147 \cdot 10^1$	$3.769 \cdot 10^1$
		$-2.373 \cdot 10^1$	$5.676 \cdot 10^0$	$-4.615 \cdot 10^{-1}$	$8.257 \cdot 10^1$	$-1.410 \cdot 10^2$	$8.190 \cdot 10^1$	$-1.819 \cdot 10^1$
		$1.345 \cdot 10^0$	$-8.385 \cdot 10^1$	$1.373 \cdot 10^2$	$-7.486 \cdot 10^1$	$1.530 \cdot 10^1$	$-1.018 \cdot 10^0$	
$a_{3,3}^{1,1}$	α	$8.963 \cdot 10^1$	$-1.267 \cdot 10^2$	$5.148 \cdot 10^1$	$-4.728 \cdot 10^0$	$1.227 \cdot 10^{-1}$	$-5.759 \cdot 10^2$	$8.778 \cdot 10^2$
		$-4.414 \cdot 10^2$	$8.645 \cdot 10^1$	$-4.872 \cdot 10^0$	$8.407 \cdot 10^2$	$-1.145 \cdot 10^3$	$4.502 \cdot 10^2$	$-3.847 \cdot 10^1$
		$-5.368 \cdot 10^0$	$-5.436 \cdot 10^2$	$8.146 \cdot 10^2$	$-4.242 \cdot 10^2$	$1.062 \cdot 10^2$	$-1.294 \cdot 10^1$	
	μ	$5.952 \cdot 10^{-1}$	$-1.424 \cdot 10^0$	$2.122 \cdot 10^0$	$-2.586 \cdot 10^{-1}$	$2.226 \cdot 10^{-2}$	$-1.198 \cdot 10^1$	$2.198 \cdot 10^1$
		$-1.417 \cdot 10^1$	$3.745 \cdot 10^0$	$-3.407 \cdot 10^{-1}$	$5.059 \cdot 10^1$	$-9.022 \cdot 10^1$	$5.654 \cdot 10^1$	$-1.464 \cdot 10^1$
		$1.307 \cdot 10^0$	$-6.076 \cdot 10^1$	$1.077 \cdot 10^2$	$-6.711 \cdot 10^1$	$1.736 \cdot 10^1$	$-1.565 \cdot 10^0$	
	ς	$3.455 \cdot 10^{-1}$	$-6.052 \cdot 10^{-1}$	$5.012 \cdot 10^{-1}$	$-1.026 \cdot 10^{-1}$	$8.040 \cdot 10^{-3}$	$-5.525 \cdot 10^0$	$9.662 \cdot 10^0$
		$-5.991 \cdot 10^0$	$1.541 \cdot 10^0$	$-1.334 \cdot 10^{-1}$	$2.168 \cdot 10^1$	$-3.769 \cdot 10^1$	$2.311 \cdot 10^1$	$-5.850 \cdot 10^0$
		$4.986 \cdot 10^{-1}$	$-2.503 \cdot 10^1$	$4.333 \cdot 10^1$	$-2.631 \cdot 10^1$	$6.539 \cdot 10^0$	$-5.410 \cdot 10^{-1}$	
	λ	$2.583 \cdot 10^1$	$-4.962 \cdot 10^1$	$3.725 \cdot 10^1$	$-7.631 \cdot 10^0$	$5.888 \cdot 10^{-1}$	$-2.856 \cdot 10^2$	$4.923 \cdot 10^2$
		$-3.094 \cdot 10^2$	$7.854 \cdot 10^1$	$-6.613 \cdot 10^0$	$1.060 \cdot 10^3$	$-1.809 \cdot 10^3$	$1.102 \cdot 10^3$	$-2.708 \cdot 10^2$
		$2.268 \cdot 10^1$	$-1.171 \cdot 10^3$	$2.012 \cdot 10^3$	$-1.221 \cdot 10^3$	$3.046 \cdot 10^2$	$-2.719 \cdot 10^1$	
	l_1	$-1.924 \cdot 10^{-1}$	$3.314 \cdot 10^{-1}$	$1.150 \cdot 10^0$	$-1.268 \cdot 10^{-2}$	$2.415 \cdot 10^{-3}$	$1.019 \cdot 10^{-1}$	$2.509 \cdot 10^{-1}$
		$-6.764 \cdot 10^{-1}$	$2.555 \cdot 10^{-1}$	$-2.229 \cdot 10^{-2}$	$2.286 \cdot 10^0$	$-5.106 \cdot 10^0$	$3.601 \cdot 10^0$	$-9.345 \cdot 10^{-1}$
		$4.309 \cdot 10^{-2}$	$-2.110 \cdot 10^0$	$3.649 \cdot 10^0$	$-1.905 \cdot 10^0$	$1.673 \cdot 10^{-1}$	$6.775 \cdot 10^{-2}$	
l_2	$3.287 \cdot 10^0$	$-2.094 \cdot 10^0$	$2.744 \cdot 10^0$	$-3.170 \cdot 10^{-1}$	$3.042 \cdot 10^{-2}$	$-3.616 \cdot 10^1$	$4.933 \cdot 10^1$	
	$-2.830 \cdot 10^1$	$6.830 \cdot 10^0$	$-5.846 \cdot 10^{-1}$	$1.079 \cdot 10^2$	$-1.647 \cdot 10^2$	$9.355 \cdot 10^1$	$-2.163 \cdot 10^1$	
	$1.675 \cdot 10^0$	$-9.901 \cdot 10^1$	$1.533 \cdot 10^2$	$-8.417 \cdot 10^1$	$1.795 \cdot 10^1$	$-1.182 \cdot 10^0$		

TABLE IX. Fit coefficients of the function $h(\text{Pe}, \Phi_0)$ used to fit the variables of the Fourier coefficients $a_{3,2}^{1,1}$ and $a_{3,3}^{1,1}$ of the function g_{approx} .

56, 4213 (1972).

- [81] L. F. Rull, Phase diagram of a liquid crystal model: A computer simulation study, *Physica A: Statistical Mechanics and its Applications* **220**, 113 (1995).
- [82] R. Berardi, C. Fava, and C. Zannoni, A Gay-Berne potential for dissimilar biaxial particles, *Chemical Physics*

Letters **297**, 8 (1998).

- [83] X. Zheng and P. Palffy-Muhoray, Distance of closest approach of two arbitrary hard ellipses in two dimensions, *Physical Review E* **75**, 061709 (2007).

	$u_{-2,0}$ $u_{-1,3}$ $u_{1,2}$	$u_{-2,1}$ $u_{0,0}$ $u_{1,3}$	$u_{-2,2}$ $u_{0,1}$ $u_{2,0}$	$u_{-2,3}$ $u_{0,2}$ $u_{2,1}$	$u_{-1,0}$ $u_{0,3}$ $u_{2,2}$	$u_{-1,1}$ $u_{1,0}$ $u_{2,3}$	$u_{-1,2}$ $u_{1,1}$		
$a_{1,1}^{2,2}$	α	$1.160 \cdot 10^2$	$-1.714 \cdot 10^2$	$8.920 \cdot 10^1$	$-2.299 \cdot 10^1$	$2.207 \cdot 10^0$	$-4.472 \cdot 10^3$	$7.477 \cdot 10^3$	
		$-4.332 \cdot 10^3$	$1.026 \cdot 10^3$	$-8.389 \cdot 10^1$	$2.331 \cdot 10^4$	$-3.945 \cdot 10^4$	$2.313 \cdot 10^4$	$-5.492 \cdot 10^3$	
		$4.334 \cdot 10^2$	$-2.741 \cdot 10^4$	$4.525 \cdot 10^4$	$-2.534 \cdot 10^4$	$5.462 \cdot 10^3$	$-3.350 \cdot 10^2$		
	μ	$-1.537 \cdot 10^0$	$4.803 \cdot 10^{-1}$	$2.396 \cdot 10^0$	$-5.445 \cdot 10^{-1}$	$4.566 \cdot 10^{-2}$	$6.793 \cdot 10^1$	$-1.032 \cdot 10^2$	
		$5.229 \cdot 10^1$	$-1.089 \cdot 10^1$	$8.576 \cdot 10^{-1}$	$-4.279 \cdot 10^2$	$7.080 \cdot 10^2$	$-4.062 \cdot 10^2$	$9.678 \cdot 10^1$	
		$-8.141 \cdot 10^0$	$5.465 \cdot 10^2$	$-8.944 \cdot 10^2$	$4.990 \cdot 10^2$	$-1.101 \cdot 10^2$	$7.486 \cdot 10^0$		
	ς	$9.018 \cdot 10^0$	$-1.508 \cdot 10^1$	$8.872 \cdot 10^0$	$-2.010 \cdot 10^0$	$1.526 \cdot 10^{-1}$	$-9.176 \cdot 10^1$	$1.521 \cdot 10^2$	
		$-8.697 \cdot 10^1$	$2.004 \cdot 10^1$	$-1.527 \cdot 10^0$	$2.502 \cdot 10^2$	$-4.028 \cdot 10^2$	$2.199 \cdot 10^2$	$-4.665 \cdot 10^1$	
		$3.044 \cdot 10^0$	$-2.049 \cdot 10^2$	$3.185 \cdot 10^2$	$-1.639 \cdot 10^2$	$3.116 \cdot 10^1$	$-1.611 \cdot 10^0$		
	λ	$2.222 \cdot 10^1$	$-7.377 \cdot 10^1$	$7.020 \cdot 10^1$	$-1.879 \cdot 10^1$	$1.489 \cdot 10^0$	$3.147 \cdot 10^0$	$1.875 \cdot 10^2$	
		$-2.405 \cdot 10^2$	$7.099 \cdot 10^1$	$-4.903 \cdot 10^0$	$-1.000 \cdot 10^3$	$1.397 \cdot 10^3$	$-6.613 \cdot 10^2$	$1.823 \cdot 10^2$	
		$-2.339 \cdot 10^1$	$1.670 \cdot 10^3$	$-2.617 \cdot 10^3$	$1.434 \cdot 10^3$	$-3.548 \cdot 10^2$	$3.001 \cdot 10^1$		
	l_1	$2.640 \cdot 10^1$	$-3.808 \cdot 10^1$	$1.321 \cdot 10^1$	$-1.567 \cdot 10^0$	$-2.439 \cdot 10^{-1}$	$-2.574 \cdot 10^2$	$3.587 \cdot 10^2$	
		$-1.445 \cdot 10^2$	$6.743 \cdot 10^0$	$3.850 \cdot 10^0$	$6.212 \cdot 10^2$	$-7.429 \cdot 10^2$	$1.559 \cdot 10^2$	$8.084 \cdot 10^1$	
		$-2.482 \cdot 10^1$	$-2.171 \cdot 10^2$	$-6.785 \cdot 10^1$	$4.507 \cdot 10^2$	$-2.794 \cdot 10^2$	$4.884 \cdot 10^1$		
	l_2	$-4.641 \cdot 10^1$	$6.846 \cdot 10^1$	$-2.784 \cdot 10^1$	$3.294 \cdot 10^0$	$3.671 \cdot 10^{-1}$	$5.251 \cdot 10^2$	$-7.732 \cdot 10^2$	
		$3.526 \cdot 10^2$	$-4.097 \cdot 10^1$	$-3.657 \cdot 10^0$	$-1.481 \cdot 10^3$	$2.047 \cdot 10^3$	$-7.817 \cdot 10^2$	$7.315 \cdot 10^0$	
		$2.763 \cdot 10^1$	$9.647 \cdot 10^2$	$-9.916 \cdot 10^2$	$-2.481 \cdot 10^1$	$2.622 \cdot 10^2$	$-6.085 \cdot 10^1$		
	$a_{1,2}^{2,2}$	α	$2.924 \cdot 10^2$	$-5.108 \cdot 10^2$	$3.130 \cdot 10^2$	$-8.061 \cdot 10^1$	$7.192 \cdot 10^0$	$-4.821 \cdot 10^3$	$8.426 \cdot 10^3$
			$-5.155 \cdot 10^3$	$1.298 \cdot 10^3$	$-1.128 \cdot 10^2$	$1.897 \cdot 10^4$	$-3.272 \cdot 10^4$	$1.964 \cdot 10^4$	$-4.789 \cdot 10^3$
			$3.876 \cdot 10^2$	$-2.020 \cdot 10^4$	$3.400 \cdot 10^4$	$-1.959 \cdot 10^4$	$4.435 \cdot 10^3$	$-3.046 \cdot 10^2$	
μ		$-1.771 \cdot 10^{-1}$	$1.301 \cdot 10^{-1}$	$1.357 \cdot 10^0$	$-1.792 \cdot 10^{-1}$	$1.818 \cdot 10^{-2}$	$-1.425 \cdot 10^1$	$2.301 \cdot 10^1$	
		$-1.364 \cdot 10^1$	$3.345 \cdot 10^0$	$-2.921 \cdot 10^{-1}$	$5.713 \cdot 10^1$	$-9.034 \cdot 10^1$	$5.057 \cdot 10^1$	$-1.159 \cdot 10^1$	
		$9.718 \cdot 10^{-1}$	$-5.730 \cdot 10^1$	$8.963 \cdot 10^1$	$-4.929 \cdot 10^1$	$1.126 \cdot 10^1$	$-1.037 \cdot 10^0$		
ς		$-9.287 \cdot 10^{-1}$	$1.531 \cdot 10^0$	$-6.651 \cdot 10^{-1}$	$1.605 \cdot 10^{-1}$	$-1.378 \cdot 10^{-2}$	$1.299 \cdot 10^1$	$-2.207 \cdot 10^1$	
		$1.288 \cdot 10^1$	$-3.040 \cdot 10^0$	$2.421 \cdot 10^{-1}$	$-5.015 \cdot 10^1$	$8.376 \cdot 10^1$	$-4.760 \cdot 10^1$	$1.069 \cdot 10^1$	
		$-7.411 \cdot 10^{-1}$	$5.053 \cdot 10^1$	$-8.068 \cdot 10^1$	$4.233 \cdot 10^1$	$-7.990 \cdot 10^0$	$2.946 \cdot 10^{-1}$		
λ		$3.338 \cdot 10^{-2}$	$-5.412 \cdot 10^0$	$1.640 \cdot 10^1$	$-5.375 \cdot 10^0$	$5.855 \cdot 10^{-1}$	$-3.366 \cdot 10^2$	$6.070 \cdot 10^2$	
		$-4.108 \cdot 10^2$	$1.110 \cdot 10^2$	$-1.035 \cdot 10^1$	$1.534 \cdot 10^3$	$-2.673 \cdot 10^3$	$1.682 \cdot 10^3$	$-4.278 \cdot 10^2$	
		$3.844 \cdot 10^1$	$-1.853 \cdot 10^3$	$3.210 \cdot 10^3$	$-1.979 \cdot 10^3$	$5.012 \cdot 10^2$	$-4.678 \cdot 10^1$		
l_1		$-2.406 \cdot 10^1$	$4.059 \cdot 10^1$	$-2.663 \cdot 10^1$	$5.862 \cdot 10^0$	$-6.051 \cdot 10^{-1}$	$4.077 \cdot 10^2$	$-7.170 \cdot 10^2$	
		$4.445 \cdot 10^2$	$-1.186 \cdot 10^2$	$1.199 \cdot 10^1$	$-1.757 \cdot 10^3$	$3.119 \cdot 10^3$	$-1.965 \cdot 10^3$	$5.289 \cdot 10^2$	
		$-5.218 \cdot 10^1$	$2.153 \cdot 10^3$	$-3.828 \cdot 10^3$	$2.419 \cdot 10^3$	$-6.497 \cdot 10^2$	$6.310 \cdot 10^1$		
l_2		$3.468 \cdot 10^1$	$-5.881 \cdot 10^1$	$3.669 \cdot 10^1$	$-8.543 \cdot 10^0$	$9.004 \cdot 10^{-1}$	$-6.130 \cdot 10^2$	$1.082 \cdot 10^3$	
		$-6.732 \cdot 10^2$	$1.801 \cdot 10^2$	$-1.836 \cdot 10^1$	$2.678 \cdot 10^3$	$-4.767 \cdot 10^3$	$3.012 \cdot 10^3$	$-8.132 \cdot 10^2$	
		$8.080 \cdot 10^1$	$-3.301 \cdot 10^3$	$5.882 \cdot 10^3$	$-3.726 \cdot 10^3$	$1.003 \cdot 10^3$	$-9.798 \cdot 10^1$		

TABLE X. Fit coefficients of the function $h(\text{Pe}, \Phi_0)$ used to fit the variables of the Fourier coefficients $a_{1,1}^{2,2}$ and $a_{1,2}^{2,2}$ of the function g_{approx} .

	$u_{-2,0}$ $u_{-1,3}$ $u_{1,2}$	$u_{-2,1}$ $u_{0,0}$ $u_{1,3}$	$u_{-2,2}$ $u_{0,1}$ $u_{2,0}$	$u_{-2,3}$ $u_{0,2}$ $u_{2,1}$	$u_{-1,0}$ $u_{0,3}$ $u_{2,2}$	$u_{-1,1}$ $u_{1,0}$ $u_{2,3}$	$u_{-1,2}$ $u_{1,1}$		
$a_{1,3}^{2,2}$	α	$5.212 \cdot 10^2$	$-9.033 \cdot 10^2$	$5.639 \cdot 10^2$	$-1.535 \cdot 10^2$	$1.426 \cdot 10^1$	$-1.083 \cdot 10^4$	$1.867 \cdot 10^4$	
		$-1.130 \cdot 10^4$	$2.833 \cdot 10^3$	$-2.437 \cdot 10^2$	$3.994 \cdot 10^4$	$-6.754 \cdot 10^4$	$3.956 \cdot 10^4$	$-9.356 \cdot 10^3$	
		$7.237 \cdot 10^2$	$-3.783 \cdot 10^4$	$6.155 \cdot 10^4$	$-3.371 \cdot 10^4$	$6.990 \cdot 10^3$	$-3.897 \cdot 10^2$		
	μ	$-1.080 \cdot 10^1$	$1.508 \cdot 10^1$	$-5.515 \cdot 10^0$	$1.111 \cdot 10^0$	$-6.551 \cdot 10^{-2}$	$8.267 \cdot 10^1$	$-1.164 \cdot 10^2$	
		$5.225 \cdot 10^1$	$-8.708 \cdot 10^0$	$4.090 \cdot 10^{-1}$	$-1.383 \cdot 10^2$	$1.596 \cdot 10^2$	$-3.993 \cdot 10^1$	$-5.423 \cdot 10^0$	
		$1.839 \cdot 10^0$	$1.735 \cdot 10^1$	$4.834 \cdot 10^1$	$-8.701 \cdot 10^1$	$3.825 \cdot 10^1$	$-4.834 \cdot 10^0$		
	ς	$-3.506 \cdot 10^0$	$5.435 \cdot 10^0$	$-2.693 \cdot 10^0$	$5.960 \cdot 10^{-1}$	$-4.579 \cdot 10^{-2}$	$4.537 \cdot 10^1$	$-7.234 \cdot 10^1$	
		$3.929 \cdot 10^1$	$-8.514 \cdot 10^0$	$6.099 \cdot 10^{-1}$	$-1.265 \cdot 10^2$	$1.926 \cdot 10^2$	$-9.597 \cdot 10^1$	$1.728 \cdot 10^1$	
		$-7.572 \cdot 10^{-1}$	$8.548 \cdot 10^1$	$-1.128 \cdot 10^2$	$3.958 \cdot 10^1$	$-1.435 \cdot 10^{-1}$	$-1.107 \cdot 10^0$		
	λ	$-2.317 \cdot 10^2$	$4.269 \cdot 10^2$	$-1.535 \cdot 10^2$	$1.859 \cdot 10^1$	$-4.416 \cdot 10^{-1}$	$-3.712 \cdot 10^2$	$3.798 \cdot 10^2$	
		$-6.158 \cdot 10^2$	$2.316 \cdot 10^2$	$-2.417 \cdot 10^1$	$4.517 \cdot 10^3$	$-7.137 \cdot 10^3$	$4.796 \cdot 10^3$	$-1.270 \cdot 10^3$	
		$1.101 \cdot 10^2$	$-5.448 \cdot 10^3$	$8.704 \cdot 10^3$	$-5.238 \cdot 10^3$	$1.230 \cdot 10^3$	$-9.100 \cdot 10^1$		
	l_1	$2.562 \cdot 10^0$	$-5.279 \cdot 10^0$	$5.126 \cdot 10^0$	$-1.252 \cdot 10^0$	$1.528 \cdot 10^{-1}$	$-2.034 \cdot 10^1$	$4.008 \cdot 10^1$	
		$-2.890 \cdot 10^1$	$9.069 \cdot 10^0$	$-1.080 \cdot 10^0$	$8.125 \cdot 10^1$	$-1.570 \cdot 10^2$	$1.106 \cdot 10^2$	$-3.400 \cdot 10^1$	
		$3.886 \cdot 10^0$	$-7.999 \cdot 10^1$	$1.498 \cdot 10^2$	$-1.015 \cdot 10^2$	$2.953 \cdot 10^1$	$-3.112 \cdot 10^0$		
	l_2	$-2.399 \cdot 10^0$	$4.389 \cdot 10^0$	$-9.411 \cdot 10^{-1}$	$4.111 \cdot 10^{-1}$	$-8.907 \cdot 10^{-3}$	$-3.861 \cdot 10^1$	$7.346 \cdot 10^1$	
		$-5.171 \cdot 10^1$	$1.620 \cdot 10^1$	$-1.811 \cdot 10^0$	$1.626 \cdot 10^2$	$-3.006 \cdot 10^2$	$2.002 \cdot 10^2$	$-5.750 \cdot 10^1$	
		$5.829 \cdot 10^0$	$-2.028 \cdot 10^2$	$3.785 \cdot 10^2$	$-2.562 \cdot 10^2$	$7.515 \cdot 10^1$	$-8.103 \cdot 10^0$		
	$a_{2,1}^{2,2}$	α	$1.022 \cdot 10^1$	$-7.775 \cdot 10^0$	$-3.443 \cdot 10^0$	$4.010 \cdot 10^0$	$-4.868 \cdot 10^{-1}$	$1.963 \cdot 10^2$	$-4.210 \cdot 10^2$
			$3.077 \cdot 10^2$	$-9.182 \cdot 10^1$	$9.159 \cdot 10^0$	$-1.215 \cdot 10^3$	$2.308 \cdot 10^3$	$-1.530 \cdot 10^3$	$4.177 \cdot 10^2$
			$-3.896 \cdot 10^1$	$1.538 \cdot 10^3$	$-2.785 \cdot 10^3$	$1.754 \cdot 10^3$	$-4.480 \cdot 10^2$	$3.810 \cdot 10^1$	
μ		$-1.074 \cdot 10^{-1}$	$1.991 \cdot 10^0$	$-6.196 \cdot 10^{-1}$	$5.463 \cdot 10^{-1}$	$-6.083 \cdot 10^{-2}$	$4.029 \cdot 10^1$	$-7.197 \cdot 10^1$	
		$4.454 \cdot 10^1$	$-1.151 \cdot 10^1$	$1.075 \cdot 10^0$	$-1.502 \cdot 10^2$	$2.511 \cdot 10^2$	$-1.482 \cdot 10^2$	$3.640 \cdot 10^1$	
		$-3.172 \cdot 10^0$	$1.617 \cdot 10^2$	$-2.731 \cdot 10^2$	$1.654 \cdot 10^2$	$-4.280 \cdot 10^1$	$4.216 \cdot 10^0$		
ς		$-1.140 \cdot 10^0$	$2.406 \cdot 10^0$	$-1.530 \cdot 10^0$	$4.751 \cdot 10^{-1}$	$-4.781 \cdot 10^{-2}$	$1.847 \cdot 10^1$	$-3.852 \cdot 10^1$	
		$2.667 \cdot 10^1$	$-7.482 \cdot 10^0$	$7.337 \cdot 10^{-1}$	$-9.404 \cdot 10^1$	$1.797 \cdot 10^2$	$-1.171 \cdot 10^2$	$3.108 \cdot 10^1$	
		$-2.825 \cdot 10^0$	$1.174 \cdot 10^2$	$-2.130 \cdot 10^2$	$1.326 \cdot 10^2$	$-3.348 \cdot 10^1$	$2.871 \cdot 10^0$		
λ		$5.378 \cdot 10^1$	$-6.892 \cdot 10^1$	$3.079 \cdot 10^1$	$-3.234 \cdot 10^0$	$-1.109 \cdot 10^{-1}$	$-1.154 \cdot 10^2$	$8.951 \cdot 10^1$	
		$-3.896 \cdot 10^0$	$-1.481 \cdot 10^1$	$5.905 \cdot 10^0$	$8.721 \cdot 10^2$	$-1.278 \cdot 10^3$	$5.346 \cdot 10^2$	$1.681 \cdot 10^1$	
		$-4.301 \cdot 10^1$	$2.502 \cdot 10^3$	$-6.391 \cdot 10^3$	$6.130 \cdot 10^3$	$-2.619 \cdot 10^3$	$4.362 \cdot 10^2$		
l_1		$6.359 \cdot 10^{-1}$	$-7.471 \cdot 10^{-1}$	$1.554 \cdot 10^0$	$-2.732 \cdot 10^{-2}$	$-3.765 \cdot 10^{-3}$	$-1.787 \cdot 10^1$	$1.616 \cdot 10^1$	
		$-3.543 \cdot 10^0$	$-3.277 \cdot 10^{-1}$	$1.330 \cdot 10^{-1}$	$1.854 \cdot 10^1$	$8.966 \cdot 10^0$	$-2.464 \cdot 10^1$	$9.834 \cdot 10^0$	
		$-1.171 \cdot 10^0$	$1.733 \cdot 10^1$	$-5.862 \cdot 10^1$	$4.838 \cdot 10^1$	$-1.406 \cdot 10^1$	$1.345 \cdot 10^0$		

TABLE XI. Fit coefficients of the function $h(\text{Pe}, \Phi_0)$ used to fit the variables of the Fourier coefficients $a_{1,3}^{2,2}$ and $a_{2,1}^{2,2}$ of the function g_{approx} .

	$u_{-2,0}$ $u_{-1,3}$ $u_{1,2}$	$u_{-2,1}$ $u_{0,0}$ $u_{1,3}$	$u_{-2,2}$ $u_{0,1}$ $u_{2,0}$	$u_{-2,3}$ $u_{0,2}$ $u_{2,1}$	$u_{-1,0}$ $u_{0,3}$ $u_{2,2}$	$u_{-1,1}$ $u_{1,0}$ $u_{2,3}$	$u_{-1,2}$ $u_{1,1}$		
$a_{2,2}^{2,2}$	α	$1.187 \cdot 10^2$	$-2.271 \cdot 10^2$	$1.525 \cdot 10^2$	$-4.427 \cdot 10^1$	$4.172 \cdot 10^0$	$-2.440 \cdot 10^3$	$4.364 \cdot 10^3$	
		$-2.727 \cdot 10^3$	$6.935 \cdot 10^2$	$-6.024 \cdot 10^1$	$9.710 \cdot 10^3$	$-1.681 \cdot 10^4$	$1.007 \cdot 10^4$	$-2.406 \cdot 10^3$	
		$1.810 \cdot 10^2$	$-9.821 \cdot 10^3$	$1.624 \cdot 10^4$	$-9.041 \cdot 10^3$	$1.864 \cdot 10^3$	$-9.070 \cdot 10^1$		
	μ	$-2.205 \cdot 10^0$	$3.439 \cdot 10^0$	$-6.182 \cdot 10^{-1}$	$3.876 \cdot 10^{-1}$	$-3.567 \cdot 10^{-2}$	$2.937 \cdot 10^1$	$-4.887 \cdot 10^1$	
		$2.775 \cdot 10^1$	$-6.470 \cdot 10^0$	$5.212 \cdot 10^{-1}$	$-9.369 \cdot 10^1$	$1.511 \cdot 10^2$	$-8.151 \cdot 10^1$	$1.694 \cdot 10^1$	
		$-9.687 \cdot 10^{-1}$	$7.813 \cdot 10^1$	$-1.168 \cdot 10^2$	$5.445 \cdot 10^1$	$-7.595 \cdot 10^0$	$-1.765 \cdot 10^{-1}$		
	ς	$-1.164 \cdot 10^0$	$2.028 \cdot 10^0$	$-1.062 \cdot 10^0$	$3.017 \cdot 10^{-1}$	$-2.847 \cdot 10^{-2}$	$1.763 \cdot 10^1$	$-3.046 \cdot 10^1$	
		$1.842 \cdot 10^1$	$-4.611 \cdot 10^0$	$4.067 \cdot 10^{-1}$	$-6.337 \cdot 10^1$	$1.072 \cdot 10^2$	$-6.278 \cdot 10^1$	$1.491 \cdot 10^1$	
		$-1.156 \cdot 10^0$	$6.299 \cdot 10^1$	$-1.036 \cdot 10^2$	$5.799 \cdot 10^1$	$-1.267 \cdot 10^1$	$8.282 \cdot 10^{-1}$		
	λ	$-8.374 \cdot 10^1$	$1.160 \cdot 10^2$	$-4.334 \cdot 10^1$	$8.179 \cdot 10^0$	$-5.720 \cdot 10^{-1}$	$7.202 \cdot 10^2$	$-1.034 \cdot 10^3$	
		$4.713 \cdot 10^2$	$-8.933 \cdot 10^1$	$6.174 \cdot 10^0$	$-1.618 \cdot 10^3$	$2.199 \cdot 10^3$	$-9.128 \cdot 10^2$	$1.436 \cdot 10^2$	
		$-5.914 \cdot 10^0$	$1.025 \cdot 10^3$	$-1.250 \cdot 10^3$	$4.123 \cdot 10^2$	$-3.457 \cdot 10^1$	$-9.732 \cdot 10^{-1}$		
	l_1	$1.377 \cdot 10^{-1}$	$-2.289 \cdot 10^{-1}$	$1.851 \cdot 10^0$	$-1.933 \cdot 10^{-1}$	$2.091 \cdot 10^{-2}$	$-1.088 \cdot 10^1$	$1.907 \cdot 10^1$	
		$-1.309 \cdot 10^1$	$3.622 \cdot 10^0$	$-3.672 \cdot 10^{-1}$	$5.149 \cdot 10^1$	$-9.142 \cdot 10^1$	$5.941 \cdot 10^1$	$-1.623 \cdot 10^1$	
		$1.620 \cdot 10^0$	$-6.592 \cdot 10^1$	$1.177 \cdot 10^2$	$-7.620 \cdot 10^1$	$2.089 \cdot 10^1$	$-2.099 \cdot 10^0$		
	l_2	$4.534 \cdot 10^0$	$-1.026 \cdot 10^1$	$8.936 \cdot 10^0$	$-1.916 \cdot 10^0$	$1.938 \cdot 10^{-1}$	$-9.532 \cdot 10^1$	$1.842 \cdot 10^2$	
		$-1.190 \cdot 10^2$	$3.146 \cdot 10^1$	$-2.983 \cdot 10^0$	$4.046 \cdot 10^2$	$-7.392 \cdot 10^2$	$4.630 \cdot 10^2$	$-1.191 \cdot 10^2$	
		$1.055 \cdot 10^1$	$-4.567 \cdot 10^2$	$8.042 \cdot 10^2$	$-4.868 \cdot 10^2$	$1.190 \cdot 10^2$	$-9.547 \cdot 10^0$		
	$a_{2,3}^{2,2}$	α	$1.074 \cdot 10^2$	$-2.135 \cdot 10^2$	$1.610 \cdot 10^2$	$-5.058 \cdot 10^1$	$4.260 \cdot 10^0$	$-1.427 \cdot 10^3$	$2.364 \cdot 10^3$
			$-1.408 \cdot 10^3$	$3.445 \cdot 10^2$	$-2.647 \cdot 10^1$	$6.291 \cdot 10^3$	$-1.021 \cdot 10^4$	$5.943 \cdot 10^3$	$-1.439 \cdot 10^3$
			$1.148 \cdot 10^2$	$-5.055 \cdot 10^3$	$7.397 \cdot 10^3$	$-3.556 \cdot 10^3$	$5.373 \cdot 10^2$	$1.326 \cdot 10^1$	
μ		$-3.181 \cdot 10^0$	$4.391 \cdot 10^0$	$-8.666 \cdot 10^{-1}$	$4.386 \cdot 10^{-1}$	$-3.813 \cdot 10^{-2}$	$2.843 \cdot 10^1$	$-3.838 \cdot 10^1$	
		$1.955 \cdot 10^1$	$-4.615 \cdot 10^0$	$4.264 \cdot 10^{-1}$	$-7.746 \cdot 10^1$	$1.189 \cdot 10^2$	$-7.251 \cdot 10^1$	$2.033 \cdot 10^1$	
		$-2.198 \cdot 10^0$	$1.759 \cdot 10^2$	$-2.900 \cdot 10^2$	$1.812 \cdot 10^2$	$-5.018 \cdot 10^1$	$5.118 \cdot 10^0$		
ς		$-2.392 \cdot 10^0$	$3.420 \cdot 10^0$	$-1.544 \cdot 10^0$	$3.520 \cdot 10^{-1}$	$-2.739 \cdot 10^{-2}$	$3.251 \cdot 10^1$	$-4.418 \cdot 10^1$	
		$2.153 \cdot 10^1$	$-4.495 \cdot 10^0$	$3.418 \cdot 10^{-1}$	$-1.253 \cdot 10^2$	$1.680 \cdot 10^2$	$-8.150 \cdot 10^1$	$1.698 \cdot 10^1$	
		$-1.300 \cdot 10^0$	$1.368 \cdot 10^2$	$-1.803 \cdot 10^2$	$8.575 \cdot 10^1$	$-1.746 \cdot 10^1$	$1.298 \cdot 10^0$		
l_1		$1.364 \cdot 10^{-1}$	$1.935 \cdot 10^0$	$-8.913 \cdot 10^{-1}$	$6.423 \cdot 10^{-1}$	$-6.122 \cdot 10^{-2}$	$1.009 \cdot 10^2$	$-1.564 \cdot 10^2$	
		$8.288 \cdot 10^1$	$-1.786 \cdot 10^1$	$1.303 \cdot 10^0$	$-2.469 \cdot 10^2$	$3.409 \cdot 10^2$	$-1.512 \cdot 10^2$	$2.381 \cdot 10^1$	
		$-8.412 \cdot 10^{-1}$	$1.657 \cdot 10^2$	$-2.036 \cdot 10^2$	$7.120 \cdot 10^1$	$-5.406 \cdot 10^0$	$-4.413 \cdot 10^{-1}$		
l_2		$-1.205 \cdot 10^1$	$1.563 \cdot 10^1$	$-5.824 \cdot 10^0$	$1.354 \cdot 10^0$	$-9.202 \cdot 10^{-2}$	$1.044 \cdot 10^2$	$-1.239 \cdot 10^2$	
		$5.024 \cdot 10^1$	$-8.027 \cdot 10^0$	$4.392 \cdot 10^{-1}$	$-3.705 \cdot 10^1$	$-4.155 \cdot 10^1$	$6.987 \cdot 10^1$	$-2.515 \cdot 10^1$	
		$2.376 \cdot 10^0$	$-8.591 \cdot 10^0$	$4.524 \cdot 10^1$	$-2.277 \cdot 10^1$	$-2.953 \cdot 10^0$	$2.219 \cdot 10^0$		

TABLE XII. Fit coefficients of the function $h(\text{Pe}, \Phi_0)$ used to fit the variables of the Fourier coefficients $a_{2,2}^{2,2}$ and $a_{2,3}^{2,2}$ of the function g_{approx} .

	$u_{-2,0}$ $u_{-1,3}$ $u_{1,2}$	$u_{-2,1}$ $u_{0,0}$ $u_{1,3}$	$u_{-2,2}$ $u_{0,1}$ $u_{2,0}$	$u_{-2,3}$ $u_{0,2}$ $u_{2,1}$	$u_{-1,0}$ $u_{0,3}$ $u_{2,2}$	$u_{-1,1}$ $u_{1,0}$ $u_{2,3}$	$u_{-1,2}$ $u_{1,1}$	
$a_{3,1}^{2,2}$	α	$1.253 \cdot 10^1$	$-2.241 \cdot 10^1$	$1.460 \cdot 10^1$	$-4.556 \cdot 10^0$	$3.797 \cdot 10^{-1}$	$-1.763 \cdot 10^2$	$3.230 \cdot 10^2$
		$-2.121 \cdot 10^2$	$5.867 \cdot 10^1$	$-5.593 \cdot 10^0$	$7.484 \cdot 10^2$	$-1.368 \cdot 10^3$	$8.921 \cdot 10^2$	$-2.444 \cdot 10^2$
		$2.358 \cdot 10^1$	$-9.270 \cdot 10^2$	$1.681 \cdot 10^3$	$-1.084 \cdot 10^3$	$2.921 \cdot 10^2$	$-2.751 \cdot 10^1$	
	μ	$3.116 \cdot 10^0$	$-5.958 \cdot 10^0$	$5.363 \cdot 10^0$	$-1.097 \cdot 10^0$	$9.662 \cdot 10^{-2}$	$-5.617 \cdot 10^1$	$9.857 \cdot 10^1$
		$-6.089 \cdot 10^1$	$1.543 \cdot 10^1$	$-1.362 \cdot 10^0$	$2.246 \cdot 10^2$	$-3.879 \cdot 10^2$	$2.351 \cdot 10^2$	$-5.861 \cdot 10^1$
		$4.984 \cdot 10^0$	$-2.502 \cdot 10^2$	$4.263 \cdot 10^2$	$-2.536 \cdot 10^2$	$6.126 \cdot 10^1$	$-4.961 \cdot 10^0$	
	ς	$1.973 \cdot 10^0$	$-3.483 \cdot 10^0$	$2.308 \cdot 10^0$	$-5.100 \cdot 10^{-1}$	$4.358 \cdot 10^{-2}$	$-2.349 \cdot 10^1$	$4.140 \cdot 10^1$
		$-2.556 \cdot 10^1$	$6.552 \cdot 10^0$	$-5.901 \cdot 10^{-1}$	$9.411 \cdot 10^1$	$-1.653 \cdot 10^2$	$1.016 \cdot 10^2$	$-2.575 \cdot 10^1$
		$2.253 \cdot 10^0$	$-1.092 \cdot 10^2$	$1.901 \cdot 10^2$	$-1.153 \cdot 10^2$	$2.867 \cdot 10^1$	$-2.442 \cdot 10^0$	
	l_1	$2.321 \cdot 10^0$	$-4.337 \cdot 10^0$	$4.297 \cdot 10^0$	$-8.316 \cdot 10^{-1}$	$7.375 \cdot 10^{-2}$	$-4.384 \cdot 10^1$	$7.713 \cdot 10^1$
		$-4.794 \cdot 10^1$	$1.208 \cdot 10^1$	$-1.065 \cdot 10^0$	$1.770 \cdot 10^2$	$-3.055 \cdot 10^2$	$1.849 \cdot 10^2$	$-4.589 \cdot 10^1$
		$3.892 \cdot 10^0$	$-1.970 \cdot 10^2$	$3.346 \cdot 10^2$	$-1.982 \cdot 10^2$	$4.756 \cdot 10^1$	$-3.802 \cdot 10^0$	
$a_{3,2}^{2,2}$	α	$-1.567 \cdot 10^1$	$5.227 \cdot 10^1$	$-5.663 \cdot 10^1$	$2.489 \cdot 10^1$	$-2.510 \cdot 10^0$	$1.821 \cdot 10^3$	$-3.318 \cdot 10^3$
		$2.145 \cdot 10^3$	$-5.752 \cdot 10^2$	$5.309 \cdot 10^1$	$-8.165 \cdot 10^3$	$1.454 \cdot 10^4$	$-9.155 \cdot 10^3$	$2.396 \cdot 10^3$
		$-2.182 \cdot 10^2$	$9.561 \cdot 10^3$	$-1.674 \cdot 10^4$	$1.028 \cdot 10^4$	$-2.584 \cdot 10^3$	$2.170 \cdot 10^2$	
	μ	$-7.079 \cdot 10^{-2}$	$-4.118 \cdot 10^{-1}$	$1.701 \cdot 10^0$	$-2.283 \cdot 10^{-1}$	$1.913 \cdot 10^{-2}$	$9.688 \cdot 10^{-1}$	$1.943 \cdot 10^0$
		$-3.271 \cdot 10^0$	$1.283 \cdot 10^0$	$-1.376 \cdot 10^{-1}$	$2.417 \cdot 10^1$	$-5.352 \cdot 10^1$	$3.858 \cdot 10^1$	$-1.065 \cdot 10^1$
		$8.843 \cdot 10^{-1}$	$-2.624 \cdot 10^1$	$4.915 \cdot 10^1$	$-2.742 \cdot 10^1$	$4.462 \cdot 10^0$	$8.313 \cdot 10^{-2}$	
	ς	$-6.017 \cdot 10^{-1}$	$1.010 \cdot 10^0$	$-4.435 \cdot 10^{-1}$	$1.340 \cdot 10^{-1}$	$-1.376 \cdot 10^{-2}$	$1.482 \cdot 10^1$	$-2.509 \cdot 10^1$
		$1.487 \cdot 10^1$	$-3.605 \cdot 10^0$	$3.048 \cdot 10^{-1}$	$-5.312 \cdot 10^1$	$8.850 \cdot 10^1$	$-5.110 \cdot 10^1$	$1.207 \cdot 10^1$
		$-9.858 \cdot 10^{-1}$	$6.080 \cdot 10^1$	$-1.028 \cdot 10^2$	$6.088 \cdot 10^1$	$-1.499 \cdot 10^1$	$1.301 \cdot 10^0$	
	λ	$4.981 \cdot 10^1$	$-9.522 \cdot 10^1$	$6.709 \cdot 10^1$	$-1.494 \cdot 10^1$	$1.206 \cdot 10^0$	$-3.968 \cdot 10^2$	$8.109 \cdot 10^2$
		$-5.301 \cdot 10^2$	$1.433 \cdot 10^2$	$-1.312 \cdot 10^1$	$3.181 \cdot 10^3$	$-6.036 \cdot 10^3$	$3.793 \cdot 10^3$	$-9.548 \cdot 10^2$
		$7.910 \cdot 10^1$	$-4.791 \cdot 10^3$	$8.606 \cdot 10^3$	$-4.905 \cdot 10^3$	$1.060 \cdot 10^3$	$-6.700 \cdot 10^1$	
	l_1	$1.327 \cdot 10^0$	$-2.641 \cdot 10^0$	$2.662 \cdot 10^0$	$-3.667 \cdot 10^{-1}$	$2.837 \cdot 10^{-2}$	$-1.514 \cdot 10^1$	$2.598 \cdot 10^1$
		$-1.533 \cdot 10^1$	$3.668 \cdot 10^0$	$-3.065 \cdot 10^{-1}$	$5.540 \cdot 10^1$	$-9.387 \cdot 10^1$	$5.535 \cdot 10^1$	$-1.328 \cdot 10^1$
		$1.066 \cdot 10^0$	$-5.728 \cdot 10^1$	$9.516 \cdot 10^1$	$-5.444 \cdot 10^1$	$1.232 \cdot 10^1$	$-8.887 \cdot 10^{-1}$	
	l_2	$-2.100 \cdot 10^0$	$3.647 \cdot 10^0$	$-7.773 \cdot 10^{-1}$	$4.886 \cdot 10^{-1}$	$-3.254 \cdot 10^{-2}$	$1.801 \cdot 10^0$	$-2.702 \cdot 10^0$
		$9.164 \cdot 10^{-1}$	$-7.536 \cdot 10^{-2}$	$-8.563 \cdot 10^{-3}$	$2.497 \cdot 10^1$	$-4.453 \cdot 10^1$	$2.836 \cdot 10^1$	$-7.332 \cdot 10^0$
		$6.070 \cdot 10^{-1}$	$-2.603 \cdot 10^1$	$3.820 \cdot 10^1$	$-1.646 \cdot 10^1$	$8.255 \cdot 10^{-1}$	$5.431 \cdot 10^{-1}$	

TABLE XIII. Fit coefficients of the function $h(\text{Pe}, \Phi_0)$ used to fit the variables of the Fourier coefficients $a_{3,1}^{2,2}$ and $a_{3,2}^{2,2}$ of the function g_{approx} .

		$u_{-2,0}$ $u_{-1,3}$ $u_{1,2}$	$u_{-2,1}$ $u_{0,0}$ $u_{1,3}$	$u_{-2,2}$ $u_{0,1}$ $u_{2,0}$	$u_{-2,3}$ $u_{0,2}$ $u_{2,1}$	$u_{-1,0}$ $u_{0,3}$ $u_{2,2}$	$u_{-1,1}$ $u_{1,0}$ $u_{2,3}$	$u_{-1,2}$ $u_{1,1}$
$a_{3,3}^{2,2}$	α	$-1.620 \cdot 10^2$	$3.010 \cdot 10^2$	$-2.002 \cdot 10^2$	$5.544 \cdot 10^1$	$-4.809 \cdot 10^0$	$2.596 \cdot 10^3$	$-4.653 \cdot 10^3$
		$2.959 \cdot 10^3$	$-7.854 \cdot 10^2$	$7.223 \cdot 10^1$	$-1.060 \cdot 10^4$	$1.879 \cdot 10^4$	$-1.176 \cdot 10^4$	$3.055 \cdot 10^3$
		$-2.726 \cdot 10^2$	$1.202 \cdot 10^4$	$-2.099 \cdot 10^4$	$1.286 \cdot 10^4$	$-3.224 \cdot 10^3$	$2.712 \cdot 10^2$	
	μ	$-1.517 \cdot 10^0$	$1.745 \cdot 10^0$	$5.371 \cdot 10^{-1}$	$3.389 \cdot 10^{-3}$	$3.217 \cdot 10^{-3}$	$6.091 \cdot 10^{-1}$	$3.130 \cdot 10^0$
		$-4.264 \cdot 10^0$	$1.298 \cdot 10^0$	$-1.181 \cdot 10^{-1}$	$1.651 \cdot 10^1$	$-3.395 \cdot 10^1$	$2.224 \cdot 10^1$	$-5.489 \cdot 10^0$
		$4.296 \cdot 10^{-1}$	$-1.928 \cdot 10^1$	$3.339 \cdot 10^1$	$-1.840 \cdot 10^1$	$3.659 \cdot 10^0$	$-1.668 \cdot 10^{-1}$	
	ς	$-2.081 \cdot 10^0$	$3.190 \cdot 10^0$	$-1.491 \cdot 10^0$	$3.283 \cdot 10^{-1}$	$-2.593 \cdot 10^{-2}$	$2.233 \cdot 10^1$	$-3.543 \cdot 10^1$
		$1.950 \cdot 10^1$	$-4.449 \cdot 10^0$	$3.497 \cdot 10^{-1}$	$-7.245 \cdot 10^1$	$1.152 \cdot 10^2$	$-6.293 \cdot 10^1$	$1.360 \cdot 10^1$
		$-9.471 \cdot 10^{-1}$	$6.798 \cdot 10^1$	$-1.055 \cdot 10^2$	$5.473 \cdot 10^1$	$-1.062 \cdot 10^1$	$5.963 \cdot 10^{-1}$	
	λ	$-3.603 \cdot 10^1$	$5.328 \cdot 10^1$	$-2.489 \cdot 10^1$	$6.364 \cdot 10^0$	$-4.972 \cdot 10^{-1}$	$3.886 \cdot 10^2$	$-6.220 \cdot 10^2$
		$3.443 \cdot 10^2$	$-7.918 \cdot 10^1$	$6.262 \cdot 10^0$	$-1.256 \cdot 10^3$	$2.019 \cdot 10^3$	$-1.113 \cdot 10^3$	$2.486 \cdot 10^2$
		$-1.794 \cdot 10^1$	$1.202 \cdot 10^3$	$-1.893 \cdot 10^3$	$1.006 \cdot 10^3$	$-2.067 \cdot 10^2$	$1.220 \cdot 10^1$	
	l_1	$1.708 \cdot 10^0$	$-2.795 \cdot 10^0$	$3.014 \cdot 10^0$	$-5.029 \cdot 10^{-1}$	$4.275 \cdot 10^{-2}$	$-3.172 \cdot 10^1$	$5.417 \cdot 10^1$
		$-3.217 \cdot 10^1$	$7.657 \cdot 10^0$	$-6.258 \cdot 10^{-1}$	$1.201 \cdot 10^2$	$-2.001 \cdot 10^2$	$1.136 \cdot 10^2$	$-2.591 \cdot 10^1$
		$1.944 \cdot 10^0$	$-1.178 \cdot 10^2$	$1.885 \cdot 10^2$	$-1.008 \cdot 10^2$	$2.068 \cdot 10^1$	$-1.217 \cdot 10^0$	
	l_2	$9.057 \cdot 10^0$	$-1.263 \cdot 10^1$	$8.982 \cdot 10^0$	$-1.765 \cdot 10^0$	$1.490 \cdot 10^{-1}$	$-1.251 \cdot 10^2$	$2.060 \cdot 10^2$
		$-1.182 \cdot 10^2$	$2.771 \cdot 10^1$	$-2.254 \cdot 10^0$	$4.253 \cdot 10^2$	$-7.021 \cdot 10^2$	$3.935 \cdot 10^2$	$-8.893 \cdot 10^1$
		$6.667 \cdot 10^0$	$-4.076 \cdot 10^2$	$6.539 \cdot 10^2$	$-3.501 \cdot 10^2$	$7.250 \cdot 10^1$	$-4.452 \cdot 10^0$	

TABLE XIV. Fit coefficients of the function $h(\text{Pe}, \Phi_0)$ used to fit the variables of the Fourier coefficient $a_{3,3}^{2,2}$ of the function g_{approx} .